STATISTICAL ANALYSIS OF ELLIPTICITY IN COSMIC MICROWAVE BACKGROUND ANISOTROPIES

by

EIRIK BERNTSEN

THESIS
for the degree of
MASTER OF SCIENCE

(Master i Teoretisk astrofysikk)

Faculty of Mathematics and Natural Sciences
University of Oslo

June 2009

Det matematisk- naturvitenskapelige fakultet
Universitetet i Oslo

Contents

Abstract

The ellipticity and obliquity of the spots in the WMAP 5 year Q, V, W and VW maps has been investigated and compared to simulated maps. No significant excess ellipticity has been found. The ellipticity is found to be around $\epsilon \approx 1.61$ for spots larger than 20 pixels and higher for smaller spots; an effect attributed to noise. This is in agreement with what is found on simulated maps. Obliquity for maps varies depending on what great circle is used as equator with mean of $\varepsilon = 57.2955^{\circ}$ when all possible such circles are considered. Obliquity result variation is higher as a function of what equator ring was is chosen for larger spots. This variation would seem to suggest a "preferred direction" on the CMB anisotropies, but detections of different "preferred directions" are made on simulated maps with almost as much significance. Also the results seem to be influenced by the mask and no certain detection of any preferred direction for the spots may be claimed from the obliquity data presented. The ellipticity data disagrees with earlier reports [1, 2, 3, 4] claiming significantly higher ellipticity in the WMAP data than can be found in simulated data. The results also disagree with findings that spots between 20 and 50 pixels show significantly higher ellipticity than spots of > 50 pixels. The obliquity result is consistent with what is reported by G.Gurzadyan et al [1, 2, 3, 4].

Acknowledgements

To write a thesis is not just science; nay 'tis to undertake a journey. One of adventure, wondrous segmentation faults, exciting new ways of cooking up bull to make it seem like one has had progress. One of marching into uncharted territories and one of consuming endless cups of coffee. Still; it would never have been possible had it not been for some people and abstract concepts. So; I would like to thank (in no particular order) Frode K. Hansen, my supervisor and the man behind it all — were it not for him, I would probably have written another thesis. Thanks for your friendly ways and for keeping up with my bull, even when I didn't. Kirsti Zeiner–Gundersen and Robert Berntsen, for keeping me fed and watered at the earliest part of my life, and for the invaluable contribution they gave in proof–reading language and offering helpful and encouraging comments. The Creator of the universe for giving me some background radiation to look at, the WMAP team for filming it, the HEALPix team for pixelating it and Einstein, Friedmann and others for explaining it. Lillian for being there and for teaching me how to work; and Anders, Anders, Mirza, Kristine, Henrik, Per, John et al. for making me forget. Lucy for granting me more time to work on the thesis, Skybertine, my imaginary girlfriend, for always being there for me, Nicolaas for his encouraging slaps in the face; Øystein and Kosovare for finding other and less painful forms of encouragement. Thank you to The White Stripes, migraine, 2001: A Space Odyssey, waterboarding and other forms of torture for existing—knowing that there are worse fates out there helps a lot. I also want to thank Knut, Arvid, Mateusz, Iselin, Stefano, Jan, Lillian (again) and Thomas for being my table tennis mates, as well as being my mates in general, Hanne–Torill, Lars, Tuva, Jostein, Maria, Silje, Kristin, Michael, Eivind, Håkon and Benedikte for just being my mates in general. Thanks also to Jostein and Per Harald answering my stupid questions.

Finally and above all; I would like to thank Spotfinder for finally and quite suddenly deciding to start working that afternoon, and sleep and my sanity for promising to once again take part in my life when this is all over.

I'm tired. And yes, I know, I forgot someone. So thanks to them as well.

Chapter 1

Introduction

The universe right after the Big Bang was an unimaginably hot place. Temperatures were much too high for anything except a quark–gluon plasma to exist. As time passed, the universe expanded and cooled; the quarks and gluons combined to form hadrons (protons and neutrons) and, later, when the universe was about 380000 years an event happened which cosmologists call recombination. What had up to then been a dense, hot plasma of free electrons and protons had cooled to about 3000K; cold enough for charged electrons and protons to combine to form neutral Hydrogen and Helium; the first atoms ever. As the newly formed atoms were electrically neutral, the intense electromagnetic radiation the plasma had previously scattered (effectively blocking it) could now move unhindered and the universe became transparent. This radiation is observable today and is called the *cosmic microwave background* (CMB). Even though the CMB had a temperature of about 3000K when released, the universe has expanded in size by more than 1100 times in all directions, and because of this, the photons are today observed as black body radiation with a temperature of 2.725K. By observing this radiation, it is possible to form an image of the very early universe and hence learn about its composition and the physics that governed it. Small density fluctuations in that hot primordial gas has created small differences in temperature with respect to direction; detected first by the COBE satellite [5] (Nobel prize 2006) and later in detail by both ground, balloon and satellite based experiments [6, 7, 8, 9]. From these observations several cosmological parameters have been estimated with great accuracy. These include the total energy density, the baryon density, the Hubble parameter and others. In particular the data from the BOOMERanG balloon experiment [7] showed for the first time to high significance that the universe seems to have a flat spacial geometry.

From measures of the CMB, a map of its temperature in different directions of the sky can be made. The middle temperature, or monopole, is 2.725K. If this is removed, what remains is a far weaker dipole signal — a

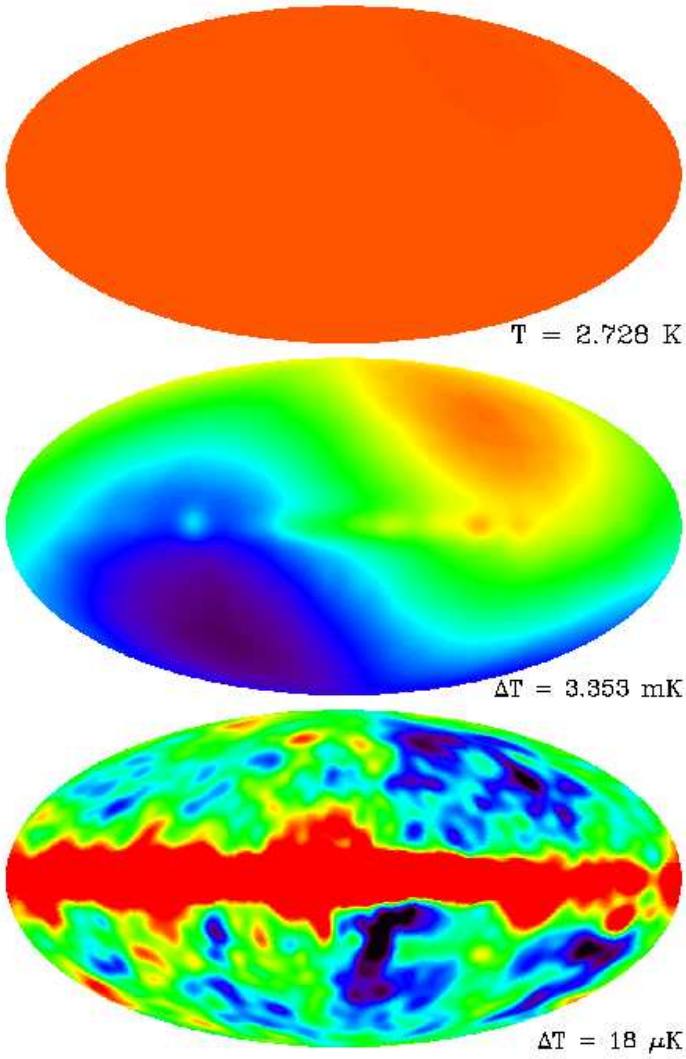

Figure 1.1: COBE DMR image showing the CMB monopole scaled linearly from 0–4K (top); the map, rescaled linearly, with the monopole removed (middle) and the map with both monopole and dipole removed (bottom) rescaled again to -100μK to $+100\mu$K. Notice how weak the dipole is when compared to the monopole (too weak to even notice) and how the CMB fluctuation are too weak to see compared even to the dipole. (from NASA/COBE team)

signature of the proper motion of the detector (and hence us) compared to the rest frame of the gas emitting the CMB. If this too is removed, what remains are small fluctuations of the order 10^{-5}K. These variations are an image of the density perturbations in the early universe. To extract information from this map of density perturbations, it is common to decompose it into spherical harmonics and calculate the angular power spectrum (see section 3.3) . The power spectrum shows the amplitude as a function of angular scale, and from this cosmological parameters may be extracted.

1.1 Thesis Description

The following is the thesis description as originally presented:

> It has been claimed that the CMB anisotropies (or "spots") have a higher elongation than expected in a flat universe. This was claimed first for the BOOMERanG data [1] and later for the WMAP first year data [2, 3]. Such an ellipticity is expected in hyperbolic universe models [3] and other speculative models. If the CMB ellipticity is indeed larger than expected, this could be important for understanding the universe and its shape and composition. All publications made claiming such an ellipticity come from the same author.
>
> The goal for this thesis is to provide an independent check of this reported ellipticity. The task is to write software to estimate the ellipticity of CMB maps and use the code to test the ellipticity of simulated maps based on an orthodox standard model universe. The code will then be used on real data from the WMAP satellite to check if results are consistent or not with the simulated maps. If the results found are in agreement with the above mentioned articles, the statistical significance of such a result will be carefully studied with respect to the WMAP instrumentation uncertainties. If detection is found to be significant, more accurate localization on the sphere will be attempted with wavelet analysis.

A "spot" was defined as described in [1]. This involves introducing a positive (negative) temperature threshold (also referred to as "cut" or "cutoff") for which all pixels with a higher (lower) value that are grouped together are considered to be a spot. A "grouping" in this respect means that it has an unbroken chain of neighbouring pixels connecting any two pixel in the spot. Two pixels are considered neighbours if they share an edge or a vertex. It was assumed, even if not stated, that the analysis would take spherical effects into account, and for that reason the following definition of ellipticity for a spot was adopted:

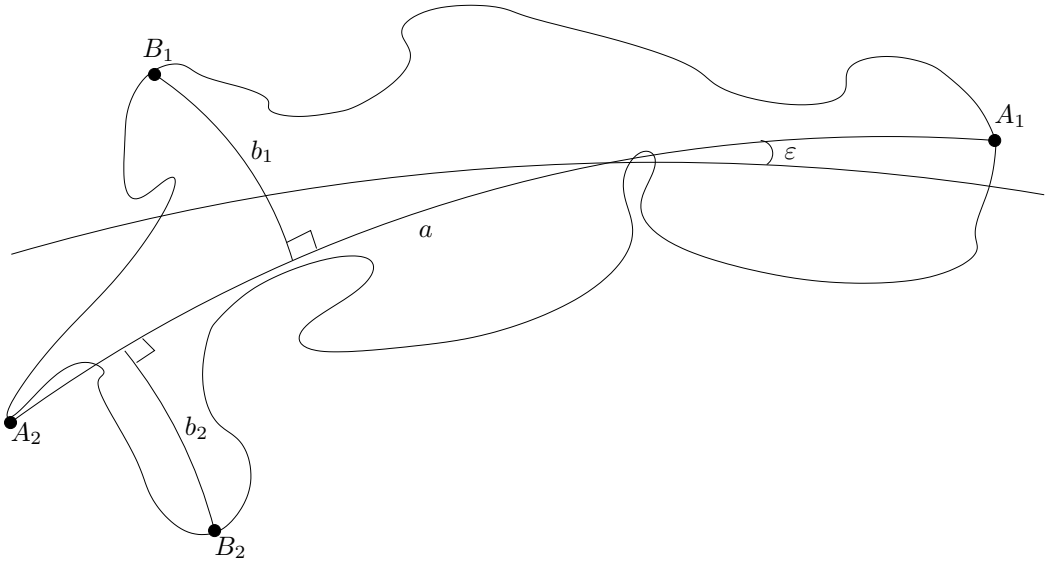

Figure 1.2: Example of a spot (presumably very large, or with high resolution). The major axis is formed between the two points furthest from each other, A_1 and A_2. The point B_1 is the furthest from the major axis on one side, the point B_2 has the greatest distance among points on the other side. The unconnected line crossing it represents the equator (so that this is an equatorial spot) and the obliquity ε is the smallest angle between the great circle traced by the major axis and the equator.

The major axis a was defined as the shortest distance (i.e. the great circle distance) connecting the center of the two pixels in the spot where that distance is the greatest. Two distances, b_1 and b_2 could then be defined with b_1 representing the distance to the pixel furthest away from any point on the major axis on one side and b_2 the distance to the pixel on the other side of the major axis with the greatest distance to it, as shown on figure 1.2. The minor axis is then

$$b \equiv \frac{b_1 + b_2}{2} \tag{1.1}$$

which leads to the ellipticity

$$\epsilon \equiv \frac{a}{b} \tag{1.2}$$

where a is the major axis and b is the minor axis. This gives a minimum possible ellipticity of 1 for a completely circular spot. The obliquity is defined as being the smallest angle between the great circle traced by the major axis and the equator as is also shown in figure 1.2.

As it turned out, there was no detection of excess ellipticity, and so the point of examining the distribution with wavelets was dropped. In stead,

we felt it prudent to extensively test the code to strengthen the case that there were indeed no ellipticity beyond what standard cosmological models would predict. Also, the search was widened to see if the obliquity measures could be used to determine if the spots have a preferred direction for their elongation.

Chapter 2

Theory

The theory will be divided roughly in two: the first part being the results traditionally derived analytically, the second concern results where the mathematics is so complex it is usually solved numerically. For that reason, the second part will be more descriptive than the first. Most of the theory here stems from books [10, 11, 12]. In all of this thesis, units will be used where $c = \hbar = 1$.

2.1 General Relativity and Cosmology

"There is nothing special about our location in the universe"

(from [11] p11). This is the cosmological principle, adopted by cosmologists for lack of any reason to think otherwise. The practical implication of this is that the universe is considered, in the standard model of cosmology as well as in this thesis, to be *homogenous* and *isotropic*. With this it is meant that; from any given point there are no direction in space that are preferred over another (isotropy) and that this is the case for any and all points in the universe (homogeneity). While this is obviously not the case for human, planetary, stellar or even galactic scales; it does seem to fit observations very well indeed if the scales considred are large enough (typically greater than 100Mpc [11]). Note, however, that this applies only for positions in space and not in time.

This part will start by introducing, without proof, three results from GR; the line element and Cartan's structural equations. It will then proceed to derive the Friedmann equations, and use them to derive some basic cosmological parameters[1].

The line element is

$$ds^2 = g_{\mu\nu} dx^\mu dx^\nu \tag{2.1}$$

[1]The GR part uses differential forms. For an introduction to forms, see for instance "http://www.math.purdue.edu/ dvb/preprints/diffforms.pdf".

where $g_{\mu\nu}$ is the *metric*, or the matrix containing information of the underlying space' geometry. The line element can be thought of as the squared change in position in 4–space.

The *Christoffel symbols* are

$$\Gamma^{i}{}_{k\ell} \equiv \frac{1}{2} g^{im} \left(\frac{\partial g_{mk}}{\partial x^{\ell}} + \frac{\partial g_{m\ell}}{\partial x^{k}} - \frac{\partial g_{k\ell}}{\partial x^{m}} \right) \tag{2.2}$$

Cartan's first structural equation is

$$\underline{d\omega}^{\mu} = -\underline{\Omega}^{\mu}{}_{\nu} \wedge \underline{\omega}^{\nu} \tag{2.3}$$

where

$$\underline{\Omega}^{\mu}{}_{\nu} = \Gamma^{\mu}{}_{\nu\alpha} \underline{\omega}^{\alpha} \tag{2.4}$$

and $\Gamma^{\mu}{}_{\nu\alpha}$ are the connection coefficients, the generalized Christoffel symbols[2]. Cartan's second structural equation is

$$\underline{R}^{\mu}{}_{\nu} = \underline{d\Omega}^{\mu}_{\nu} + \underline{\Omega}^{\mu}{}_{\alpha} \wedge \underline{\Omega}^{\alpha}{}_{\nu}. \tag{2.5}$$

Equations (2.3) and (2.5) are mathematical results concerning differential geometry, but may (and will) be used in later physical derivations.

2.1.1 The Robertson-Walker Metric

Special relativity teaches us that the distance in 4-space between two events at positions with sperical coordinates (t, r, θ, ϕ) and $(t+dt, r+dr, \theta+d\theta, \phi+d\phi)$ is given by the line element

$$ds^2 = -dt^2 + dr^2 + r^2 d\Omega^2 \tag{2.6}$$

where

$$d\Omega^2 \equiv d\theta^2 + \sin^2\theta d\phi^2. \tag{2.7}$$

This is true in a flat Minkowski space, with metric (in matrix representation)

$$g_{\mu\nu} = \eta_{\mu\nu} = \begin{pmatrix} -1 & 0 & 0 & 0 \\ 0 & 1 & 0 & 0 \\ 0 & 0 & 1 & 0 \\ 0 & 0 & 0 & 1 \end{pmatrix} \tag{2.8}$$

where the $\eta_{\mu\nu}$ is used in place of $g_{\mu\nu}$ for emphasis on this particular metric. In an expanding universe the physical distance between two points in space is dependent upon the time at which the distance is measured. For this

[2]The connection coefficients are called Christoffel symbols whenever one operates in a metric space with a coordinate basis.

reason the metric in a flat, expanding or contracting universe becomes, in matrix representation,

$$g_{\mu\nu} = \begin{pmatrix} -1 & 0 & 0 & 0 \\ 0 & a^2(t) & 0 & 0 \\ 0 & 0 & a^2(t) & 0 \\ 0 & 0 & 0 & a^2(t) \end{pmatrix} \tag{2.9}$$

where a is the universal scale factor at time t. This metric is called the Friedmann–Lemaître–Robertson–Walker metric (hereafter the Robertson–Walker metric or RW metric) for a flat space and can also be written (in spherical comoving[3] coordinates (χ, θ, ϕ))[4], where χ is the comoving radial part,

$$ds^2 = -dt^2 + a^2(t)\left[d\chi^2 + \chi^2 d\Omega^2\right]. \tag{2.10}$$

2.1.2 Curvature

A more general solution allows for the universe to be curved. The curvature of space refers to the possibility of non–Euclidian 3-space, where positive curvature means that the sum of all angles in a triangle is more than π, negative curvature means that the sum of all angles is less than π and no curvature (flat space) means that the sum of all angles in a triangle is equal to π. But introducing curvature confounds the equations a little. Including curvature produces the metric

$$ds^2 = -dt^2 + a^2(t)\left[d\chi^2 + S^2(\chi) d\Omega^2\right]. \tag{2.11}$$

This expression for the metric including curvature contains the factor S^2 that includes all information about the curvature. To evaluate this function it is necessary to introduce an orthonormal basis

$$\underline{\omega}^{\hat{t}} = \underline{d}t \tag{2.12}$$
$$\underline{\omega}^{\hat{\chi}} = a(t)\underline{d}\chi \tag{2.13}$$
$$\underline{\omega}^{\hat{\theta}} = a(t)S(\chi)\underline{d}\theta \tag{2.14}$$
$$\underline{\omega}^{\hat{\phi}} = a(t)S(\chi)\sin\theta\underline{d}\phi. \tag{2.15}$$

It is necessary to use Cartan's structural equations ((2.3) and (2.5)) to find the curvature forms:

$$\underline{d\omega}^{\hat{\mu}} = -\underline{\Omega}^{\hat{\mu}}{}_{\hat{\nu}} \wedge \underline{\omega}^{\hat{\nu}} \tag{2.16}$$

[3] See section 2.1.6

[4] Strictly speaking this is the RW line element. The difference between a metric and a line element is often ignored in physics as inconsequential, although there is a mathematical difference. The terms will be used interchangeably within this thesis.

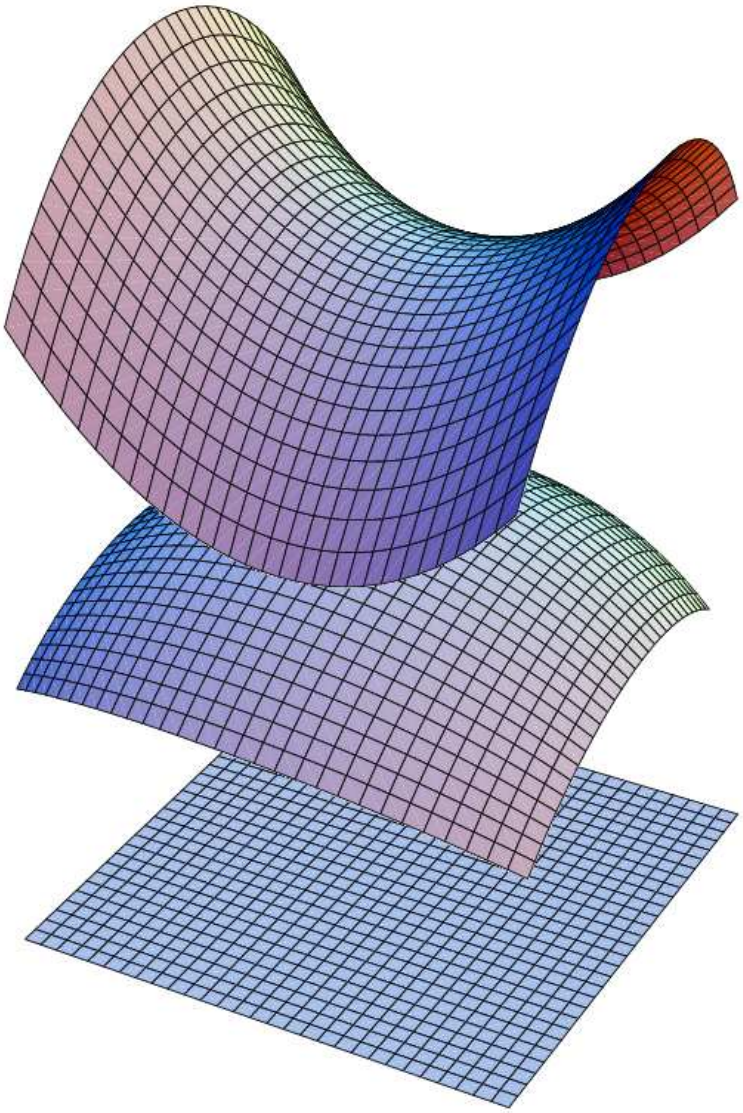

Figure 2.1: Curvature on a two dimensional surface; hyperbolic (negative) on top, elliptic (positive) in the middle and Euclidean (flat) on the bottom. This is analogue to the three dimensional curvature of the universe.

and

$$\underline{R}^{\hat{\mu}}{}_{\hat{\nu}} = \underline{d\Omega}^{\hat{\mu}}_{\hat{\nu}} + \underline{\Omega}^{\hat{\mu}}{}_{\hat{\alpha}} \wedge \underline{\Omega}^{\hat{\alpha}}{}_{\hat{\nu}}. \tag{2.17}$$

Evaluation produces

$$R^{\hat{t}}{}_{\hat{i}} = \left(\frac{\ddot{a}}{a}\right) \underline{\omega}^{\hat{t}} \wedge \underline{\omega}^{\hat{i}}, \tag{2.18}$$

$$R^{\hat{\chi}}{}_{\hat{j}} = \left(\frac{\dot{a}^2}{a^2} - \frac{S''}{Sa^2}\right) \underline{\omega}^{\hat{\chi}} \wedge \underline{\omega}^{\hat{j}} \tag{2.19}$$

and

$$R^{\hat{\theta}}{}_{\hat{\phi}} = \left(\frac{\dot{a}^2}{a^2} - \frac{1}{a^2 S^2} - \frac{(S')^2}{a^2 S^2}\right) \underline{\omega}^{\hat{\theta}} \wedge \underline{\omega}^{\hat{\phi}} \tag{2.20}$$

where in this case

$$S' \equiv \frac{\partial S}{\partial \chi}. \tag{2.21}$$

Isotropy also includes curvature, so the three spacial directions should be the same as long as an orthonormal basis is used. In other words:

$$\frac{S''}{a^2 S} = \frac{(S')^2}{a^2 S^2} - \frac{1}{a^2 S^2} \tag{2.22}$$

which implies

$$SS'' = (S')^2 - 1 \tag{2.23}$$

or

$$(S')^2 - SS'' = 1. \tag{2.24}$$

Because

$$\left(\frac{S'}{S}\right)' = \frac{SS'' - (S')^2}{S^2} \tag{2.25}$$

the differential equation (2.24) may be written

$$S^2 \left(\frac{S'}{S}\right)' = -1. \tag{2.26}$$

If this is multiplied by $2S'/S^3$,

$$2\frac{S'}{S}\left(\frac{S'}{S}\right)' = -2\frac{S'}{S^3} \tag{2.27}$$

is found. By integration;

$$\left(\frac{S''}{S}\right)^2 = \frac{1}{S^2} - \frac{k}{R_0^2} \tag{2.28}$$

so that multiplying with S^2 and taking the square root gives

$$S' = \sqrt{1 - \frac{kS^2}{R_0^2}}. \tag{2.29}$$

Here R_0 is the present value of the radius of the 3-space curvature (with dimension length), and k is a dimensionless constant of integration described whose sign determines the form of the curvature[12]:

$$k = \begin{cases} 1, & \text{if space is positively curved (elliptic)} \\ 0, & \text{if space is flat (Euclidean)} \\ -1, & \text{if space is negatively curved (hyperbolic).} \end{cases} \tag{2.30}$$

Integrating one final time produces

$$S(\chi) = \begin{cases} R_0 \sin\left(\frac{\chi}{R_0}\right), & \text{if } k > 0 \\ \chi, & \text{if } k = 0 \\ R_0 \sinh\left(\frac{\chi}{R_0}\right), & \text{if } k < 0 \end{cases} \tag{2.31}$$

and with this S, equation (2.11) is the general RW metric describing a simply connected (see section B.3.1), homogeneous, isotropic, expanding or contracting universe[13, 14, 15, 16]. It is important to note, however, that this equation is only a good approximation on very large scales where the assumption of homogeneity and isotropy is true. Fortunately, clusters and superclusters are sufficiently small to make this approximation very good, and in such an idealized universe, all information is contained in R_0 and $a(t)$.

2.1.3 Forceless Motion

In a Minkowski space a particle moving (or not) without any forces acting upon it the particle will move in a straight line. In a more general space curvature must be factored in. For a particle without any forcing acting upon it, general relativity states that it will follow a *geodesic*; that is a generalization of the straight line to a curved space.

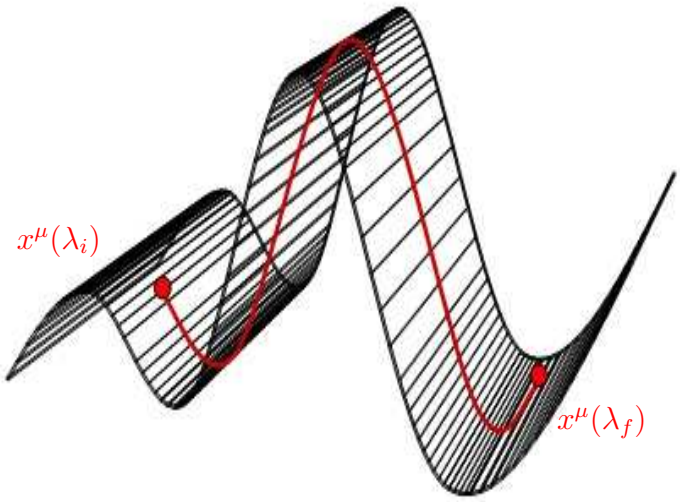

Figure 2.2: A geodesic curve parametrized by λ. λ increases monotonically from λ_i to λ_f. However the physical significance of this parameter is not a concern as it will always vanish in the final expression. This figure also illustrates the general concept of a geodesic — a curve is restricted to moving on a surface and will try to minimize the distance covered, but not be able to make the line straight. This is the way a test particle will move in free fall.

The particle will have its trajectory determined by the metric of the space it is moving through. For a particle moving along a path parametrized by the parameter λ, the geodesic equation becomes

$$\frac{d^2x^\mu}{d\lambda^2} = -\Gamma^\mu{}_{\alpha\beta}\frac{dx^\alpha}{d\lambda}\frac{dx^\beta}{d\lambda} \tag{2.32}$$

where $\Gamma^\mu{}_{\alpha\beta}$ is the Christoffel symbols

$$\Gamma^\mu{}_{\alpha\beta} \equiv \frac{g^{\mu\nu}}{2}\left(\frac{\partial g_{\alpha\nu}}{\partial x^\beta} + \frac{\partial g_{\beta\nu}}{\partial x^\alpha} - \frac{\partial g_{\alpha\beta}}{\partial x^\nu}\right) \tag{2.33}$$

where $g_{\mu\nu}$ is the metric. In cosmology this is complicated because the metric changes with time, but the fortunate thing for the isotropic and homogeneous universe with metric as given in (2.9) is that the metric is zero exept for the diagonal. In addition the first index of that diagonal is constant so that the Christoffel symbols reduce to

$$\Gamma^0{}_{ij} = \delta_{ij}\dot{a}a \tag{2.34}$$

$$\Gamma^{i}{}_{0j} = \Gamma^{j}{}_{0i} = \delta_{ij}\frac{\dot{a}}{a} \tag{2.35}$$

where latin and greek indexes are as described in section B.1 and

$$\dot{a} \equiv \frac{da}{dt}. \tag{2.36}$$

All other $\Gamma^{\mu}{}_{\alpha\beta}$ equal zero[10].

2.1.4 Friedmann and his Fluids

To say anything about the universe, it is necessary to see what the contents of the universe will do to it. All matter will be approximated as fluids on the large scale. Starting with the general Einstein tensor describing the geometry of the universe,

$$G_{\mu\nu} \equiv R_{\mu\nu} - \frac{g_{\mu\nu}\mathcal{R}}{2} = 8\pi G T^{\mu\nu} \tag{2.37}$$

where $R_{\mu\nu}$ is the Ricci tensor describing the metric and the derivatives of the metric,

$$\mathcal{R} \equiv g^{\mu\nu}R_{\mu\nu} \tag{2.38}$$

is the Ricci scalar and $T^{\mu\nu}$ is the energy-momentum tensor defined as

$$T^{\mu}{}_{\nu} \equiv \begin{pmatrix} -\rho & 0 & 0 & 0 \\ 0 & \mathcal{P} & 0 & 0 \\ 0 & 0 & \mathcal{P} & 0 \\ 0 & 0 & 0 & \mathcal{P} \end{pmatrix}, \tag{2.39}$$

the Friedmann equations may be derived. Here ρ is the (total) energy density of the universe and $\mathcal{P}$ is the fluid pressure of the substance making up that energy. In order to derive the Friedmanns equations, consider the Ricci tensor expressed as

$$R_{\mu\nu} = \Gamma^{\alpha}{}_{\mu\nu,\alpha} - \Gamma^{\alpha}{}_{\mu\alpha,\nu} + \Gamma^{\alpha}{}_{\beta\alpha}\Gamma^{\beta}{}_{\mu\nu} - \Gamma^{\alpha}{}_{\beta\nu}\Gamma^{\beta}{}_{\mu\alpha} \tag{2.40}$$

where $\Gamma^{\alpha}{}_{\mu\nu,\alpha}$ is as defined in section B.1.3. For a universe described by the RW metric the Christoffel symbols are as described by equations (2.34) and (2.35) and thus the Ricci tensor for the space-space component is

$$R_{ij} = \delta_{ij}\left(2\dot{a}^2 + a\ddot{a}\right) \tag{2.41}$$

and the time-time component is

$$R_{00} = 3\frac{\ddot{a}}{a}. \tag{2.42}$$

The time-space components, R_{0i} and R_{i0} are zero [10]. The Ricci scalar, found from equation (2.38), is

$$\mathcal{R} = g^{\mu\nu}R_{\mu\nu} = -R_{00} + \frac{1}{a^2}R_{ii} = 6\left(\frac{\ddot{a}}{a} + \frac{\dot{a}^2}{a^2}\right). \tag{2.43}$$

If the time-time part of equation (2.37) is considered, one can calculate the evolution of a. The equation then reduces to

$$G_{00} = R_{00} - \frac{g_{00}}{2}\mathcal{R} = 8\pi G T_{00} \tag{2.44}$$

This is then the *first Friedmann equation*, more commonly written as

$$H^2 = \frac{8\pi G\rho}{3}. \tag{2.45}$$

where

$$H \equiv \frac{\dot{a}}{a} \tag{2.46}$$

is the Hubble rate that describes how fast the scale factor changes. This is the equation for a universe with no curvature and no cosmological constant. The complete equation is written as

$$H^2 = \frac{8\pi G\rho}{3} - \frac{1}{a^2}\frac{k}{R_0^2}. \tag{2.47}$$

If no curvature is assumed, $k = 0$ and equation (2.45) is regained. In this case the energy density is

$$\rho = \frac{3H^2}{8\pi G}. \tag{2.48}$$

If the value of the Hubble parameter seen in present time, the Hubble constant

$$H_0 = \frac{1}{a_0}\frac{da(t_0)}{dt} \tag{2.49}$$

where a_0 is the value of the scaling parameter today ($H_0 \approx 72km/s/kpc$ (see section A), the *critical density* may be defined as

$$\rho_{\text{cr}} \equiv \frac{3H_0^2}{8\pi G} \tag{2.50}$$

and is the constant[5] density that, given all other parameters, keeps the universe from having curvature in the absence of dark energy (see section 2.2.4). With the critical density, it is possible to define the *density parameter*

$$\Omega \equiv \frac{\rho}{\rho_{\text{cr}}}, \tag{2.51}$$

[5]The Hubble rate is not constant, but depends upon the time at which it is measured, and because of that so does the critical density. Although the values of these may be quite different when cosmological time scales are considered, the convention is to adopt the values the critical density have today.

and with this the first Friedmann equation then becomes

$$1 - \Omega = -\frac{k}{R_0^2 a^2 H^2}. \tag{2.52}$$

Fluids

Having supposed homogenity and isotropy, it follows that whatever energy is present in the universe is considered to be perfectly evenly distributed. Noethers Theorem teaches us that for any closed system total energy is always conserved[6]. This is commonly expressed through the first law of thermodynamics:

$$dQ = dE + PdV \tag{2.53}$$

where P is pressure, dE is the net change in internal energy, dV is the change in volume and dQ is the net flow of energy in or out of the system [17]. In an isotropic and homogeneous universe there is no net flow of energy in or out of such a system (for if it was, there would soon be more or less of it in one place!) such that $dQ = 0$. This would imply that (2.53) for such a system is

$$\frac{dE}{dt} + P\frac{dV}{dt} = 0 \tag{2.54}$$

or

$$\dot{E} + P\dot{V} = 0. \tag{2.55}$$

But the universe is expanding. Any comoving volume of space would have its size dependent on the cube of the scale factor so that for instance a cube of comoving length l is

$$V(t) = l^3 a^3(t) \tag{2.56}$$

so that

$$\dot{V} = 3l^3 a^2(t)\dot{a} = 3V\frac{\dot{a}}{a} = 3VH. \tag{2.57}$$

The internal energy is

$$E(t) = \rho(t)V(t) \tag{2.58}$$

[6]If the universe is a "closed" system *in a thermodynamic context*, this should also be true on a global scale. That is at least at first glance not the case; as will be shown, photons loose energy because of the expansion of the universe, but not in proportion to the energy gained when vacuum energy is conserved. The question of total energy in the universe is in general a very unpleasant and nontrivial one that is still not fully resolved, indeed it is not agreed upon what the question should even mean. From here on a "closed system" in the thermodynamic sence will be taken to be a small patch of space under the influence of cosmic expansion.

and so

$$\dot{E} = V\dot{\rho} + \rho\dot{V} = V\left(\dot{\rho} + 3H\rho\right). \tag{2.59}$$

Putting this into equation (2.53) yields

$$V\left(\dot{\rho} + 3H\left(\rho + P\right)\right) = 0. \tag{2.60}$$

This will be referred to as the *fluid equation*.

To obtain the final equation of state the first Friedmann equation is multiplied by a^2 and derivated with respect to time,

$$2\dot{a}\ddot{a} = \frac{8\pi G}{3}\left(\dot{\rho}a^2 + 2\rho a\dot{a}\right). \tag{2.61}$$

Dividing by $2a\dot{a}$ gives

$$2\frac{\ddot{a}}{a} = \frac{4\pi G}{3}\left(\frac{\dot{\rho}}{H} + 2\rho\right). \tag{2.62}$$

By substituting, from equation (2.60), an expression for $\dot{\rho}/H$,

$$\frac{\dot{\rho}}{H} = -3(\rho + P), \tag{2.63}$$

into (2.62)

$$\frac{\ddot{a}}{a} = -\frac{4\pi G}{3}\left(\rho + 3P\right) \tag{2.64}$$

is obtained. This is the acceleration equation or the *second Friedmann equation*. This equation provides a relationship between the acceleration in expansion and the energy density and pressure of the universe. A positive right hand side will mean accelerating expansion, but can only happen if $3P < -\rho$, in other words if either pressure is negative ("tension") or if energy density is negative ("unphysical") [7].

This gives us two independent equations and four unknowns. To solve them, initial conditions are needed. These can only be found by experiment and physical reasoning, and the values to best knowledge today are repeated in appendix A.

2.1.5 Redshift

The notion of an expanding universe begs the question of how light will be affected by moving in an expanding medium. Both special and general relativity states that light moves such that the line element,

$$ds^2 = -dt^2 + dx^2 + dy^2 + dz^2 = 0. \tag{2.65}$$

[7] Or is it? The photons have already lost energy, if total energy (and thus energy density) started at zero as has been claimed [18] it would be negative now if vacuum energy can be neglected.

If one places the x direction along the path of a photon, this becomes

$$0 = -dt^2 + dx^2 \Rightarrow \frac{dx}{dt} = \pm 1 \tag{2.66}$$

in the special relativity case. Locally one may use special relativity even in a universe with $k \neq 0$ in the special case for $ds^2 = 0$. Because ds^2 is a scalar, this will be true for all frames of reference. To include the expansion of the universe;

$$ds^2 = 0 = dt^2 a^2(t) \frac{dx^2}{1 - kx^2} \tag{2.67}$$

produces

$$\frac{dt}{a(t)} = -\frac{dx}{\sqrt{1 - kx^2}}. \tag{2.68}$$

Consider now a wave of light emitted at a point x and a time t_e and received at the origin and time t_r. The first peak is then emitted at t_e and the second peak is emitted at $t_e + \delta t_e$ and these peaks are received at times t_r and $t_r + \delta t_r$ respectively.

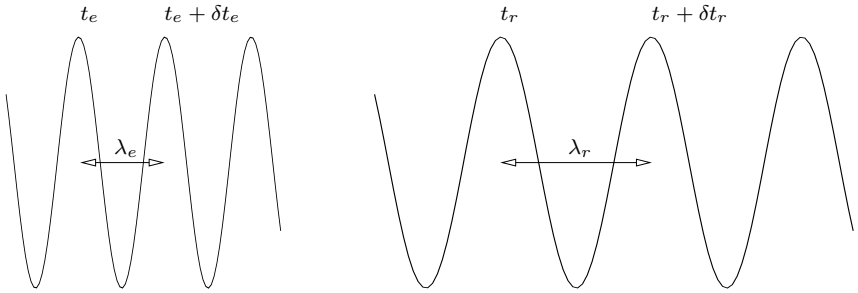

Figure 2.3: Cosmological redshift is caused directly by the expansion of the universe — the wave is stretched along with the rest of space.

Equation (2.68) then becomes

$$\int_{t_e}^{t_r} \frac{cdt}{a(t)} = -\int_{x}^{0} \frac{dx}{\sqrt{1 - kx^2}} \tag{2.69}$$

and

$$\int_{t_e + \delta t_e}^{t_r + \delta t_r} \frac{dt}{a(t)} = -\int_{x}^{0} \frac{dx}{\sqrt{1 - kx^2}} \tag{2.70}$$

for the first and second peak respectively. In other words

$$\int_{t_e}^{t_r} \frac{dt}{a(t)} = \int_{t_e + \delta t_e}^{t_r + \delta t_r} \frac{dt}{a(t)}. \tag{2.71}$$

The integrals on either side may be split so that

$$\int_{t_e}^{t_e+\delta t_e} \frac{dt}{a(t)} + \int_{t_e+\delta t_e}^{t_r} \frac{dt}{a(t)} = \int_{t_e+\delta t_e}^{t_r} \frac{dt}{a(t)} + \int_{t_r}^{t_r+\delta t_r} \frac{cdt}{a(t)}. \tag{2.72}$$

Subtracting the factor $\int_{t_e+\delta t_e}^{t_r} \frac{cdt}{a(t)}$ on both sides produces

$$\int_{t_e}^{t_e+\delta t_e} \frac{cdt}{a(t)} = \int_{t_r}^{t_r+\delta t_r} \frac{cdt}{a(t)}. \tag{2.73}$$

These two integrals are integrals over time, which means $a(t)$ might change. Luckily, the time intervals are very small, so that $a(t)$ may be considered constant (although $a(t_e) \neq a(t_r)$). Evaluating the now easy integrals and dividing both sides by c produces

$$\frac{\delta t}{a(t_e)} = \frac{\delta t_r}{a(t_r)}. \tag{2.74}$$

This means that

$$\frac{\delta t_e}{\delta t_r} = \frac{a(t_e)}{a(t_r)} \tag{2.75}$$

or, as the speed of light is constant and the wavelength $\lambda \propto \delta t$,

$$\frac{\lambda_r}{\lambda_e} = \frac{a(t_r)}{a(t_e)}. \tag{2.76}$$

Finally, one may introduce the *redshift parameter*

$$z \equiv \frac{\lambda_r}{\lambda_e} - 1 = \frac{a(t_r)}{a(t_e)} - 1 \tag{2.77}$$

commonly used throughout cosmology to measure redshift.

Redshift measurements have several advantages. First of all, it is very easy to measure accurately. Second, because of this relationship, one may know how much the universe has expanded since light was emitted, and by knowing the expansion rate for the universe, one may deduce the time and distance to the emitter.

2.1.6 Distance

The distance between two points is, in most aspects of human endeavour, usually an easy thing to define (even if it is not always easy to measure in practice). On cosmological scales, however, this is no longer the case. Two problems arise; the universe is not static, it may expand and contract, and it is not necessarily Euclidian. The three most common are the proper distance, the angular diametre distance and the luminocity distance.

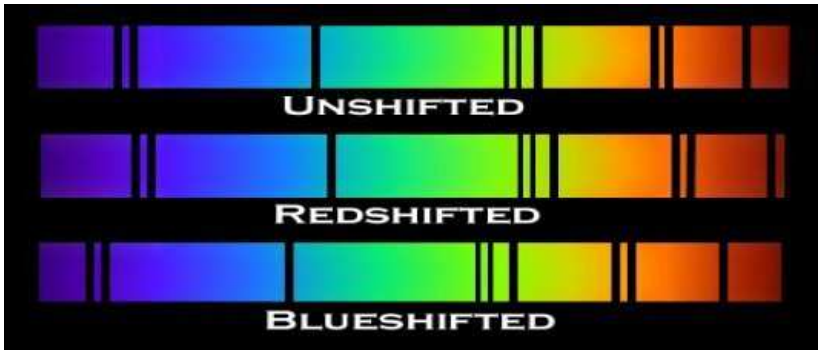

Figure 2.4: Measuring redshift or blue shift of light emitted from a distant source is possible by comparing lines in the spectrum. Because these lines can be very narrow, it is possible to measure redshift (or blue shift) very accurately.

Comoving Distance

In addition to the three mentioned, the comoving distance between two points may be defined. This is a number that remains constant under the expansion of the universe, so that a comoving distance between points A and B is the same for all times.

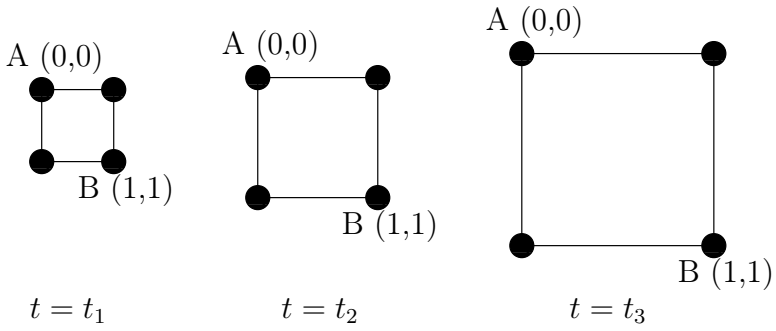

Figure 2.5: The comoving distance between points A and B is the same for all times (in this case $\sqrt{2}$ in the coordinates chosen), as long as they have no proper motion. The physical distance, however, changes as the scaling factors $a(t_1)$, $a(t_2)$ and $a(t_3)$ are all different ($a(t_1) < a(t_2) < a(t_3)$). In an expanding universe this implies that $t_1 < t_2 < t_3$, but this need not necessarily be the case; a contracting universe would reverse the order.

Proper Distance

To define the *proper distance*, imagine the expantion of the universe to be halted at time t_0 and the required number of standard measuring rods placed

along a geodesic from an origin A towards the target B. The resulting length is the proper distance between A and B at time t_0.

So, assuming an observer being located with spacial coordinates $(0, 0, 0)$ measuring the distance to an object with spacial comoving coordinates χ, θ, ϕ, the RW line element (in spherical coordinates) is

$$ds^2 = -dt^2 + a^2(t_1)\left[d\chi^2 + S^2(\chi)d\Omega^2\right] \tag{2.78}$$

at a time t_1. As any peculiar motion is ignored, the angles will remain constant and $d\phi = d\theta = 0$ (and hence $d\Omega = 0$). The geodesic considered is constant in time ($t = t_1$, $dt = 0$), but moves along the spacial path $d\chi$. This produces a line element of

$$ds^2 = a^2(t)d\chi. \tag{2.79}$$

This may be integrated to produce the proper distance

$$d_p(t_1) = a(t_1)\int_0^{\chi} d\chi = a(t_1)\chi \tag{2.80}$$

To get the true spacial distance the spacial coordinate

$$r \equiv S(\chi) \tag{2.81}$$

is introduced so that

$$\chi = S^{-1}(r) \tag{2.82}$$

where

$$S^{-1}(r) = \begin{cases} \frac{1}{R_0(t_1)}\sin^{-1}\left[\frac{r}{R_0(t_1)}\right], & \text{if } k > 0 \\ r, & \text{if } k = 0 \\ \frac{1}{R_0(t_1)}\sinh^{-1}\left[\frac{r}{R_0(t_1)}\right], & \text{if } k < 0 \end{cases} \tag{2.83}$$

may be obtained from inverting equation (2.31). Substituting r for χ in equation (2.80) then produces

$$d_p(t_1) = a(t_1)S^{-1}(r). \tag{2.84}$$

The proper distance is perhaps the most intuitive cosmological measure, but in an expanding universe it is not easy to measure directly[8]. It is, however, a good way to illustrate the expansion rate of the universe at earlier epochs because of the linear relationship between $d_p(t)$ and $a(t)$ given r.

[8]It is, after all, not an easy task to move cosmological distances let alone halt the expansion of the universe!

Luminosity Distance

Whenever a point in space emits light, the luminosity L is defined as the total energy emitted per unit time and it is

$$L = 4\pi d^2 l \tag{2.85}$$

where d is the distance to the point source and l is the flux of energy per unit square. This may be inverted to

$$d = \sqrt{\frac{L}{4\pi l}}. \tag{2.86}$$

In cosmology the *luminosity distance*, d_L, is defined to be the distance at which equation (2.85) is true so that

$$d_L \equiv \sqrt{\frac{L}{4\pi l}}. \tag{2.87}$$

Whenever this distance is calculated, the light observed at a time t_0 has been red shifted by a factor

$$z + 1 = \frac{a_0}{a(t_e)}. \tag{2.88}$$

Also;

$$\delta t_0 = \frac{a(t_0)}{a(t_e)} \delta t_e \tag{2.89}$$

where t_e is when the light was emitted. The deceived flux is

$$l = \frac{L}{4\pi a^2(t_0) r^2} \left(\frac{a(t_e)}{a(t_0)} \right)^2 = \frac{L}{4\pi a^2(t_0) r^2} \frac{1}{(1+z)^2}. \tag{2.90}$$

Inserting this into the expression (2.87) for d_L results in

$$d_L = \sqrt{\frac{L}{4\pi \frac{L}{4\pi a^2(t_0) r^2 (1+z)^2}}} = a(t_0) r (1+z) \tag{2.91}$$

where r is defined in equation (2.81).

So far so good, but for this measure to be made one needs to know the emitted luminosity from the observed object and this is typically not so easy. *Standard Candles* are objects whose light profile *are* known from physics, and they are much treasured by astronomers. Type 1a supernovae is used as standard candles on very large scales, because they have a very well known emittance profile and they are bright enough to be observed on cosmological scales.

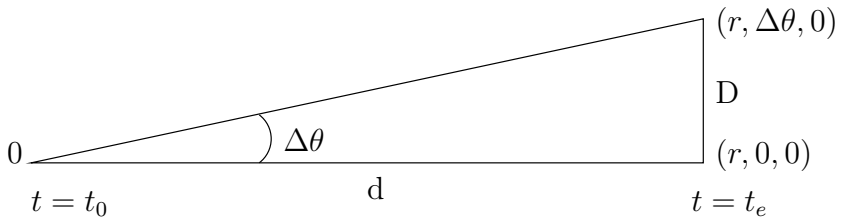

Figure 2.6: Cosmological redshift is caused directly by the expansion of the universe — the wave is stretched along with the rest of space.

Angular Diameter Distance

Where the proper distance describes the distance along a geodesic at a given time t_1, the *angular diameter distance* describes how much of the sky a certain object with known size will occupy. The angular diameter of an object of length D will take in a flat metric is calculated from

$$\frac{D}{d_A} \approx \Delta\theta \tag{2.92}$$

where d_A is the angular diameter distance from observer to the object and assuming $D \ll d_A$ (so that $\sin\Delta\theta \approx \Delta\theta$). If light from the object is emitted at a time t_e, and the extremes (the two points with distance D between them) of the emitter is assumed to be placed at points in space equal to $(r, 0, 0)$ and $(r, \Delta\theta, 0)$, the line element becomes

$$ds^2 = -r^2 a^2(t_e)(\Delta\theta)^2 = -D^2, \tag{2.93}$$

so that

$$D = a(t_e) r \Delta\theta. \tag{2.94}$$

From the definition of angular diameter distance in equation (2.92) is then realized

$$d_A = \frac{D}{\Delta\theta} = a(t_e) r = \frac{a(t_e)}{a_0} a_0 r, \tag{2.95}$$

or

$$d_A = \frac{a_0}{1+z} r. \tag{2.96}$$

This implies that the angular diameter distance has some strange properties. Even in a flat, expanding and relatively benign universe the $1 + z$ in the denominator causes the distance to be suppressed at truly large z so that at some point d_A will begin to decrease for increasing z.

2.1.7 Conformal Time and Horizons

Conformal time is defined to be

$$d\eta \equiv \frac{dt}{a} \tag{2.97}$$

or on integral form

$$\eta = \int_0^t \frac{dt'}{a(t')}. \tag{2.98}$$

If one integrates this to the current value for t, t_0, the conformal time is equal to the comoving coordinate value for *particle horizon* in a given model of the universe. This quantity is the furthest away any particle we receive today could have originated (had it moved with the speed of light). In standard time it is defined to be at the proper distance

$$d_p^{ph}(t) = a(t) \int_0^t \frac{dt'}{a(t')}. \tag{2.99}$$

While not all universe models have theoretical particle horizons, it is not currently possible to observe further back than the *last scattering surface*, the time at which photons decoupled to become the cosmic microwave background (see section 2.3) no matter what universe model is preferred.

The *event horizon* is the greatest comoving distance from which light (or particles) emitted today (that is $t = t_0$) may reach us at some point in the future. The proper distance to the event horizon in a given universe model is

$$d_p^{eh}(t) = a(t) \int_{t_0}^{\infty} \frac{dt'}{a(t')} \tag{2.100}$$

2.2 Contents of the Universe

The universe contains stuff. In terms of the basic cosmological equations, this may be known as the density parameter, Ω, is defined in equation (2.51). This parameter may be split into several parts such that

$$\Omega = \sum \Omega_i = \Omega_k + \Omega_{CDM} + \Omega_b + \Omega_r + \Omega_\nu + \Omega_\Lambda = 1 \tag{2.101}$$

where Ω_k is density from curvature, Ω_{CDM} is density from cold dark matter, Ω_b is the density from ordinary (baryonic) matter, Ω_r is the density from radiation, Ω_ν is the neutrino density and Ω_Λ is the density from the cosmological constant or dark energy.

The *equation of state* for either of these components may be described as

$$p = w\rho \tag{2.102}$$

so that if one knows w in either case, p may be found. Substituting this into equation (2.63) and multiplying by H,

$$\dot{\rho} = -3H(1+w)\rho \tag{2.103}$$

is found. This differential equation may be integrated with present values ρ_0 and a_0 as boundary conditions to find

$$\rho = \rho_0 \left(\frac{a_0}{a}\right)^{3(1+w)}. \tag{2.104}$$

Equation (2.104) explains the time evolution of the density. For the equation to make any sense the parameter w must be known, and this must be determined separately in each case.

2.2.1 Ω_k

Of these Ω_k is perhaps both the easiest and the hardest to follow. Although it's not energy per se, it does influence the Friedmann equations, and so if all other parameters are known, it would fall out naturally. One can calculate that it has $w = -1/3$ and by that from (2.102)

$$p = -\frac{1}{3}\rho. \tag{2.105}$$

This implies that (2.104) becomes

$$\rho_k = \rho_{k0} \left(\frac{a_0}{a}\right)^2 \tag{2.106}$$

so that the "energy density" of curvature follows the somewhat counter–intuitive $V^{-2/3}$. The easy thing about it is that as it seems the universe is indeed very close to being flat [19], Ω_k does not seem to matter[9].

2.2.2 Dust

Dust is all matter and cold dark matter (abbreviated CDM) that is moving at non-relativistic speeds. For the purpose of cosmological calculations, dust is considered to have no or negligible momentum. Both matter and CDM are very similar in that they have

$$w = \frac{\langle v^2 \rangle}{3} \tag{2.107}$$

and since dust has $v \ll c$, $w \approx 0$. This gives them the same equation of state,

$$p = 0, \tag{2.108}$$

[9] These measurements, conducted by looking at the CMB as well as type 1a supernovae and baryon acoustic oscillation data do not agree with a universe that is hyperbolic.

and the same gravitational behavior. Although matter form compact structures and cold dark matter does not, they do by and large behave the same way from a cosmological point of view. The reason to differentiate between either is that while ordinary matter couples to electromagnetism, CDM does not; and while this will be of consequence in an early radiation dominated epoch. The density, also being the same, is

$$\rho_m = \rho_{m0} \left(\frac{a(t)}{a_0} \right)^3 \tag{2.109}$$

where ρ_{m0} is the density at present time. This is a very simple result realized from the fact that 3–space increases by it's diameter cubed.

The true nature of the dark matter is still a matter for debate (although it is hoped the LHC will shed some light on the question, see for instance [20]), but fortunately its nature matters little for the generalized cosmology except that it needs to be there to account for the rate structure formation. What is clear is that it couples either not at all or extremely weakly to the electromagnetic force, and that it may feel the strong and weak nuclear interactions apart from normal gravitational interaction. A universe consisting only of CDM (and curvature) was very popular amongst cosmologists until the late 1990's when it was shown that the universe is actually accelerating[21, 22]. The currently accepted values for dust are

$$\Omega_{CDM} = 0.21 \tag{2.110}$$

and

$$\Omega_b = 0.044 \tag{2.111}$$

2.2.3 Radiation

In cosmological terms radiation is whatever is moving at ultra-relativistic speeds. This includes both normal electromagnetic radiation and other ultra-relativistic particles. Neutrinos (Ω_ν) are considered to be radiation because even if they are not completely massless, most of their energy is contained as motion. They will, however, couple only very weakly to matter and be decoupled much earlier. In an idealized situation, radiation has an equation of state of [17]

$$p = \frac{\rho}{3}, \tag{2.112}$$

in other words, it has a $w = 1/3$. From this it is realized that equation (2.104) becomes

$$\rho_r = \rho_{r0} \left(\frac{a_0}{a} \right)^4 . \tag{2.113}$$

This should be noted for two reasons. First; the rate of decrease in density is *faster* than the increase in volume. This can be understood both from it's equation of state and from the fact that light traveling in an expanding universe is red shifted, and hence looses energy, as explained in 2.1.5 with a factor proportional to a as well as the $1/a^3$ from volume increase. Second; it has consequences for the time evolution of the universe. In it's extreme, it implies that for a nonzero radiation density, there must have been a time where radiation dominated total the energy density in the universe. Currently accepted values for radiation densities today is

$$\Omega_\gamma = 10^{-5} \tag{2.114}$$

and

$$\Omega_\nu = 10^{-6} \tag{2.115}$$

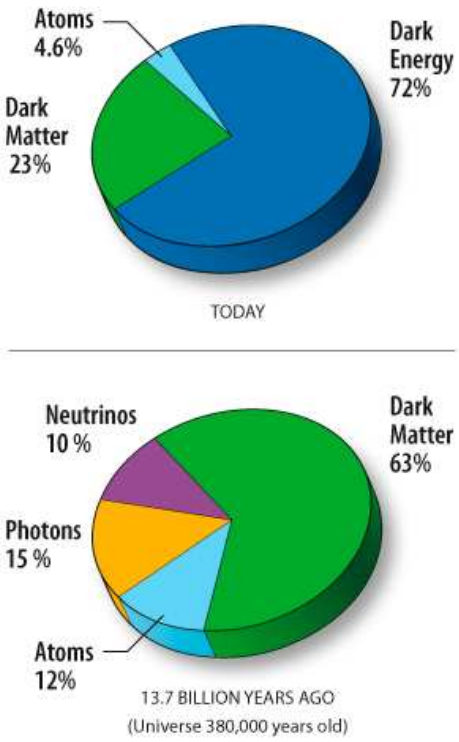

Figure 2.7: The composition of the universe today and 380 000 years after the Big Bang as derived from the WMAP 5 year data by the NASA/WMAP Science Team.

2.2.4 Dark Energy

While the curvature, matter and radiation is well understood and dark matter at least has several candidate theories, there is no consensus what the dark energy is. It was observed in 1998-1999, however, that the expansion of the universe seems to be accelerating [21, 22]. The acceleration observed is consistent with a cosmological constant, Λ, taken to be such that its $w = -1$ so that

$$\rho_\Lambda = \frac{\Lambda}{8\pi G} \tag{2.116}$$

and

$$p_\Lambda = -\rho_\Lambda \tag{2.117}$$

or constant in both cases. Although the today popular ΛCDM model uses the cosmological constant to account for the mysterious acceleration, it is by no means the only suggestion put forward to account for this (see for instance [23]). In any case, the currently accepted best fit parameter for dark energy is

$$\Omega_\Lambda = 0.72 \tag{2.118}$$

at present time. One can thus say that we live in a dark energy dominated universe.

2.3 The Early Universe

One of the first and most important consequences of the Friedmann equations ((2.45) and (2.64)) is the dynamic nature of the universe; i.e. it must either be expanding or contracting. When Edwin Hubble showed in 1929 that galaxies further away from us move away with greater speed than the ones closer to us, it became immediately obvious that in an expanding universe put in reverse matter moves closer together[24][10]. In other words there must have been a time at which the matter in the present day galaxies was close enough for significant heating to occur and that heat would be transmitted through radiation, some of which should still be around; pointing to the existence of the *cosmic microwave background* abbreviated CMB. While the calculations shown above were all made well before the 1960's, the existence

[10] Although Hubble in his well known paper actually did not get a very good detection of the red shift, the findings were solid enough for him to convince Einstein. The rate of the Hubble parameter, however was way off (he predicted it to be around 500 kpc/s/Mpc). This lead to an estimated age of the universe of around 2 billion years at a time when it was known that the Earth is more than 4 billion years old, causing many to take it as evidence *against* the Big Bang theory.

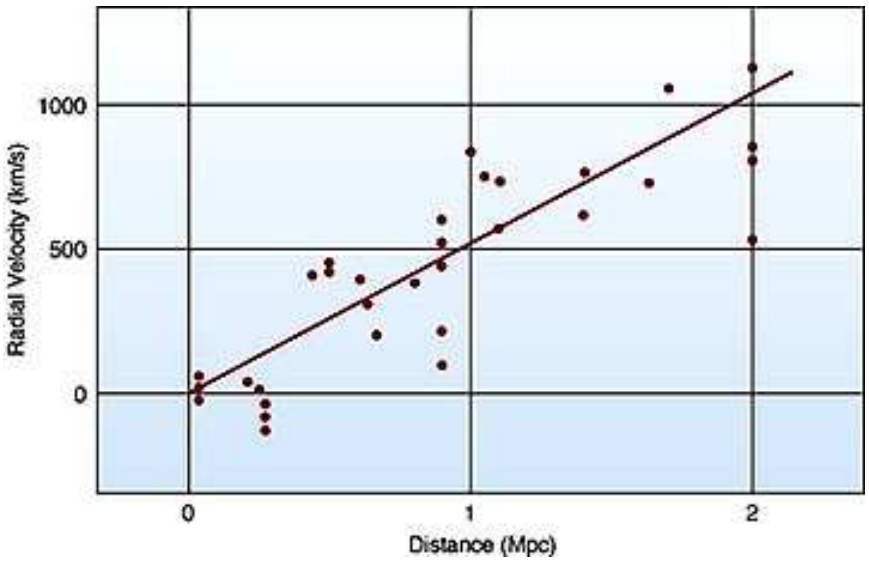

Figure 2.8: The galaxies measured by Hubble. The idea is right, the slope and hence the Hubble parameter is wrong.

of such a CMB remained controversial, and before it's initial detection in 1964 by Arno Penzias and Robert Woodrow Wilson the rival *steady state theory*, contending that an expanding universe could indeed be possible, but that matter was created continuously (at a very low rate) rather than at the beginning, had its proponents.

2.3.1 Primordial Perturbations

In order for galaxies, stars, planets gas clouds or any other form of structures to form, a perfectly smooth metric will not do. There must be some form of tiny inhomogeneities that such structures may grow out from. It is therefore necessary to perturb the metric in order to get the required equations.

Gravity Perturbations

In the Newtonian limit of general relativity, a particle moving in a static gravity potential will experience an acceleration

$$\frac{d^2x^i}{dt^2} = -\frac{\partial\Psi}{\partial x^i}, \tag{2.119}$$

where Ψ is the potential. Performing the same calculation in the framework of general relativity, it is clear that as this is the Newtonian limit, the difference between this and the standard Minkowski metric (2.8) is small. If one splits the new metric into two parts

$$g_{\mu\nu} = \eta_{\mu\nu} + h_{\mu\nu} \tag{2.120}$$

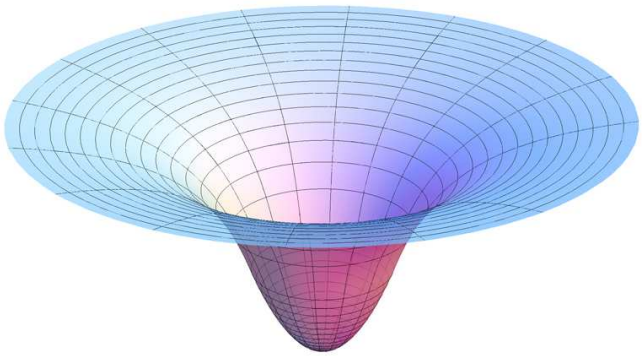

Figure 2.9: Static, spherical Newtonian gravity potential Ψ. from Wikimedia Commons

where $\eta_{\mu\nu}$ is the standard Minkowski metric and $h_{\mu\nu}$ is the small correction, it is possible to calculate that

$$\frac{d^2x^i}{dt^2} = \frac{1}{2}\frac{\partial h_{00}}{\partial x^i}. \tag{2.121}$$

The equations (2.119) and (2.121) are the same, so that in the Newtonian limit, $h_{00} = -2\Psi$. In other words,

$$g_{\mu\nu} = \eta_{\mu\nu} + h_{\mu\nu} = \begin{pmatrix} -1-2\Psi & 0 & 0 & 0 \\ 0 & a^2(t) & 0 & 0 \\ 0 & 0 & a^2(t) & 0 \\ 0 & 0 & 0 & a^2(t) \end{pmatrix} \tag{2.122}$$

so that

$$ds^2 = -(1+2\Psi)dt^2 + (1-\Psi)(dx^2+dy^2+dz^2). \tag{2.123}$$

is the line element (in Cartesian coordinates).

It should be noted that *in the Newtonian limit* it is irrelevant what the factor in front of the spacial part is. Therefore it is possible to introduce a so called *conformal Newtonian Gauge* where the perturbed metric is

$$ds^2 = -(1+2\Psi)dt^2 + a^2(1-\Phi)(dx^2+dy^2+dz^2). \tag{2.124}$$

2.4 Inflation

In the early 80's there were three problems facing cosmologists:

1. The horizon problem: The CMB temperature seems to be *too* homogeneous, with temperatures being the same everywhere in the observable universe even if the gas on antipodal points have never been in casual contact.

2. The flatness problem: The universe seems to lack any spacial curvature. Calculation shows that even a very small initial curvature would grow over time, so the lack of curvature today places extremely tight limits on what could have been initial curvature.

3. The monopole problem: The universe should contain some magnetic monopoles according after the initial high energy era. None have been observed.

Inflation is one of the most popular solutions to these problems. The basic idea is that the universe, which is expanding now with some time dependent scale factor a(t), starts expanding faster and faster. Expansion means that the scale factor changes with time, d a(t)/dt is nonzero. For inflation, this change in the scale factor changes with time as well, that is, the scale factor accelerates:

$$\frac{d^2a(t)}{dt^2} > 0. \tag{2.125}$$

The effect of this is to dilute away all the inhomogeneities in space, such as monopoles predicted by many high energy theories (one of the early motivations), or any other sort of fluctuations. The number density of particles goes to zero, since space is expanding so fast.

Horizons

A special feature of inflation is its effect on horizons. The horizon demarcates the boundary of causally connected regions, regions that light rays (which travel at the fastest speed that any signal can travel) can reach since the time of the big bang. These regions grow over time, as light has more time to travel, but the expansion of the universe means that over time there is more space to cross as well. When the universe isn't inflating, such as now, regions which are larger and larger come inside the horizon and become causally connected. During inflation, the expansion of the universe wins out. Regions which were causally connected are separated so fast by the expansion of space that a region once in causal contact can have parts of it "pushed out" of the horizon. Thus we expect scales larger than our horizon would not be correlated (that is, were once able to affect each other causally) unless inflation occurred. For example, the Cosmic Microwave background is homogeneous on scales which were not in causal contact when the signal was created, and thus suggests we need something like inflation to explain its homogeneity.

What's Left?

During inflation, the only reason that space doesn't become completely boring is that "empty space" can have energy (and does during inflation, as will

be seen below) and that "empty space" also always has quantum fluctuations. These quantum fluctuations can provide the seeds for the formation of structure after inflation ends.

Inflation can end when the energy in "empty space" goes back into (kinetic) energy for the fields in space, turning into a bath of particles ("reheating"). This change from being the energy of space to kinetic energy of particles arises very naturally when particles are treated as the quantum fields that they are. In some scenarios inflation only ends in some regions of the universe and parts of the universe continue to inflate forever.

Consider a spacetime with some fluctuations superposed on a homogeneous space background– the background metric is

$$ds^2 = dt^2 - a^2(t)dx^2, \tag{2.126}$$

so this space is changing in time with scale factor a(t).

The matter in spacetime affects the space and space affects the matter via Einstein's equations. In the presence of matter with density rho and pressure p (fluid form), and vacuum energy lambda (cosmological constant), Einstein's equations for the scale factor become

$$\frac{\dot{a}^2}{a^2(t)} = H^2 = \frac{8\pi G\rho}{3} - \frac{k}{a^2(t)} + \frac{\Lambda}{3} \tag{2.127}$$

The properties of the matter enter here through the density ρ.

One way to get inflation, an accelerating scale factor a(t), can be seen with a toy model. Consider a very simple world where there is only the metric (with scale factor a(t)) above) and some matter represented by a scalar field Δ. Normally the field can have kinetic and potential energy. Take the potential energy of Delta, $V(\Delta)$, approximately constant. Since $V(\Delta)$ is a function of Δ, this doesn't have to be true for all values of Δ, say just for some values of Delta, and take the kinetic energy a lot smaller than the potential energy. Then the total energy rho will be

$$\rho = \text{kinetic energy} + V(\Delta) \sim V(\Delta) \sim K \tag{2.128}$$

where K is a constant by assumption. Using this expression for the energy density in the equation for the metric, from above,

$$H^2 = \frac{8\pi GK}{3} - \frac{k}{a^2} + \frac{\Lambda}{3} \tag{2.129}$$

and as a(t) increases, we eventually get

$$\frac{\dot{a}^2}{a^2} \sim C \tag{2.130}$$

where

$$C = \frac{8\pi GK}{3} + \frac{\Lambda}{3}, \tag{2.131}$$

a time independent constant. Thus this equation can be solved, to get

$$a(t) = e^{C\frac{1}{2}t} \tag{2.132}$$

That is, exponential expansion.

In field theory, you specify the equations of motions for the field, and can get the example of potential energy V » kinetic energy in a few ways. The kinetic energy is related to the change in the potential with the field, so in the simple toy models often used for examples, you can be at an extremum of the potential or just have the potential change very slowly with Δ ("slow roll").

So if there is just one field Δ dominating, plus gravity, inflation can occur if $dV(\Delta)/d\Delta$ is "small" for whatever value(s) of Δ describes the universe at that time. There is a quantitative description of how small "small" must be for a given theory.

Chapter 3

Practice

3.1 Introduction

In cosmology cosmic microwave background (CMB) radiation is regarded as a form of electromagnetic radiation filling the universe. While no radiation from the background space is observed visibly by use of a traditional optical telescope, a faint background glow can be observed by use of a radio telescope. It is observed to be almost exactly the same in all directions, and is not associated with any star, galaxy, or other object. This glow is strongest in the microwave region of the radio spectrum, hence the name cosmic microwave background radiation. The CMB's discovery in 1964 by radio astronomers Arno Penzias and Robert Wilson was the culmination of work initiated in the 1940s, and in 1978 they received the Nobel Prize for this discovery.

The CMB radtiation is well explained by the Big Bang model explaining what may have happened at the very beginning of our universe. Extrapolation of the expansion of the universe backwards in time using general relativity yields an infinite density and temperature at a finite time in the past.This singularity signals the breakdown of general relativity. Discoveries in astronomy and physics have shown beyond a reasonable doubt that our universe did in fact have a beginning.

Precise measurements of cosmic background radiation are critical to cosmology, since any proposed model of the universe must explain this radiation. The CMB radiation has a thermal black body spectrum at a temperature of 2.725 K, thus the spectrum peaks in the microwave range frequency of 160.2 GHz, corresponding to a 1.9 mm wavelength. The glow is almost but not quite uniform in all directions, and shows a very specific pattern equal to that expected if the inherent randomness of a red-hot gas is blown up to the size of the universe. In particular, the spatial power spectrum (how much difference is observed versus how far apart the regions are on the sky) contains small anisotropies, or irregularities, which vary with the size of

the region examined. They have been measured in detail, and match what would be expected if small thermal fluctuations had expanded to the size of the observable space we can detect today.

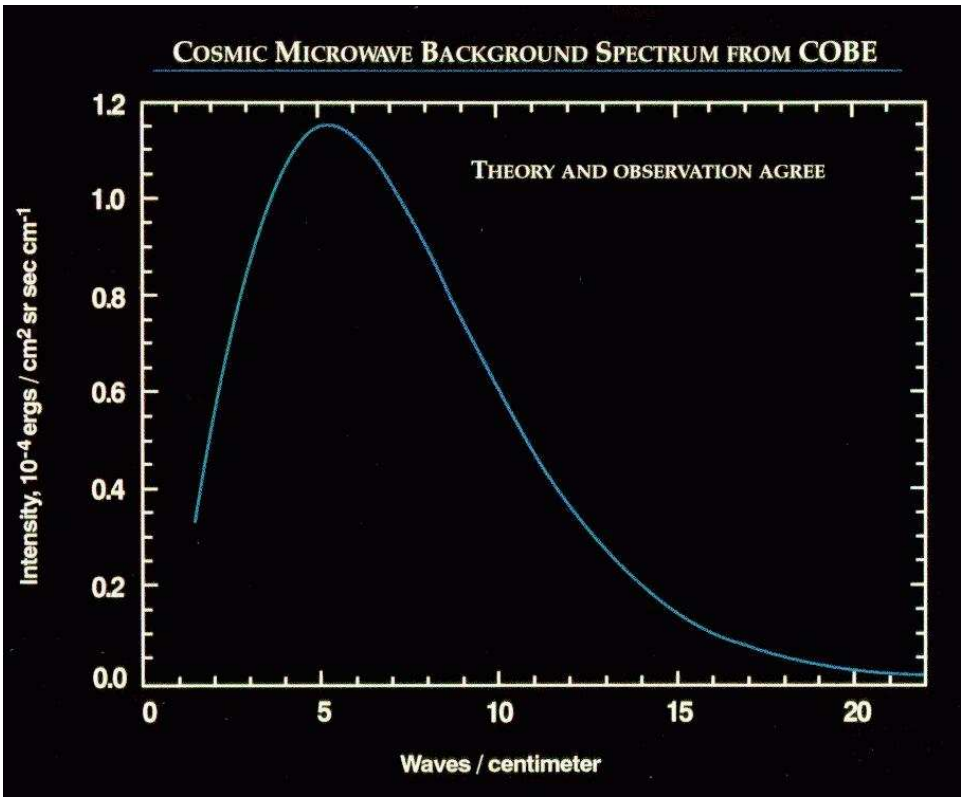

Figure 3.1: The CMB black body spectrum as measured by the COBE FIRAS instrument. (From NASA/COBE team)

The cosmic microwave background is isotropic to roughly one part in 100,000: the root mean square variations are only 18 μK. The Far-Infrared Absolute Spectrophotometer (FIRAS) instrument on the COBEsatellite has measured the spectrum of the cosmic microwave background. The CMB was compared with an internal reference black body and the spectra agreed to within the experimental error. It was concluded that any deviations from the black body form that might still remain undetected in the CMB spectrum over the wavelength range from 0.5 to 5 mm must have a weighted root mean square value of at most 50 parts per million (0.005%) of the CMB peak brightness. This made the CMB spectrum the most precisely measured black body spectrum in nature.

The cosmic microwave background, and its level of isotropy, are both predictions of Big Bang model. In the theory, after about 10^{-37} seconds the nascent universe underwent exponential growth that smoothed out nearly

all inhomogeneities a process known as cosmic inflation. This was followed by symmetry breaking; a type of phase transition that set the fundamental forces and elementary particles in their present form. After 10^{-6} seconds, the early universe was made up of a hot plasma of photons, electrons and baryons. The photons were constantly interacting with the plasma through Thomson scattering. As the universe expanded, adiabatic cooling caused the plasma to cool until it became favourable for electrons to combine with protons and form hydrogen atoms, thus making the universe transparent to radiation. This recombination event happened at around 3,000 K or when the universe was approximately 379,000 years old. At this point, the photons scattered off the now electrically-neutral atoms and began to travel freely through space, resulting in the decoupling of matter and radiation. Since then, the temperature of the radiation has dropped by a factor of roughly 1100 due to the expansion of the Universe. As the universe expands, the CMB photons are red shifted, making the radiation's temperature inversely proportional to the Universe's scale length.

The color temperature of the photons has continued to diminish ever since; now down to 2.725 K, their temperature will continue to drop as the universe expands. According to the Big Bang model, the radiation from the sky we measure today comes from a spherical surface called the surface of last scattering. This represents the collection of points in space at which the decoupling event is believed to have occurred, less than 400,000 years after the Big Bang, and at a point in time such that the photons from that distance have just reached observers. The estimated age of the Universe is 13.7 billion years. However, because the Universe has continued expanding since that time, the comoving distance from the Earth to edge of the observable universe is now at least 46.5 billion light years.

The Big Bang theory suggests that the cosmic microwave background fills all of observable space, and that most of the radiation energy in the universe is in the cosmic microwave background, which makes up a fraction of roughly 6×10^{-5} of the total density of the universe. Two of the greatest successes of the big bang theory are its prediction of its almost perfect black body spectrum and its detailed prediction of the anisotropies in the cosmic microwave background. Although many different processes might produce the general form of a black body spectrum, no model other than the Big Bang has yet explained the fluctuations. The recent Wilkinson Microwave Anisotropy Probe has precisely measured these anisotropies over the whole sky down to angular scales of 0.2 degrees. These can be used to estimate the parameters of the standard ΛCDM model of the big bang. Some information, such as the shape of the Universe, can be obtained straightforwardly from the cosmic microwave background, while others, such as the Hubble constant, are not constrained and must be inferred from other measurements. The latter value gives the redshift of galaxies as a proportion of their distance.

The cosmic microwave background radiation and the cosmological red

shift are together regarded as the best available evidence for the Big Bang theory. The CMB gives a snapshot of the Universe when, according to standard cosmology, the temperature dropped enough to allow electrons and protons to form hydrogen atoms, thus making the universe transparent to radiation. When it originated some 380,000 years after the Big Bang [1] the temperature of the Universe was about 3,000 K. This corresponds to an energy of about 0.25 eV, which is much less than the 13.6 eV ionization energy of hydrogen.

3.2 Wilkinson Microwave Anisotropy Probe

The Wilkinson Microwave Anisotropy Probe or WMAP is a satelite launched by NASA in June 2001. Its mission is to map out the entire sky in five different bands (mean frequencies): the K band (23GHz), Ka band (33GHz), Q band (41GHz), V band (61GHz) and W band (94GHz).

3.2.1 The Probe

The WMAP[2] satellite was originally conceived to replace and complement the measures taken by other experiments up to then. These include the COBE satellite, the MAXIMA and BOOMERanG balloon experiments, as well as several ground based experiments. The probe was proposed in June 1995 and construction started in June 1996. It was launched by a Med-Lite Delta II 7425-10 rocket on June 30, 2001 at 15:46:46 EDT.

The probe itself uses two back–to–back primary mirrors that can be made out on the picture in figure 3.2.1. It is shielded from the sun by the large golden heat shield doubling as a solar panel for power. Above the solar panels, in what's referred to as the "hex hub", the 419W power supply, electronics and control instruments are housed. A so called gamma alumina cylinder shields the instruments from the hex hub. The instruments are also passively cooled by radiators on each side[3] [25]. This passive cooling feature was essential to the possibility of extending the mission beyond the original intent.

In order to gather as much information as possible the WMAP satellite is required to be as far away from any heavenly bodies as possible, even more

[1] This time period is generally known as the "time of last scattering" or the period of recombination or the decoupling era.

[2] WMAP was named MAP until February 2003 when it was renamed in honor of the late MAP team member David Todd Wilkinson (1935-2002).

[3] In contrast from WMAP, the Planck satellite will contain bolometric instruments that require cooling to 0.1K to work; achieved by dissolving ^{3}He into ^{4}He. This mixture is then vented into space after having performed its cooling duty. The finite supply of Helium limits its lifetime to about two years because even if the radiometric low frequency instruments in theory could operate longer, the cost of recording data and the marginal improvement over the WMAP data means it will most likely be shut down.

(a) WMAP takeoff (from nasa.gov)

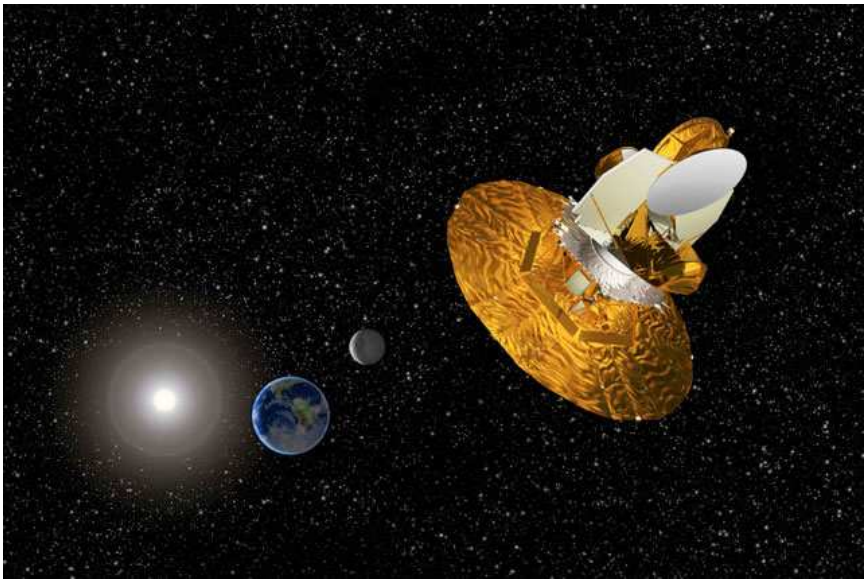

(b) WMAP underway (NASA/WMAP team)

Figure 3.2: The Delta II rocket carrying WMAP taking off from Cape Canaveral (top) and artist rendering of WMAP underway to its intended location in L2 (bottom).

so than high frequency observatories because even very cold objects radiate and reflect in the 23-94MHz range. Simultaneously it needs to be at a point where data can be transmitted down to Earth. The Lagrange points, shown in figure 3.3, enable the craft to remain at a great distance from the Earth and Moon, while keeping still relative to the Earth in its orbit around the Sun. Points L1, L2 and L3 are unstable because they are saddle points so that any object placed there will be moved down into the potential. Points L4 and L5 are stable, because any object starting to drift away from the point will experience a Coriolis force to force it into an orbit around the point. This is a disadvantage for placement of satellites because they require areas of space relatively free of dust and objects that may hit it and damage them; ruling out L4 and L5. L3 is impractical because the Sun blocks signals from the probe, and L1 is between the Sun and the Earth, making it difficult to avoid interference from both at the same time when scanning the sky. The WMAP satellite was therefore placed in L2.

The probe reached its intended destination, L2, on August 10th 2001 and the team released the first year data in February 2003 [9]. Although originally

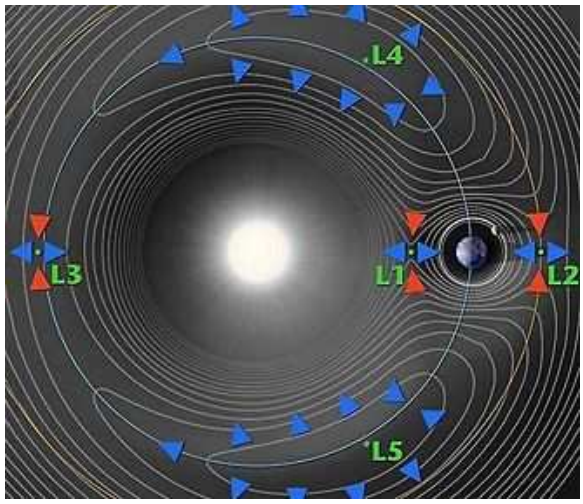

Figure 3.3: Overview of the five Lagrange points in the system consisting of the Earth, Moon and Sun. They are the points at which an orbiting body will maintain the same position relative to the Earth in a rotating frame of reference in their orbit around the Sun. The figure shows a contour plot of the gravity potentials in the system, and the arrows show the tendency of objects placed in the points to wander if they are close to, but not perfectly on each of the points. (from NASA/WMAP team)

only intended for 27 months of operations, the probe proved to last longer than intended and in March 2006 the three year data was released [26]. The five year data was released in March of 2008 [27]. When it was decided to

extend the mission; priority shifted from temperature maps to polarization maps (so called "stretch" goals), but the polarization maps obtained are still too lacking in detail for meaningful ellipticity measurement statistics to be obtained.

3.2.2 The Instruments

Band	f_{center} (GHz)	Δf_{noise} (GHz)	T_{HEMT} (K)	$N_{assembly}$	$\Theta FWHM$ (deg)
K	23	5.5	25	1	0.88^o
Ka	33	7.0	35	1	0.66^o
Q	41	8.3	50	2	0.51^o
V	61	14.0	80	2	0.35^o
W	94	20.5	100	4	0.22^o

Table 3.1: Specifications for each of the different WMAP bands. This table shows the peak frequency of detection (f_{center}), the uncertainty in measure, or noise, per assembly (Δf_{noise}), the hot amp temperature (T_{HEMT}), the number of assemblies ($N_{assembly}$) and the spherical approximation to the beam ($\Theta FWHM$). The number of radiometers and channels per assembly are two and four respectively.

The CMB is most easily observed in the bands from 40 to 130 GHz, as shown by figure 3.4. Above, the CMB is increasingly drowned by dust foregrounds, below, free–free and synchrotron radiation foregrounds will increasingly drown the signal [28, 29]. All instruments on the probe share the same mirrors. The two 1.4×1.6m primary mirrors mounted back–to–back on "top" of the satellite (see image 3.2.1) reflect into the 0.9×1.0m secondary mirrors which again reflect into the radiometer feed horns. These are mounted on a rack back–to–back and each pair of radiometers feed four channels down through amplification by one cold (see table 3.1) and one hot (290K) amplifier to detection. The setup is described in figure 3.5 where A and B denote the two sides of the original signal input. The signal input (A and B) from the feed horns is split in the orthomode transducer (OMT) into orthogonal polarization modes (A_V and A_H and B_V and B_H) and combined in a hybrid Tee so that

$$\text{Signal}_{V1} = \frac{A_V + B_V}{\sqrt{2}} \tag{3.1}$$

and

$$\text{Signal}_{V2} = \frac{A_V - B_V}{\sqrt{2}} \tag{3.2}$$

for one radiometer and

$$\text{Signal}_{H1} = \frac{A_H + B_H}{\sqrt{2}} \tag{3.3}$$

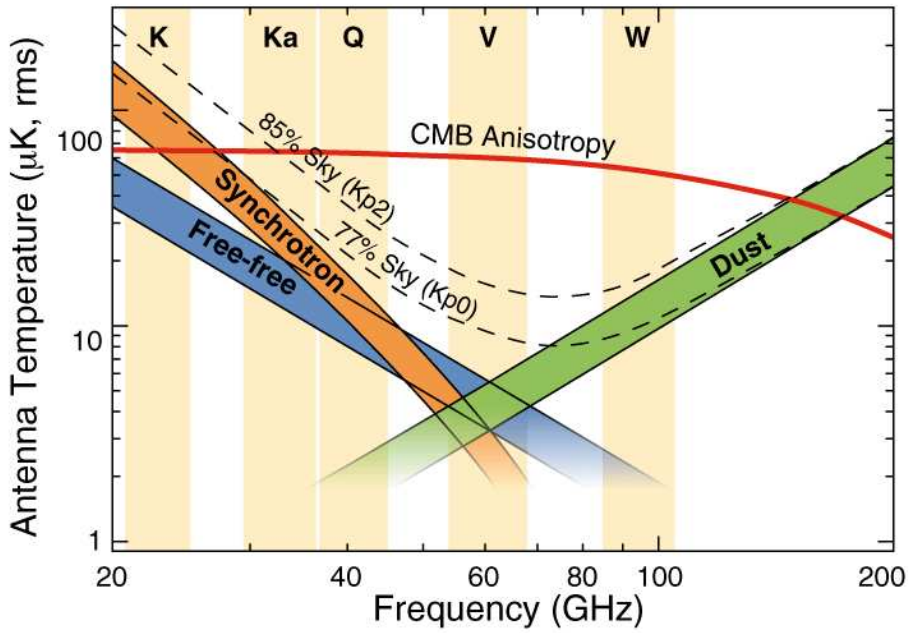

Figure 3.4: Logarithmic plot showing the WMAP bands and the expected noise in each. The CMB is masked by galactic foreground radiation stemming from galactic dust in the high frequency area and synchrotron and free–free scattering emmision in the lower frequency area. (from NASA/WMAP team)

and

$$\text{Signal}_{H2} = \frac{A_H - B_H}{\sqrt{2}} \tag{3.4}$$

for the other. All channels then amplify the signal and from each pair, one of the signals is phase shifted between 0 and π and the signal is split back into A_V and B_V and A_H and B_H again in a second hybrid Tee. The beam is then detected by a square–law demodulator[4] returning the difference

$$S_V = B_V - A_V \tag{3.5}$$

. and

$$S_H = B_H - A_H \tag{3.6}$$

As shown by figure 3.5 there are two detectors per radiometer and the returned digital signal is the average between these two. The two radiometers per assembly may be combined to measure temperature alone, or subtracted to measure polarization. What is in the end actually measured is

[4]Analogue demodulator whose output voltage is proportional to the square of the input voltage.

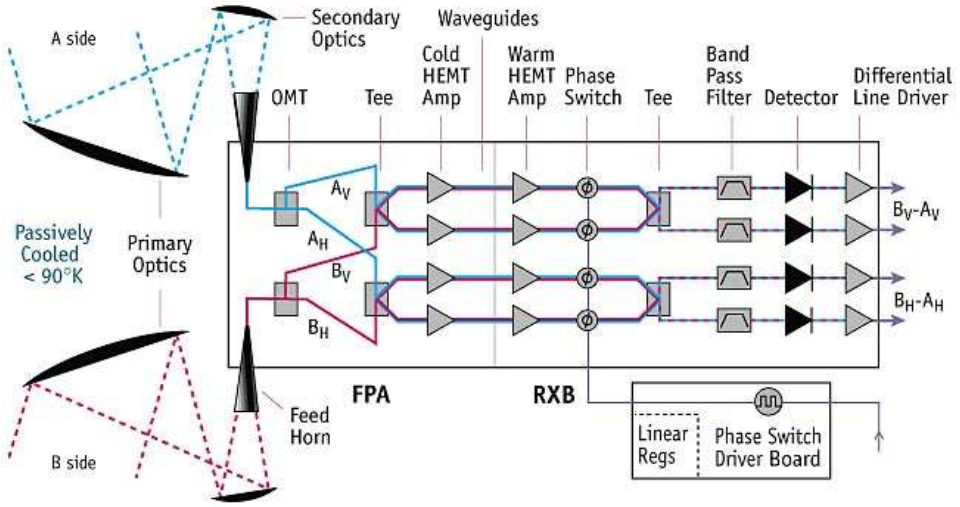

Figure 3.5: WMAP differing assembly. From the intake horns the signal is directed down four channels to be amplified twice (cold and hot amps). Each two channels have two detectors. The WMAP convension is to refer to a pair of these channels as a "radiometer" and all four together as a "differing assembly". (from NASA/WMAP team)

thus the temperature *difference* between photons collected with $\approx 140°$ between them. The data is calibrated using the known dipole from Doppler shift by motion relative to the primordial gas (shown in figure 1.1) [30].

The probe carries such detectors in five different frequency bands centered on 23, 33, 41, 61 and 94GHz (see table 3.1). All detectors are radiometers and consist of one or more (again described in table 3.1) assemblies described in figure 3.5. Effective bandwidth is 13GHz in all bands [31]. The low frequency bands (K and Ka) are included primarily to map (and remove) the low frequency foregrounds, while radiometer technology limit the highest detectable frequencies to about 100GHz, leaving us less information on high frequency foregrounds[5].

The dominating foregrounds in the K and Ka bands make them unsuited for ellipticity measures, because the CMB dominated area covers only a very small patch on each pole in both maps. Disturbance from the effect of free–free and synchrotron radiation diminish in frequencies above the Ka band. None of the bands go high enough for dust emission to dominate except in the galactic band, so that the Q, V and W bands are all suited for ellipticity measure.

[5]The Planck satellite will be equipped with bolometric instruments that, in addition to having much better angular resolution, can be made to go to higher frequencies. This will give much better data on high frequency foregrounds.

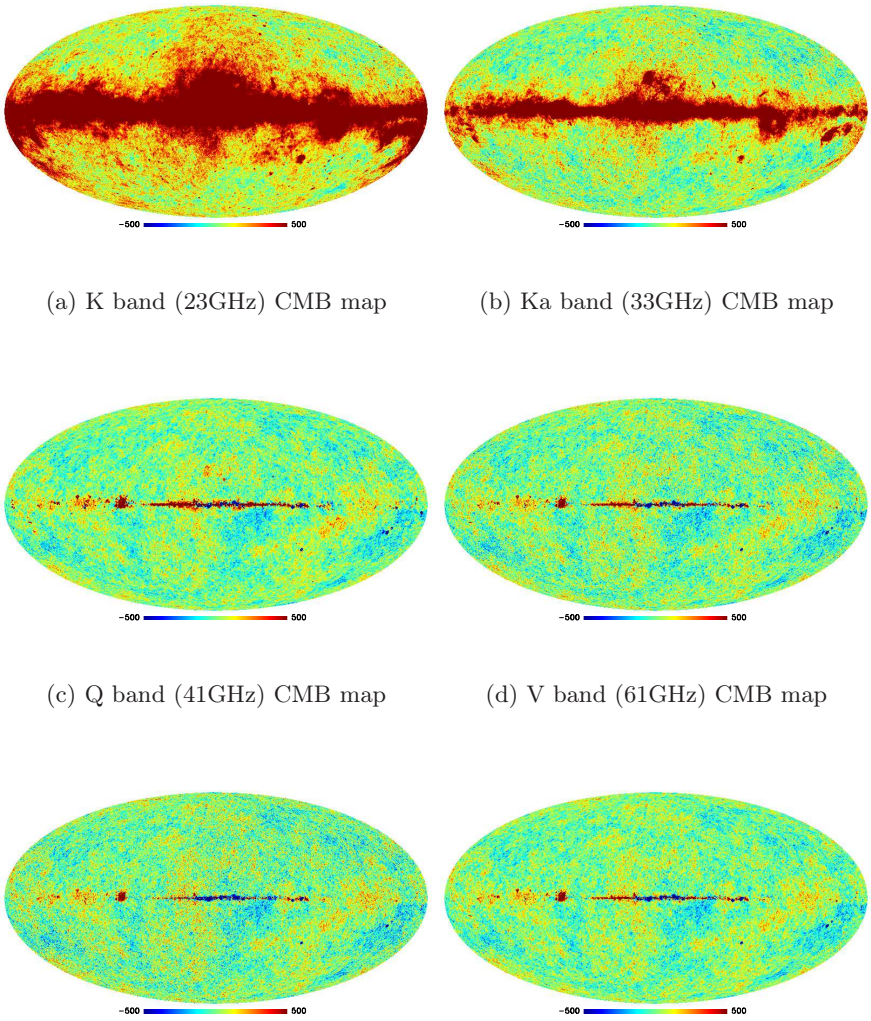

(a) K band (23GHz) CMB map

(b) Ka band (33GHz) CMB map

(c) Q band (41GHz) CMB map

(d) V band (61GHz) CMB map

(e) W band (94GHz) CMB map

(f) Combined VW bands CMB map

Figure 3.6: Temperature maps in all five bands as well as the combined vw map. The galactic disc can be easily seen as a horizontal band across all maps, but least in the two "best" bands, V and W. The Ka band and especially K band are too contaminated by foregrounds to be of use for ellipticity measurements, but are useful for deciding the shape of masks. All maps have been plotted in temperature ranges of -500 to 500μK where the monopole and dipole have been subtracted and the zero point represents the average temperature of the CMB.

3.3 Spherical Harmonics

There are several ways of using a HEALPix map (see section 3.5) of the CMB and one of them is to split it up into different scales. The basic wave functions for *spherical harmonics* is found by solving Laplace's equation:

$$\nabla^2\psi = 0 \tag{3.7}$$

where ψ is a function. To solve this in spherical coordinates, it is necessary to split it into

$$\psi(r,\theta,\phi) = R(r)\Theta(\theta)\Phi(\phi). \tag{3.8}$$

Because this is a 2 dimensional function on a sphere; R is constant equal to one, and the equation then becomes

$$\frac{\Phi(\phi)}{\sin(\theta)}\frac{d}{d\theta}\left(\sin\theta\frac{d\Theta(\theta)}{d\theta}\right) + \frac{\Theta(\theta)}{\sin^2(\theta)}\frac{d^2\Phi(\phi)}{d\phi^2} + l(l+1)\Theta(\theta)\Phi(\phi) = 0. \tag{3.9}$$

Solving this equation results in

$$\psi = \sqrt{\frac{(2l+1)(l-m)!}{4\pi(l+m)!}}P_{lm}(\cos(\theta))e^{im\phi} \equiv Y_{lm}(\theta,\phi) \tag{3.10}$$

where $l \geq 0$ are the number of modes for different scales and $-l \leq m \leq l$ is the "shape" of the waves, that is, the number of waves along equator. When $m = 0$, l says how many waves can be fitted between 0 and 2π. The wavelength of each mode is therefore

$$\lambda = \frac{2\pi}{l}. \tag{3.11}$$

More generally for $m \neq 0$, the "typical size" for a spot in a map of this kind, is

$$\lambda \approx \frac{\pi}{l}. \tag{3.12}$$

These Y_{lm}s are the spherical harmonic functions. It should be noted that they have a useful symmetry:

$$Y^*_{lm} = (-1)^m Y_{l-m}. \tag{3.13}$$

All functions defined on a sphere may be expanded into spherical harmonics so that

$$T(\theta,\phi) = \sum_{l=0}^{l_{max}}\sum_{m=-l}^{l} a_{lm}Y_{lm}(\theta,\phi) \tag{3.14}$$

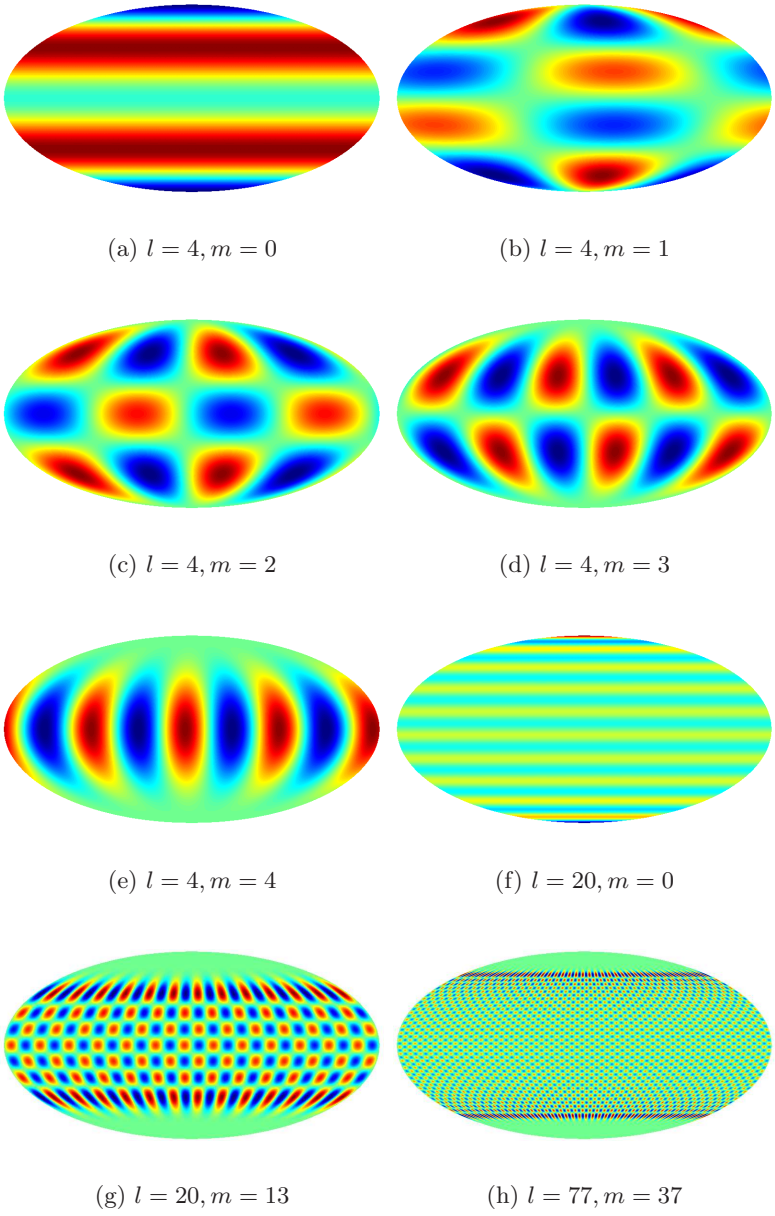

(a) $l = 4, m = 0$ (b) $l = 4, m = 1$

(c) $l = 4, m = 2$ (d) $l = 4, m = 3$

(e) $l = 4, m = 4$ (f) $l = 20, m = 0$

(g) $l = 20, m = 13$ (h) $l = 77, m = 37$

Figure 3.7: The modes for $l = 4$ (from top to bottom with $m = 0, 1, 2, 3, 4$) as well as a few other examples. All l may be subdivided into m's, but because all values on the function are real, there is no need for the negative m's.

where the expansion coefficients, a_{lm} are given as

$$a_{lm} = \int_{4\pi} T(\theta,\phi) Y^*_{lm}(\theta,\phi) d\Omega \tag{3.15}$$

where $Y^*_{lm}(\theta,\phi)$ is the complex conjugate of the function $Y_{lm}(\theta,\phi)$.

If one assumes the universe is truly isotropic and Gaussian then no information is contained in the different m's as m's only give directions on the sky for a particular scale l. It is then possible to define an *angular power spectrum* to be

$$C_l \equiv \frac{1}{2l+1} \sum_{m=-l}^{l} |a_{lm}|^2 \tag{3.16}$$

is an average over all m's for each l. This only makes sense if there are no inhomogeneities and if all fluctuations are truly Gaussian which will be the case if all perturbations originated as quantum mechanical harmonic oscillators as inflation (section 2.4) opens for. Still assuming perfect Gaussianity, the statistical distribution for the a_{lm}s is

$$P(a_{lm}) \propto \frac{1}{\sqrt{C_l}} e^{-\frac{a^*_{lm} a_{lm}}{2C_l}} \tag{3.17}$$

and the power spectrum is the variance of the a_{lm}s.

The equations (3.15) and (3.17) both contains the complex conjugate of Y_{lm} and a_{lm} respectively. Because the CMB maps only contain real entries, the computation may be simplified by using that

$$T^*(\theta,\phi) = T(\theta,\phi) \tag{3.18}$$

so that

$$\sum_{lm} a_{lm} Y_{lm}(\theta,\phi) = \sum_{lm} a^*_{lm} Y^*_{lm}(\theta,\phi). \tag{3.19}$$

Because of (3.13)

$$\sum_{lm} a_{lm} Y_{lm}(\theta,\phi) = \sum_{lm} a^*_{lm} (-1)^m Y_{l-m}(\theta,\phi), \tag{3.20}$$

but this means that

$$\sum_{lm} a_{lm} Y_{lm}(\theta,\phi) = \sum_{lm} a_{l-m} (-1)^m Y_{lm}(\theta,\phi), \tag{3.21}$$

which shows that it is true for a_{lm}'s that

$$a^*_{lm} = (-1)^m a_{l-m} \tag{3.22}$$

just as for the Y_{lm}'s.

3.3.1 Theoretical and Observed Power Spectrum

When the C_ls are measured, the observed values are not necessarily the perfect truth. This is because the observed values for the power spectrum is just one realization of what theory might predict — assuming one had perfect knowledge of all physics on beforehand, it would be possible to calculate a power spectrum of how the universe would appear for a given observer at a time (say here, today), but the theoretical power spectrum is in fact just the most likely outcome among a number of less likely ones. One may turn this around to realize that while the observed power spectrum

$$\hat{C}_l = \frac{1}{2l+1} \sum_{m=-l}^{l} |a_{lm}|^2 \tag{3.23}$$

is only one of many different possible outcomes; all physical effects are described by the *ensemble mean* power spectrum:

$$C_l = \left\langle \frac{1}{2l+1} \sum_{m=-l}^{l} |a_{lm}|^2 \right\rangle_{ensemble} . \tag{3.24}$$

Unfortunately cosmologists only have one experiment! There is no way one may obtain a different one[6], and so there will always be an uncertainty in the "true"(ensemble mean) power spectrum. This uncertainty is termed the *cosmic variance* and may be shown to be

$$\Delta C_l = \sqrt{\frac{2}{2l+1}} C_l \tag{3.25}$$

The best one may do with the obtained data is to estimate the likelihood that a given physical model is the correct one given the $\hat{C}_l$s observed, assuming still that they contain all relevant information.

If one assumes that the universe is of a kind where all information indeed is contained in the angular power spectrum, there would be no specific ellipticity to be found. Thus, if ellipticity were found to be inconsistent with simulated maps generated from the measured CMB power spectrum, it would indicate that the power spectrum is not the whole story[7]. Conversely, if no difference is found, it can still not be ruled out that the universe is not isotropic and/or that the fluctuations are not all Gaussian.

[6] Moving to another time or place in the universe would do the trick, but only if the difference is of cosmological significance. Creating a new universe would also, obviously, do the trick. The most realistic proposal to gain information of the universe would seem to get observations of the cosmic neutrino background, predicted to be there, but never observed, but this, also, seems exceedingly hard.

[7] Or that one of the HEALPix routines create_alm or alm2map contains errors...

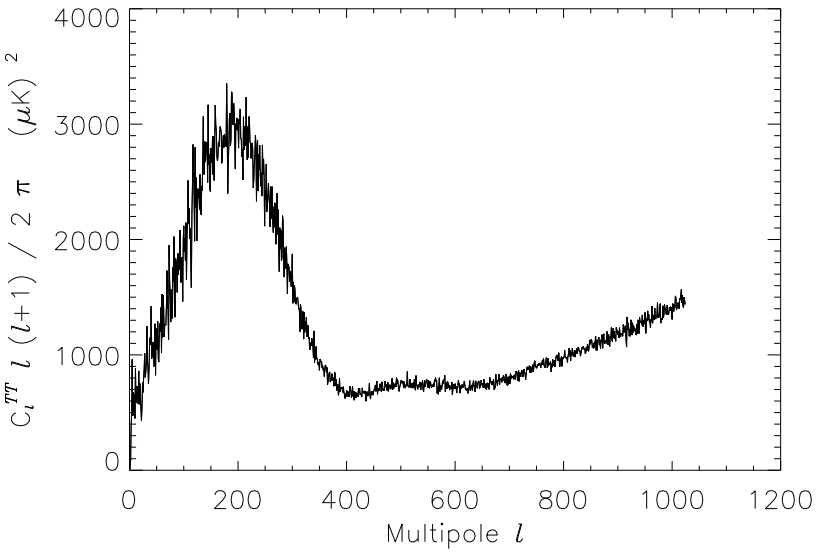

Figure 3.8: The observed angular power spectrum. This particular one is from the raw data for the WMAP 5 year combined vw map with l running up to 1024. The first and second peak has been suppressed by the beam. The third and fourth peaks, predicted to be there, have been completely drowned by noise, which starts to dominate on smaller scales (higher l), but may be observed when noise is corrected for.

3.4 Dogs in the Manger

In a perfect world this would be the end of the story. However, the resolution and accuracy of the measurements is limited by two observational constraints in addition to the constraint of finite pixelization. The observational limit is placed from the effects of *beam* and *noise*. Beam limits the resolution of the picture and noise limits the accuracy of measurements. Noise can be corrected for by increasing the scanning time; beam places and absolute limit on the angular resolution. The angular resolution in turn determines how fine the pixel resolution (N_{side}) must be to avoid loss of information in the picture.

3.4.1 Beam

The scanning profiles of radiometers cannot be made infinitely narrow. Rather; the received photons originate within a loose "cone" with the detector at its tip with photons originating from close to the instrument axis of orientation having a greater probability of being detected than photons from further away. This cone is referred to as a beam and the probability distribution

for photon detection is a *beam profile*. This effect puts a natural limit on the resolution of CMB data, and must be accounted for when CMB maps are made from the raw data. The effect of the beam is to turn the *measured* temperature at a given point in the sky, $T_{(\text{measured})}(\theta, \phi)$, into a function of the true temperature on that particular point, $T_{(\text{true})}(\theta, \phi)$, and a *beam function* $b(\theta, \phi)$ representing the beam smear taking into account that the measured temperature is also dependent upon neighbouring points on the sphere. This gives that for each point on the sphere

$$T_{(\text{measured})}(\theta, \phi) = \int_{4\pi} T_{(\text{true})}(\theta', \phi') b\left(|(\theta, \phi)| - |(\theta', \phi')|\right) d\Omega. \qquad (3.26)$$

Beam profiles will be approximated by Gaussian functions with full–width–half–maximum (FWHM) values as given in table 3.1. If one approximates the

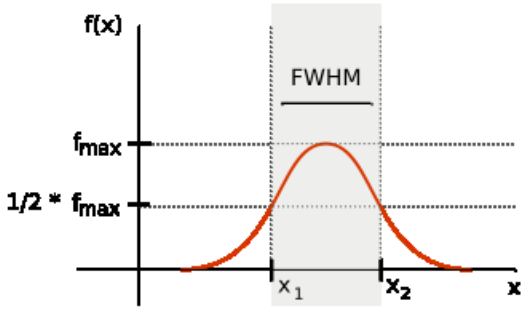

Figure 3.9: FWHM is the width of the full function at half its maximum value.

beam function to a Gaussian wavelet centered on (θ, ϕ), it follows from expression (3.26) that the width (i.e. FWHM value) of function $b(\theta, \phi)$ decides how dependent $T_{(\text{measured})}(\theta, \phi)$ is on the true temperature on a neighbouring point $T_{(\text{true})}(\theta + \Delta\theta, \phi + \Delta\phi)$ and likewise how dependent the temperature measured in the point $(\theta + \Delta\theta, \phi + \Delta\phi)$ is on $T_{(\text{true})}(\theta, \phi)$. A broad beam makes $T_{(\text{measured})}(\theta, \phi)$ more dependent upon $T_{(\text{true})}(\theta + \Delta\theta, \phi + \Delta\phi)$ and vice–versa and the angular resolution is decreased. Obviously, it is always desirable to reduce the beam smear as much as possible.

Although it is common to approximate the beam function $b(\theta, \phi)$ as a Gaussian distribution centered on the axis of orientation, the true beam is distorted [32, 33, 34]. This is an artifact of the non spherical mirrors, the side lobes, the mirror and feed horn backing structure etc. The true form of the beam is measured by observations of Jupiter and the results are shown in figure 3.10. The Gaussian approximation is justified by the WMAP scanning pattern, whereby each point in the sky is scanned in as many orientations as possible.

On real data, the effect is inherent in the data, and only needs to be considered whenever conversion to and from spherical harmonics are needed

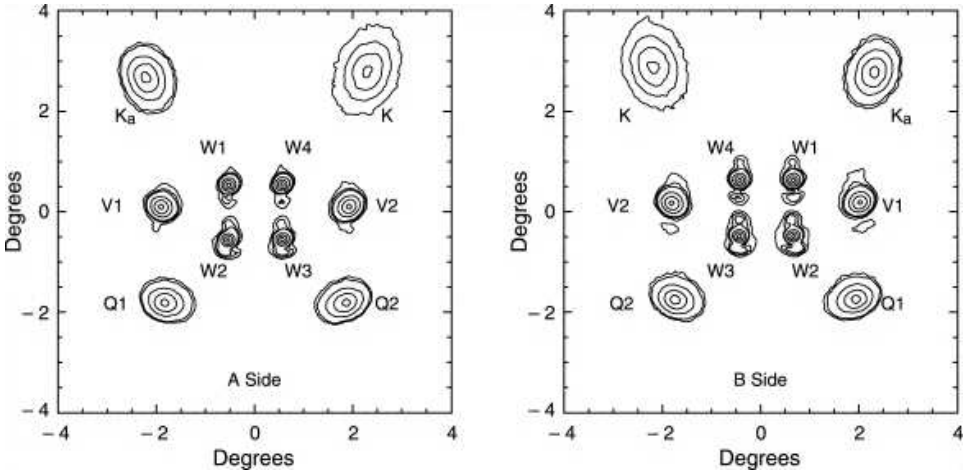

Figure 3.10: True measured beam profiles for the WMAP radiometer assemblies. The placement of the contour plots suggest the placement of the radiomoeter feed horns on the rack. If the beams were truely Gaussian, these plots would all be symmetric and the contour lines would suggest a bell shape.(from [32])

(see section 3.3). If a map is to be simulated, the effect of including beam for a given l is to change the returned a_{lm}'s into

$$a_{lm(\text{beam})} = a_{lm} \cdot e^{\frac{-\sigma^2 l(l+1)}{2}} \tag{3.27}$$

so that the power spectrum turn into

$$C_{l(\text{beam})} = C_l \cdot e^{-\sigma^2 l(l+1)} \tag{3.28}$$

where

$$\sigma^2 = \frac{\lambda^2}{8 \ln 2} \tag{3.29}$$

for a beam with FWHM = λ. It is preferable to go to harmonic space for inclusion of the beam as this is computationally more efficient.

3.4.2 Noise

Taking beam into account is unfortunately not the only story. Noise is the effect that the analogue output from a radiometer channel is not necessarily directly proportional to the input signal — rather there is a distribution of values that will be returned by the analogue radiometer for a given input. The effect of noise is to turn the output signal $T_{(\text{output})}(\theta, \phi)$ into

$$T_{(\text{output})}(\theta, \phi, t) = T_{(\text{measured})}(\theta, \phi, t) + n(t) \tag{3.30}$$

where n is a random number stemming from noise that cannot be known. Cosmological parameters may be assumed to be independent of t, so that only n is not constant with time.

White noise is noise that is truly random (i.e. there is no influence from sources outside the radiometer, nor does it depend on any earlier noise) and whose expectation value $\langle n \rangle$ is zero. Obviously this would place the expectation value for the signal as a whole on the desired signal. The uncertainty in the signal is then determined by the shape of the noise distribution. There are several forms of white noise. *Shot noise* is noise stemming from the fact that both the electromagnetic radiation entering the detector and the electric current inside it is carried in discrete quantum packages. This noise follows a Poisson distribution with standard deviation

$$\sigma_s = \sqrt{2eI\Delta f} \tag{3.31}$$

where e is the elementary charge, I is the mean current and Δf is the bandwidth[8]. Because the Poisson distribution approaches the Gaussian for large numbers, this noise is assumed to be Gaussian. *Johnson–Nyquist noise* or thermal noise is the noise associated with random quantum mechanical fluctuations of conducting particles. The squared noise voltage is (in either direction)

$$\langle V_t^2 \rangle = 4k_B T \Delta f R \tag{3.32}$$

where R is the resistance in the circuit, Δf is the bandwidth, T is the temperature in Kelvin and k_B is Boltzmann's constant. Obviously

$$\langle V_t \rangle = 0 \tag{3.33}$$

because thermal noise is not in any way determined by the external voltage, so there is no preferred direction on the thermal noise current. The root–mean–square (RMS) current standard deviation is found by dividing the RMS standard deviation of the voltage with R, so that the noise distribution of the signal has a standard deviation of

$$\sigma_t = \frac{\sqrt{\langle V_t^2 \rangle - \langle V_t \rangle^2}}{R} = 2\sqrt{\frac{k_B T \Delta f}{R}}, \tag{3.34}$$

or is, as with shot noise, proportional to the square root of the signal. The temperature dependence of the thermal noise is the reason for cooling the instruments down to below 100K. A third always–occurring white noise phenomenon, flicker (or $1/f$) noise, is ignored in the WMAP data because as it is proportional to the inverse frequency the effect is small compared to

[8] In other words it goes down compared to the signal for higher currents or if the bandwidth is increased

other noise sources given the high frequency electronics used. As the noise is considered Gaussian and proportional to the square of the signal, it follows that for N observations the noise is $\sqrt{N}$ and the *signal to noise ratio* (SNR) is

$$SNR = \frac{N}{\sqrt{N}} = \sqrt{N}. \tag{3.35}$$

This is true also if the N is the number of detectors, so that noise is decreased with the square root of the number of detectors for a particular frequency band (see table 3.1)

In the digital output the data is pixelated in the HEALPix scheme (see section 3.5). The effect of noise on a pixel i is then

$$T_{i(\text{output})} = T_i + n_i \tag{3.36}$$

where T_i is the signal average for that pixel and n_i is the mean uncertainty in the signal in that pixel due to noise. There should be no correlation between noise in different pixels, so that

$$\langle n(i)n(j)\rangle = \delta_{ij}\sigma_n^2 \tag{3.37}$$

where, if the total area of each pixel is A and the scanning density[9] per unit area is N,

$$\sigma_n = \sqrt{\frac{\sigma_t^2 + \sigma_s^2}{AN}} \tag{3.38}$$

is the total noise. This Gaussian distribution makes it simple to simulate noise in a map. The WMAP scanning pattern produces a non homogeneous σ_n and turns noise into a function of position. This noise map has been supplied by the WMAP team, and the one used for all analysis in this thesis is the combined optimized VW noise map, shown in image 3.11.

3.4.3 Nasty Dogs

In addition to these well understood internal sources of error, there are several other non–trivial and much less predictable sources. The data collected is influenced by several systematic sources of error. These include

- Sidelobe pickup of the Galaxy and solar system bodies
- Distorted beam shapes
- Effects induced by temperature instability

[9]The number of scans per unit area. This is proportional to the time spent scanning times the number of scanners used.

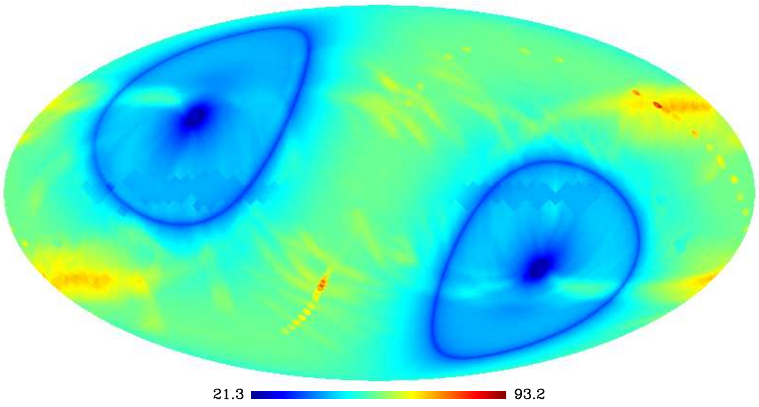

Figure 3.11: The noise map for the VW combined 5 year data. By generating a pseudorandom number with a Gaussian distribution with σ equal to the map value for each pixel, it is possible to simulate noise in a computer generated CMB map. This map has values assuming that temperatures are measured in μK.

- Residual non-white noise components
- Non-idealities in the radiometers
- Spacecraft pointing errors and nutation
- Calibration accuracy

It is important to know to what extent the different effects influence the final data made available to scientists. None of these have been considered in the work for this thesis, but they are nevertheless potential sources of error.

While it has been claimed that the WMAP team has underestimated the noise levels [35]; in all data analysis performed for this thesis it is assumed that all noise is white noise and that all beams are truly Gaussian.

3.5 HEALPix data

The WMAP input is in analogue form, prompting the need to organize the data into a usable, digital, form. Because the data is collected on a sphere, spherical polar coordinates (r, θ, ϕ) are used, it is assumed that r=1 for the entire map, that $0 \leq \theta \leq \pi$[10] and $0 \leq \phi < 2\pi$. In order to convert this data into digital form, it is necessary to somehow pixelate the sphere. The answer

[10] Whenever the term "north", "south" and "equator" is used, it will refer to $\theta = 0$, $\theta = \pi$ and $\theta = \pi/2$ respectively.

to this form is the HEALPix scheme, that is used on data from WMAP as well as on data from the upcoming Planck satellite [36].

HEALPix [37] is an acronym for Hierarchical Equal Area isoLatitude Pixelization, and is a way of dividing a sphere into pixels of equal size. The basic idea is very simple and based on the rhombic dodecahedron with each side being rounded off (or "inflated") to fit a sphere. "Inflating" a rhombic

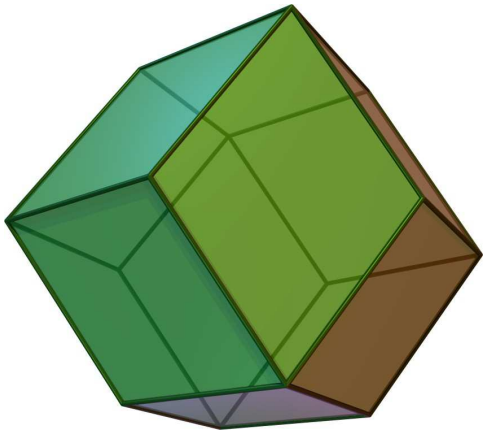

Figure 3.12: A rhombic dodecahedron. To form a HEALPix map of $N_{side} = 1$ the dodecahedron needs to be "inflated", and the $\theta = 0$ poles need to be placed in a vertex between four rhombi. (from Wikimedia Commons)

dodecahedron in such a way would morph the rhombi into quadrilaterals whose sides were not necessarily straight, but whose area would be equal for all. A spherical map thus pixelated have three qualities (all suggested in the name): pixels may be split to form maps of finer resolution, all pixels cover an equal amount of area and the center of all pixels are placed on discrete rings of equal latitude[11]. Each quadrilateral may then be subdivided along it's long edges into four smaller quadrilateral to form a map of increased resolution. Each of these new (smaller) pixels may again be divided in the same manner to form even smaller pixels. This division preserves the two important qualities that the size is the same for all pixels and that all pixels are placed on bands of constant latitude. Also; pixel boundaries are non-geodesic and take the forms

$$\cos\theta = a \pm (b \cdot \phi) \tag{3.39}$$

in the equatorial zone, and

$$\cos\theta = \frac{a+b}{\phi^2}, \tag{3.40}$$

[11]The "position" of a pixel refers to the center point unless otherwise specified.

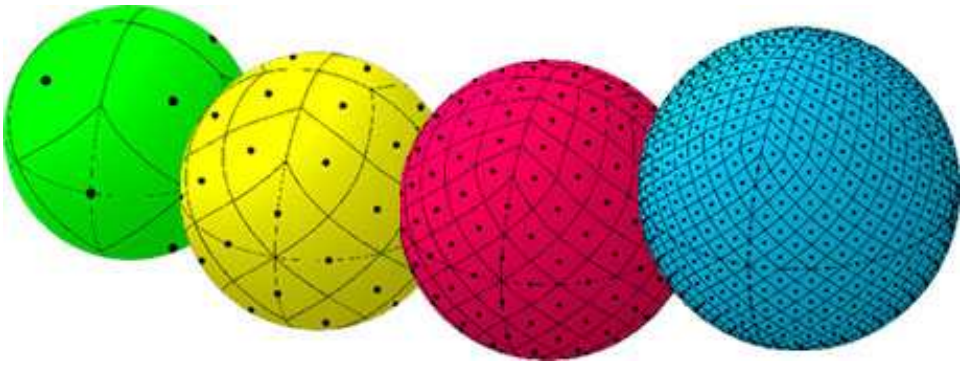

Figure 3.13: Illustration of the pixels size of the four coarsest map pixelizations. The four maps have N_{side} equal to 1, 2, 4 and 8 for the first, second third and fourth sphere from the left respectively. (from the JPL HEALPix site)

or

$$\cos\theta = \frac{a+b}{(\frac{\pi}{2}-\phi)^2}, \tag{3.41}$$

in the polar caps [37].

A useful measure of how finely the map is divided is the property N_{side} , the count of all pixels along one side of one of the original (largest possible) quadrilaterals. The original map has 12 such pixels and has an N_{side} of one. Dividing once creates a map of $N_{side} = 2$. Dividing again gives an $N_{side} = 4$ and so on, so that for a map divided n times the formula

$$N_{side} \equiv 2^n \tag{3.42}$$

is obtained. On a HEALPix map the total number of pixels is

$$N_{pix} = 12(N_{side})^2. \tag{3.43}$$

This means that as a rule of thumb, the average size of a HEALPix pixel is

$$\theta_{pix} = \sqrt{\frac{4\pi}{N_{pix}}} \approx \frac{60^o}{N_{side}}. \tag{3.44}$$

The number of islatitude rings for a map is

$$N_{rings} = 4N_{side} - 1. \tag{3.45}$$

For the WMAP data, the data is usually found pixelated with $N_{side} = 512$ or 1024 and in this thesis maps should be assumed to have $N_{side} = 512$ unless otherwise specified.

3.5.1 Ring or Nested

The data forming each map set is ordered as a one dimensional array whose index runs from 0 to $N_{pix} - 1$. It is necessary to know where on the sphere each pixel belongs so both the number of pixels and the order in which they should be placed must be known. Assuming N_{pix} is known, the map may be ordered into to listing schemes; ring and nested. The ring scheme follows the latitude rings, ordering the pixels whose θ value at the center point is closest to the $\theta = 0$ point in increasing ϕ order, then followed by the next closest θ center point values in increasing ϕ order and so on. The advantages of the ring scheme are to be able to easily implement the Fourier transforms from map to spherical harmonics (see section 3.3) as well as making it easy to distinguish hemispheres and to have an intuitive ordering of pixels even for large N_{pix} maps.

The nested scheme has the same starting point as the ring scheme in that the original twelve pixels are equally enumerated and subsequent divisions of the map are ordered into twelve tree structures (so that for $N_{side} = 1$ they are the same). To make higher N_{side} maps, consider two pixels numbered A and B in an $N_{side}/2$ map are split into pixels numbered A_0, A_1, A_2, A_3 and B_0, B_1, B_2, B_3 respectively. When the nested scheme is used, it is known that

$$A_i + 1 = A_{i+1} \tag{3.46}$$

and

$$B_i + 1 = B_{i+1} \tag{3.47}$$

for all i and that if $A < B$ then

$$A_i < B_j \tag{3.48}$$

for all i and j. The ordering of the different A_is with respect to each other is to assign the lowest number (A_0) to the southernmost pixel, the second lowest(A_1) to the easternmost pixel, third lowest (A_2) to the westernmost pixel and the highest number (a_3) to the northernmost of the four pixels. The "east–west" ordering is the same even if the pixels cross the boarder between $\phi = 2\pi$ (so that moving the $\phi = 0$ line will not alter their respective ordering[12]). The big advantage of the nested scheme is that the tree structure ordering of pixels facilitate easy finding of neighbours [38], in particular through the HEALPix method "neighbours_nest" (see section 3.7.1),and for this reason, this was the preferred scheme in work done for this thesis. Another advantage of the nested scheme is to make it easy to

[12] Assuming of course that they are not split into different $N_{side}/2$ pixels. Also it would probably alter the final enumeration, but not the respective order.

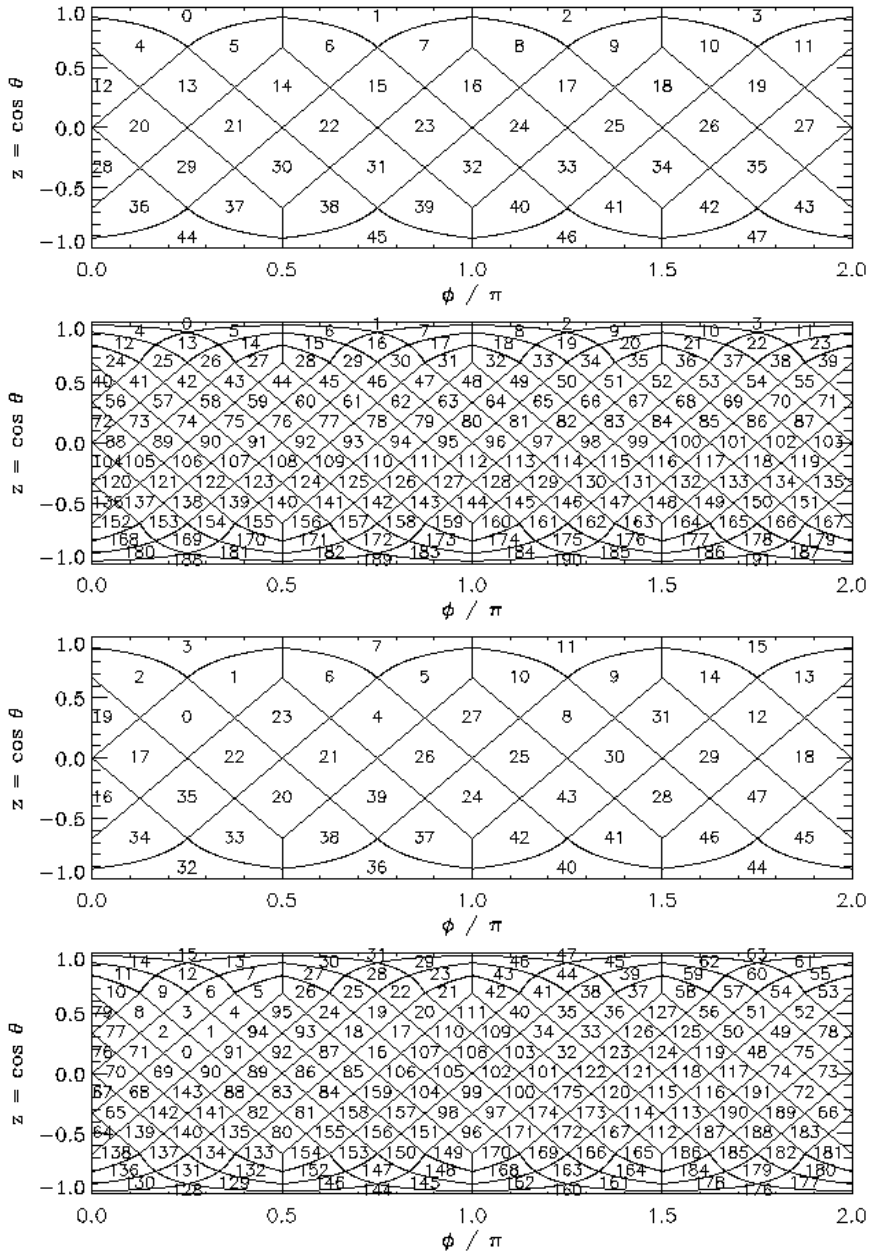

Figure 3.14: Cylindrical plot of the two enumeration schemes for N_{side} 2 and 4. The two uppermost plots show the ring scheme, the lower two the nested scheme. (from JPL HEALPix site)

increase or decrease the N_{side} ; halving the N_{side} means that for pixel n with value $T(n)$: wherever pixel $n|4$

$$n_{\rm new} = \frac{n}{4} \tag{3.49}$$

and

$$T(n_{\rm new}) = \frac{T(n) + T(n+1) + T(n+2) + T(n+3)}{4}, \tag{3.50}$$

and that doubling the N_{side} implies that

$$n_{\rm new} = 4n \tag{3.51}$$

and

$$T(n_{\rm new}) = T(n_{\rm new} + 1) = T(n_{\rm new} + 2) = T(n_{\rm new} + 3) = T(n). \tag{3.52}$$

This ease of changing N_{side} was exploited in step 1 of the "find_ellipticity" program described in section 4.2.1.

3.5.2 Yet More Dogs: Weight Function

A *weight function*, W is a function used for placing different importance on a different pars of a set of information. Averaging the value over a map (or parts of a map) with n pixels is done as

$$\langle M_p \rangle = \frac{1}{n} \sum_p M_p \tag{3.53}$$

and is equivalent to using the weight function $W_p = 1$ for all pixels. More generally

$$\langle M_p \rangle = \frac{\sum_p W_p M_p}{\sum_p W_p}. \tag{3.54}$$

In HEALPix the weight function is used as a safeguard against numerical instabilities resulting from the deformation of pixels near the poles compared to the equator. The actual weight function supplied by the program is precomputed for all N_{side} up to 8196 as a power spectrum.

There should be one beam function and one weight function for each of the radiometer maps [39]. This thesis used only one weight function, corresponding to the one supplied by HEALPix. The weight function used is an average over all functions used for the W band maps.

3.6 HEALPix Routines

The HEALPix package [37][13] contains a series of built in routines to more easily facilitate use of HEALPix data. They come for languages C, C++, Fortran90 (F90), IDL and Java, but for this thesis only F90 was used for programming and IDL for plots, so any description of methods will imply application to F90 and/or IDL and any differences to other languages will be assumed to be insignificant. Also, only the specific routines actually used directly will be mentioned although many routines called by the written program themselves call further routines.

3.6.1 Module "rngmod"

The rand_init routine will, if given zero to four seeds (integers) and a type planck_rng (containing four integers, a double and a logical) "handle" as input parameters, initialize a random sequence that may be used later by calls to the methods rand_gauss and rand_uni to get random numbers with a Gaussian or uniform distribution respectively.

The random number generator used is an exclusive–or (xor or $\oplus$)[14] bit shift generator — xorshift for short [40]. Such a random number generator takes a repeated xor shift of a number with a bit shifted version of itself and returns the results. To illustrate, consider the seed $a = 4019$ where the binary representation of a is (as a 32 bit integer)

$$a = 00000000000000000000111110110011 \tag{3.55}$$

and this number bit shifted three left is b so that $b = a \ll 3$ (where $\ll Q$ now is the bit shift left by Q operator) then b is

$$b = 00000000000000000111110110011000 \tag{3.56}$$

because the bit shift operator fills vacated bits with zeros. The xor operation then yields a third number c who is returned as the new pseudorandom number which is

$$\begin{array}{cl} & 00000000000000000000111110110011 \\ \oplus & 00000000000000000111110110011000 \\ = & 00000000000000000111001000101011 \end{array} \tag{3.57}$$

returning $c = 29227$. The random numbers actually returned by the subroutines are double precision floats x with $x \in [0, 1]$ created by dividing the resulting integer by 2^{32} and adding one if it is negative. Also, the random

[13] The site may be found at "http://healpix.jpl.nasa.gov/html/main.htm"

[14] The xor operation is the binary operation on two binary elements that is 0 if they are equal and 1 if they are not.

number generator included in the HEALPix package uses xorshift operations with bit shifts both left and right on the four last numbers to obtain a number to be returned.

This generator has a claimed theoretical best case period with four seeds of $2^{128} - 1 \approx 3,403 \times 10^{38}$, and such seeds (as found in [40]) are provided as default in the initialize routine. Such a high periodicity is obtained because the xor operation is taken four times in each instance and so that the resulting pseudorandom number depends on the four previous rather than just one. Because of the relatively low number of random numbers required this was considered not to be a problem for this thesis. What might be a problem is the claim by Francois Panneton and Pierre L'ecuyer that xorshift generators in general have poor equidistribution and/or fail several statistical tests even while their period is large and for this reason are not recommended unless speed is very important[41]. The HEALPix homepage specifically states that "we have not extensively tested this generator — it did not represent the main drive of this project". What problems might be associated with the xorshift implementation used in the HEALPix package are not known, and for this thesis it was assumed that the random number generator behaved flawlessly.

3.6.2 Subroutine "pixel_window"

The pixel_window subroutine will return the average–m space *window function* $w_{(\mathrm{pix})}(l)$ for a specified $\mathrm{N_{side}}$. This function contains the effects of pixelization on the observed $\hat{a}_{lm}$s compared to the true underlying a_{lm}s that would have been observed; so that

$$a_{lm} = \hat{a}_{lm} w_{(\mathrm{pix})}(l). \tag{3.58}$$

The function is derived by imagining that one has the true a_{lm}s so that the value f of the pixel p is

$$f(p) \equiv \sum_{l=0}^{l_{max}} \sum m a_{lm} w_{lm}(p) \tag{3.59}$$

where, if w_p is a function with value 0 outside p and 1/(area of p) inside p,

$$w_{lm} \equiv \int_{4\pi} w_p(\theta, \phi) Y_{lm}(\theta, \phi) d\Omega. \tag{3.60}$$

Because of computational constraints, this is simplified to

$$w_{lm}(p) = w_l(p) Y_{lm}(p) \tag{3.61}$$

which is a close approximation if the number of pixels is large. Here

$$w_l(p) = \sqrt{\frac{4\pi}{2l+1} \sum_{m=-l}^{l} |w_{lm}(p)|^2}. \tag{3.62}$$

Note the similarities between the power spectrum c_l vs a_{lm} and w_l vs w_{lm}; and indeed the observed power spectrum is related to the true (unpixelized) one by

$$\hat{C}_l = w_l^2 C_{l(\text{True theoretical})} \tag{3.63}$$

where

$$w_l^2 = \frac{1}{\mathrm{N_{pix}}} \sum_{p=0}^{\mathrm{N_{pix}}-1} w_l^2(p). \tag{3.64}$$

Even with the simplification made in (3.61), this is only possible to calculate exactly for $\mathrm{N_{side}}$ of 128 or less. The pixel window functions provided for greater $\mathrm{N_{side}}$ is a linear extrapolation of the one found for $\mathrm{N_{side}}$ 128.

3.6.3 Subroutine "create_alm"

This subroutine will, given a power spectrum c_l generate the a_{lm} coefficients (described in section 3.3) necessary to simulate a map. The a_{lm}s thus created will be based upon the assumption that the sky is Gaussian. If one inverts equation (3.16), then for the m'th coefficient for a given l;

$$|a_{lm}|^2 = C_l(2l+1) - \left(|a_{l0}|^2 + \ldots + |a_{lm-1}|^2 + |a_{lm+1}|^2 + \ldots + |a_{ll}|^2\right) \tag{3.65}$$

Because the fluctuations in m are assumed to be Gaussian, there should be no bias towards any of the m's, so that each a_{lm} for a given l should be randomly drawn with a Gaussian distribution centered on zero. If $z(l,m)$ is a pseudorandom complex number and $b_l(l)$ is the beam function for a given l (generated from the FWHM value of the assumed instrumental beam) then the created $a_{lm}(l,m)$ is[15]

$$a_{lm}(l,m) = z(l,m)\sqrt{C_l(l) \times [w_l(l) \times b_l(l)]^2} \tag{3.66}$$

The real and imaginary parts of the complex number z of a given a_{lm} coefficient are both drawn individually from a zero centered Gaussian distribution with variance equal to one except for the cases where $m = 0$ where the imaginary part is zero. With these new a_{lm}s it is possible to generate a new map to be a possible random realization of the C_ls given as input. It should be noted that if one was to compute the power spectrum from these new a_{lm} coefficients it would not be exactly the same because for a given l the m's drawn from a Gaussian distribution centered on zero would not likely sum up exactly to zero.

[15]This is for a temperature map only, because polarization was not considered in this thesis. Including polarization means one has to consider the polarized beam function, with small differences for the $\vec{E}$ and $\vec{B}$ fields.

3.6.4 Subroutines "alm2map", "map2alm" and "alm2cl"

Assuming an array of a_{lm}s available the alm2map subroutine will move from harmonic space back to a map of the sky for a_{lm}'s both for temperature and polarization. The transformations used are the inverse of those described in section 3.3.

The map2alm routine performes the transformations described in section 3.3 numerically. The inserted map must be of ring format and the output is an array of a_{lm}coefficients as best suited to the given map. The maps inserted may be of the temperature or polarization or both, but as always, only temperature was considered for this thesis. Optionally the routine may accept $\cos\theta$ values for an upper and lower bound on the map to be considered and it may include a weight function for quadrature correction. It may also, optionally, be called with precomputed values for the $P_{lm}(\cos\theta)$ and tensor harmonics or the $P_{lm}(\cos\theta)$ alone; otherwise these will be calculated by recursion.

In addition to the mathematical description in section 3.3, the routine needs to consider the effect of the discrete pixel values that all HEALPix maps will have.

3.6.5 Subroutine "rotate_alm"

The pixelization of the HEALPix map is unique for a given orientation. This means that rotating the pixel grid for a given map will not exactly recreate the same map, and so it is necessary to determine the value for all pixels in the new map from the old one. The "rotate_alm" subroutine performs this operation in harmonic space so that if fed into the "alm2map" subroutine, the map produced will be the original one rotated the specified orientation as far as the now newly oriented (relative to the map) pixels will allow it. The rotations are defined on the Euler rotation angles ψ, ϕ, θ, they themselves being defined as

ψ : Rotation about the original z-axis
ϕ : Rotation about the original y-axis
θ : Rotation about the original z-axis

in that order. Equivalently;

θ : Rotation about the original z-axis
ϕ : Rotation about the new y-axis
ψ : Rotation about the new z-axis

with all rotations defined for $[2\pi, -2\pi]$ and the routine is called with the map, l_{max} (i.e. the largest l defined) and the three desired Euler angles to return the new a_{lm}'s. They are performed recursively on the spherical harmonics

directly using the *Wigner rotation matrices*, [42] D(R) for a rotation R. They have the following properties;

$$D(R_1R_2) = D(R_1)D(R_2) \tag{3.67}$$

$$D(R^{-1}) = D^{-1}(R) \tag{3.68}$$

$$D^\dagger D = DD^\dagger = I \tag{3.69}$$

where R^{-1} represents the inverse rotation and $D^\dagger$ is the conjugate transpose of D. The D matrix itself is the irreducible representation of the SU(3) and SO(2) unitary matrices. This is a matrix of size $(2j+1) \times (2j+1)$ where j is the degree of the rotation group for the operation. Because of identity (3.67), it is possible to split the rotation in three parts by defining a "small" d matrix such that

$$D_{jmm'}(\theta, \phi, \psi) = e^{im\theta} d_{jmm'}(\phi) e^{-im'\psi} \tag{3.70}$$

where d is a real matrix and a function of the angle ϕ only. In the subroutine the d matrix is expressed as

$$\begin{aligned} d_{jm'm}(\phi) &= \sqrt{\frac{j-m}{j-m'}} d_{(j-1/2)(m+1/2)(m'+1/2)}(\phi) \sin\frac{\phi}{2} \\ &- \sqrt{\frac{j+m}{j-m'}} d_{(j-1/2)(m-1/2)(m'+1/2)}(\phi) \sin\frac{\phi}{2} \end{aligned} \tag{3.71}$$

so that the d matrix may be recursively calculated.

In spherical harmonics

$$D_{jm0}(\theta, \phi, \psi) = \sqrt{\frac{4\pi}{2l+1}} Y_{lm}(\phi, \psi) \tag{3.72}$$

In general, the Wigner matrices calculated in F90 may in some cases loose significant digits [43]. For this thesis it was assumed that round off errors were negligible.

3.7 Other Routines

- Subroutines "ang2xxx", "pix2xxx", "vec2xxx", "ring2nest" and "nest2ring". These subroutines will convert back and forht between angles, vectors and pixel number for both the nested and ring scheme.
- Subroutine "input_map". Routine to read a map from a FITS file to an F90 program.

3.7.1 Subroutine "neighbours_nest"

The neighbours_nest subroutine will, if given a specified pixel number and N_{side} number, return all the number of neighbouring pixels sharing both edges and vertexes as they appear in the nested scheme.

3.7.2 "Mollview" Visualization

The Mollweide projection of a sphere is an equal area projection where the sphere is projected to a 2:1 ellipse. In this thesis the Mollweide projection was computed by the "mollview" IDL subroutine.

The Mollweide projection is not conformal; shapes are distorted more than they would be in a truly conformal projection. This is called *shearing* and occurs in the ϕ direction and more towards the poles. However, shapes are not distorted along either the lines of tangency or along the map's central meridian, but shape distortion increases rapidly as you move away from these lines. It is possible to interrupt the projection (in effect placing more central meridians into the map) to reduce this shape distortion at the cost of creating many "tears" in the map. The "mollview" routine projects the map onto a single ellipse.

Mollweide maps show lines of equal θ as parallel straight lines and lines of equal ϕ as nonparallel lines that become increasingly curved as you move farther away from the map's central meridian until the edges 180 degrees away from the map's central meridian ($\theta = \pi$). Tearing occurs along these edges. For this reason it is possible to easily visualize the ring format; simply plot the rings underneath each other. Mollweide projections are equivalent, that is the total areas of the different map features are always the same relative to each other and so the maps do not suffer from compression. The disadvantages of using the Mollweide projection are that it is not equidistant (there are no point or points from which all distances are shown accurately) and it is not azimuthal (there are no point or points from which all directions are shown accurately).

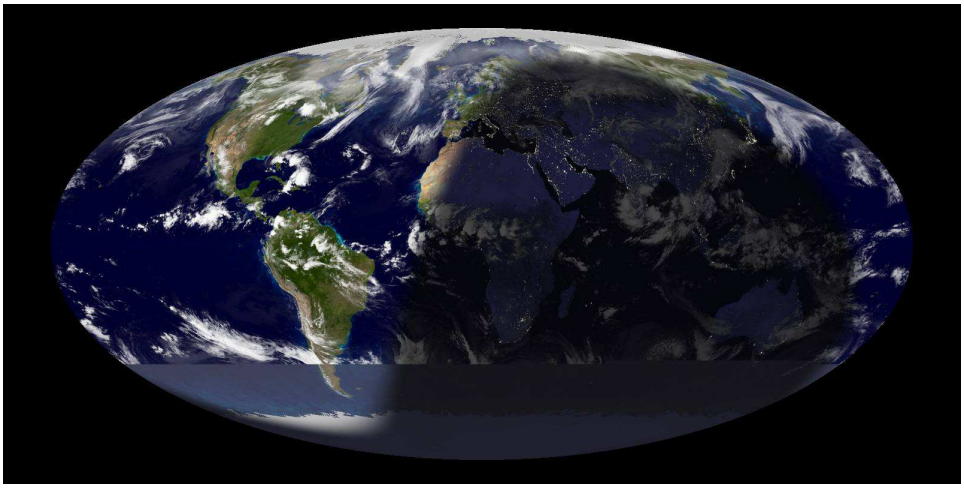

Figure 3.15: Mollweide projection of the solar cover of the Earth on May 20th 2009 at 21:20 CET. The cloud cover was from within the last three hours, except for the southernmost part where no data was available. (from die.net)

Chapter 4

The Program

The program written for this thesis completes three tasks:

1. Finding and isolating spots as defined in the thesis description (section 1.1)
2. Calculating the spot obliquity as defined in the thesis description
3. Caclulating the ellipticity parameter, also as defined in the thesis description

The second and third are quite interlinked and handled by the same subroutine ("find_ellipticity"), the first is a preliminary step requiring its own subroutine ("Spotfinder").

4.1 Spotfinder

With an N_{side} , a temperature threshold, a CMB-map to apply it to and an indication if the spot is negative or positive, this routine will return an array of the pixels in a $N_{\text{relevant pix}} \times 2$ format with the other number being a key unique for each spot. Spotfinder does, first of all, create an array of what it considers *relevant pixels* for isolating spots. The relevant pixels are the pixels whose temperature value is higher than the threshold (or below if cold spots are considered) and whose neighbours include at least one other such pixel. One pixel spots are not considered as relevant, because they cannot contribute to the ellipticity statistics. The task for it is then to sort all relevant pixels in such a way as to make sure that all neighbouring relevant pixels have the same *unique* [1] spot key, as well as appearing in the output array without any pixels from other spots between them. A "neighbouring pixel" is defined as from the HEALPix F90 library "neighbours_nest" routine; all

[1] Unique in the sense that no other spot is allowed that key — obviously all pixels within the same spot must share the same key.

pixels returned — eight for most pixels, except for 8 pixels[2] which only have seven neighbours — will, if relevant, be considered neighbours and part of the same spot.

Although sorting algorithms are amongst the most studied in the field of informatics, this problem is slightly different from the ones usually targeted by such algorithms because it required a genuinely two dimensional sorting. This task was achieved by using one of two different methods — one brute force algorithm and one taking its basic idea from linked list sorting. Both of these algorithms use the nested enumeration scheme in order to gain access to the "neighbours_nest" routine included in the HEALPix package.

4.1.1 Brute Force Algorithm

This initial algorithm was not fast, but easy to code and provided a semi-independent check for the final algorithm. On the WMAP 5-year vw map, $N_{side} = 512$, with a cut at 100 μK the code ran for about 120 seconds on the test machine. The algorithm can be summarized as:

1. Run through the array over relevant pixels once; assign a spot key to all pixels.

2. This key is saved in both the relevant pixels array and a specialized array of size N_{pix} (for ease of access — array index is the same as pixel number)

3. Run through again and compare neighbouring pixels key. If not the same (and they will not be the first time), both pixels are given the key that is the lower of the two.

4. Repeat last step until all neighbouring pixels have the same key.

5. Sort the resulting array; here by using the Quicksort algorithm [44], by its key, but make sure that the pixels are moved with their corresponding key.

The main problem with this algorithm regarding speed is the second last step. Because most spots (and especially large spots) will be entered from different places as the program traverses the array of relevant pixels, the "lowest" keys from each entry point will spread throughout the spot, and will then have to be overwritten by the actual lowest one later, so in practice the number of runs of the array will be proportional to the number of pixels in its largest spot. The theoretical worst case is for all relevant pixels to merge into one giant spot (something that more or less happens if absolute value of the cut is $\lesssim 60$) with very high numbered pixels next to the one with the

[2]The southernmost and northernmost pixel of the (divided) four equatorial $N_{side} = 1$ pixels will only have seven neighbours.

lowest key and then descending numbers on the pixels further away (this can not be regarded as unrealistic, considering it uses the nested scheme). When a full analysis is performed on a map, the starting and ending point cuts are typically + and -500μK, in such a way as giving a time performance dominated by cases close to the worst case at low cuts. Its average time consumption, as well as a worst case performance, is therefore $O(n^2)$.

This algorithm has a best case time consumption of $O(n)$. This is when the spots appear in such an order as to never be entered into from more than one place, and then have the neighbouring pixels all in ascending order from the initial one. This is, however, very unlikely for a randomly generated CMB map and does not happen on the WMAP 5-year data maps.

The brute force algorithms sole redeeming feature (apart from its role as control for the other one) is an $O(n)$ memory usage, as only two arrays of size $\mathrm{N_{pix}}$ and $\mathrm{N_{relevant\ pix}}$ are needed.

4.1.2 Linked List Algorithm

The second algorithm used was the "linked list algorithm". For its superior speed it ended up being preferred to the brute force algorithm. This algorithm used between 0.7 and 1.0 seconds on the test machine and the WMAP 5-year vw $\mathrm{N_{side}} = 512$ map with a cut at 100 μK that the brute force algorithm spent 120 seconds sorting. The idea is to make a linked list consisting of all pixels in a spot. As the problem is again that the code might enter a spot from different directions (each with a different identification key), the gain stems from moving the entire list when one pixel is determined to have a neighbour with a lower key. For this algorithm, two new types were defined:

1. Pixel: A type containing the pixel number (an integer), a pointer to the next pixel (pixel type, that is) and a logical "placed" to determine if it had been viewed before.

2. Spot: A type containing four bits: a pointer to the first pixel in each spot list, a pointer to the last ("current") pixel in the list, a logical "obsolete" that would be true if the spot has been discovered to be part of a larger one and the list has been moved there and an integer remembering what spot took the list.

With these, the algorithm can be summarized as:

1. Save the pixel number to all relevant pixels in an array of length $\mathrm{N_{pix}}$ (for ease of access — array index is the same as pixel number). The non relevant pixels are marked in this array by a number not between 0 and $\mathrm{N_{pix}} - 1$. This array will serve to hold the spot keys.

2. Create an array of the type pixel the size of $\mathrm{N_{relevant\ pix}}$, an array of the type spot the size of $\mathrm{N_{pix}}$ as well as an array containing the entries of the second of these.

3. Run through the array over pixels. Each pixel is linked to its neighbours[3], to form a chain starting at the spot in the array over spots. The key to this spot, one of the pixels number, will be saved in the array for the spot keys.

4. If a neighbouring pixel is found that has not already been found, it will simply be added to the chain, and its key updated.

5. If a neighbouring relevant pixel has already been found before, the two chains will be joined at the neighbours spot and the old spot will be considered obsolete. The array of keys will not be updated, in stead any search through an obsolete key will be rerouted to the new spot.

6. When completed, the array over spots is run through, all pixels that belong together in each spot are now read in turn through the chain list. No sorting is necessary as all pixels within the same spot are already listed together.

This algorithm turned out to be $\gtrsim 100$ times faster than the brute force one. The best case scenario here is, as for brute force, for all spots to be entered into only once with no need for list swapping. This admits a time use of $O(n)$. The worst case is for all spots to merge into one, and then for the program to enter into that spot in such a way as to have a maximum number of list moves and for each subsequent pixel to give a maximum number of obsolete keys to be rerouted through. This would in case give a time of $O(n \times m)$ where m is the number of entry points into a given spot. In worst case $m \sim n$ and time spent is $O(n^2)$[4]. On average the number of iterations scale with n times number of "obsolete reroutes", who in turn are (on average) proportional to $\log m$. The average running time is thus of order $O(n \log n)$.

The memory usage here is linear too, as it only needs four arrays, none larger than N_{pix}. The memory usage is still a little larger than the brute force method, but only negligibly so.

4.2 Ellipticity and Obliquity Calculator

The code for finding ellipses is divided into two different subroutines. The first, "ellipse_NEST", has no distinct properties other than to chop the array of spots up into arrays of individual spots, calling the other and handling the output from that subroutine. It also calculates the statistics for the map after the ellipticity calculations have been made for all spots found. The second subroutine, "find_ellipticity", will calculate the ellipticity for one individual spot in two different ways, the cosine formula and the haversine formula (see

[3] Not strictly true; it suffices to know that two pixels are in the same spot to link them.

[4] In practice it will still be faster than the average time used by the brute force algorithm as m is at most one third plus one the number of pixels in a spot.

section B.2 for a complete derivation) as well as calculating the obliquity for the spot in both cases.

4.2.1 find_ellipticity

The subroutine "find_ellipticity" will take as input an array of pixels representing a spot, as well as a copy of the original map. The procedure it will follow is then:

1. Double the N_{side} for the spot; that is create a new array with new entries for the new (better resolution) spot.

2. Make the following sorting: Discard all pixels that have (at least) a relevant pixel on either side of it, that is with relevant neighbours occupying place 1 and 5, 2 and 6, 3 and 7 or 4 and 8 as defined by the neighbours_nest routine. No pixels with fewer than 8 neighbours will be discarded.

3. Calculate the distance between each pixel in the spot not discarded. The two pixels with the greatest distance form the major axis along a great circle between them.

4. Calculate the spot obliquity ε.

5. Calculate the distance from all pixels down to the major axis. The average of the two pixels on each side with the greatest such distance is the semi-minor axis.

6. Calculate the ellipticity

$$\epsilon = \frac{a}{b} \tag{4.1}$$

   where a is semi-major axis and b is semi-minor axis.

Computationally step 3 gives this algorithm a time consumption of $O(n^2)$. This is also the reason for step 2: it greatly reduces the running time, especially for large spots. The sorting is significantly strong to make running times for the WMAP 5-year vw map of $N_{side} = 512$ map with a cut at 100 μK about 4.5 seconds on the test machine. The quadratic behaviour of the algorithm is made worse by step 1. Step 1 is included in order to avoid cases where all pixels in the spot lie on a chain with no significant distance from the major axis. This would then give a potentially close to zero semi-minor axis and by that a diverging ellipticity, heavily skewing the statistics. This step was performed as explained under the description of the nested scheme in section 3.5.1.

Step 2 is performed by including a "black and white" version of the map (where all pixels are marked as either relevant or non-relevant) on which

the neighbours of a given pixel can be easily identified without the need for running through the array of the spot pixel numbers. The sorting is not entirely well founded; while in a Euclidean space it will always be true that the distance from a given relevant pixel to a relevant pixel with two relevant neighbours on opposite sides is less than to at least one of those two neighbours, this is not always true on a curved sphere in general and in particular not for the HEALPix map. In practice, however, the difference turned out to be negligible (although observable) and, considering the $O(n^2)$ time behaviour, substantial amounts of time is saved per spot.

The steps 3 and 5 are performed in two different ways, one based on cosines and one based on haversines. For method one, the cosine formula, the formula used in step 3 was

$$\cos(\Lambda) = \cos(\theta_A)\cos(\theta_B) + \sin(\theta_A)\sin(\theta_B)\cos(\phi_A - \phi_B) \tag{4.2}$$

where Λ is the great circle distance between points A and B. What was then actually computed was

$$\Lambda = \arccos\left(\cos(\theta_A)\cos(\theta_B) + \sin(\theta_A)\sin(\theta_B)\cos(\phi_A - \phi_B)\right). \tag{4.3}$$

Step 5 was comprised of five different calculations; two to get the distances λ_A and λ_B from the pixel to each of the greatest distance pixels (A and B, using formula (4.3)), one based on the law of cosines to get the angle between the major axis and the direction to the pixel considered ($\angle A$)

$$\angle A = \arccos\left(\frac{\cos(\lambda_B) - \cos(\Lambda)\cos(\lambda_A)}{\sin(\lambda)}\right), \tag{4.4}$$

one to determine the distance from the center of that pixel to the major axis using the spherical law of sines

$$\frac{\sin a}{\sin A} = \frac{\sin b}{\sin B} = \frac{\sin c}{\sin C} \tag{4.5}$$

and one to determine which side of the major axis the pixel in question is on. This was done by considering a vector pointing in the direction of the pixel and taking the dot product with a vector [5] orthogonal to the plane spanned by the major axis great circle. In the unlikely event that such a calculation yields a zero, the distance to the great circle is either zero or so small it can be neglected.

While these formulae are all analytically correct, some may lead to round-off errors when the distance considered is small. To prevent round-off errors and to get a semi-independent check for the results containing cosines, the second haversine based way was also included in the final data. Here equation (4.2) was replaced by the haversine formula (for a sphere with radius = 1)

$$\mathrm{hav}(\Lambda) = \mathrm{hav}(\theta_A - \theta_B) + \sin(\phi_A)\sin(\phi_B)\mathrm{hav}(\phi_A - \phi_B), \tag{4.6}$$

[5] As this step is performed after step 4, such a vector has already been found.

where Λ still is the great circle distance between points A and B. The identities

$$\mathrm{hav}(a) = \frac{\mathrm{vers}(a)}{2} = \sin^2\left(\frac{a}{2}\right) \tag{4.7}$$

and

$$\mathrm{hav}^{-1}(a) = 2\arcsin(\sqrt{a}) \tag{4.8}$$

enables equation 4.6 to be rewritten as

$$\Lambda = 2\arcsin\left(\sqrt{\sin^2\left(\frac{\theta_A - \theta_B}{2}\right) + \sin(\phi_A)\sin(\phi_B)\sin^2\left(\frac{\phi_A - \phi_B}{2}\right)}\right). \tag{4.9}$$

While equation (4.9) is computationally slower to calculate than (4.3) because it calls one more function (the square root) as well as squaring sines, it is more robust against round-off errors because there is no cosine to consider. This avoids the problem with the nines after the decimal point on the cosine being carried as significant digits by the computer, and accuracy becoming very poor when a small angle must be evaluated from its cosine[45]. Step 5 was again made up by the same five different parts, this time calculated by haversines. The first two parts are, as before, finding the distances λ_A and λ_B, this time using equation (4.9). The next part is finding the angle A, this time with the haversine analogue to the law of cosines; the law of haversines

$$\mathrm{hav}(\angle A) = \frac{\mathrm{hav}(\lambda_B) - \mathrm{hav}(\lambda_A - \Lambda)}{\sin(\lambda_A)\sin(\Lambda)}. \tag{4.10}$$

This can be expressed as

$$\angle A = 2\arcsin\left(\sqrt{\frac{\sin^2\left(\frac{\lambda_B}{2}\right) - \sin^2\left(\frac{\lambda_A}{2}\right)}{\sin(\lambda_A)\sin(\Lambda)}}\right). \tag{4.11}$$

The fourth part (finding the norm from the pixel to the major axis) and fifth part (determining which side of the major axis the pixel is on) were performed the same way on both methods.

Step 4 was calculated by vectors. The *obliquity* ε is defined as the inclination of the major axis great circle to the $\theta = \pi/2$ plane. This translates into calculating the angle between a vector $\vec{z}$ orthogonal to the $\theta = \pi/2$ plane and the vector $\vec{v}$ orthogonal to the major axis great circle plane, in other words the inverse cosine to the dot product between the normalized versions of the two. For ease of calculation Cartesian coordinates were used; the first one is then simply the vector $(0, 0, 1)$. $\vec{v}$ is found by normalizing the vector product between the vectors pointing to the centre of pixels A and B

as calculated by the "pix2vec_nest" routine from the HEALPix F90 library. As vector product vectors do not commute, the direction of $\vec{v}$ can be either up or down, depending on what pixel ended up being considered as A. This is corrected by a simple test, and is inconsequential for the vector test used in step 5.

The obliquity is a fairly useless number when calculated for spots close to the poles, as they will all be close to $\pi/2$, but can be used for testing for preferred directions amongst spots close to equator. Fortunately, it is possible to test against $\vec{z}$ other than $(0, 0, 1)$, and by a Monte Carlo simulation one can test for a preferred direction of the spots in the current map. For this reason, the subroutine is designed to take as input an vector against which obliquity is tested. By disallowing spots further away from the (newly defined) equator than $\sim 20°$, it was found that the number of spots was still large enough to give small statistical error bars and by testing all directions on the sky it is possible to find the preferred direction (if any) of the spots in that $\pm 20°$ band.

Finally, step 6 is to calculate the spot *ellipticity*. This is straightforward; if a is the semi major axis, and b is the average between the greatest distance on each side of the major axis, then the ellipticity ϵ is

$$\epsilon = \frac{a}{b}. \tag{4.1}$$

This number, calculated twice (one for the cosine run and one for the haversine run) along with the two obliquities is what this subroutine returns to its parent subroutine, "ellipse_NEST". As this is calculated in the same way both times, the difference is not great. However, there *is* a difference as the two methods will yield slightly different results on the distances between pixels, and may thus end up returning different pixels A and B to form the major axis in a spot.

Optional function

As an optional function this subroutine can also change the "black and white" HEALPix map to reflect the spot obliquity or the spot ellipticity on the position of the spot pixels for a visual output. This was used to visually confirm the numbers generated by the routine.

4.2.2 ellipse_NEST

The simple subroutine "ellipse_NEST" will, if given an $N_{pix} \times 2$ array as produced by Spotfinder, do the following:

1. Divide the array into individual arrays, one for each spot.
2. Call the already described subroutine "find_ellipticity" with the input parameters N_{side} , a "black and white" map of spots and of course the

array of the spot pixel indexes. Optionally a vector $\vec{z}$ against which to calculate obliquity (different from the standard $\vec{z} = (0, 0, 1)$ could be included in the call.

3. Receive the output from the above noted subroutine; always an array containing the numbers ellipticity and obliquity (calculated with both cosines and haversines)

4. Collect the statistics from all spots and calculate mean ellipticity, mean obliquity and (statistical) confidence intervals.

The spot properties collected by the program is grouped according to the number of pixels in the spot. In addition the routine has the job of calculating the means

$$\bar{y} = \frac{1}{n} \sum_{i=1}^{n} y_i, \tag{4.12}$$

the variances

$$s^2 = \frac{1}{n-1} \sum_{i=1}^{n} (y_i - \overline{y})^2 \tag{4.13}$$

and estimate the 95% confidence intervals

$$T = \bar{y} \pm Z \frac{\sigma}{\sqrt{n}} \tag{4.14}$$

where n is the number of spots and Z is 1.960 for large n. All spots are weighted equally without regard to size or temperature gradients. To estimate the value of Z the distribution of values for ellipticity and obliquity were all assumed to be Gaussian. The number of spots was assumed to be large, in which case Z converges to 1.968 for a 95% confidence interval.

Also, the *skewness*

$$\gamma_1 = \frac{\mu_3}{s^3} \tag{4.15}$$

and *kurtosis*

$$\gamma_2 = \frac{\mu_4}{s^4} \tag{4.16}$$

where

$$\mu_3 = \frac{1}{n-1} \sum_{i=1}^{n} (y_i - \overline{y})^3 \tag{4.17}$$

and

$$\mu_4 = \frac{1}{n-1} \sum_{i=1}^{n} (y_i - \overline{y})^4 . \tag{4.18}$$

was computed. Skewness is a measure of how skewed a distribution is; a perfectly symmetric distribution (like a Gaussian) has a skewness of zero, while a distribution with values on one side of the mean tend to be further away than the on the other has a skewness, increasing for a higher effect. The sign determines if that side is below (minus) or above (plus). Kurtosis

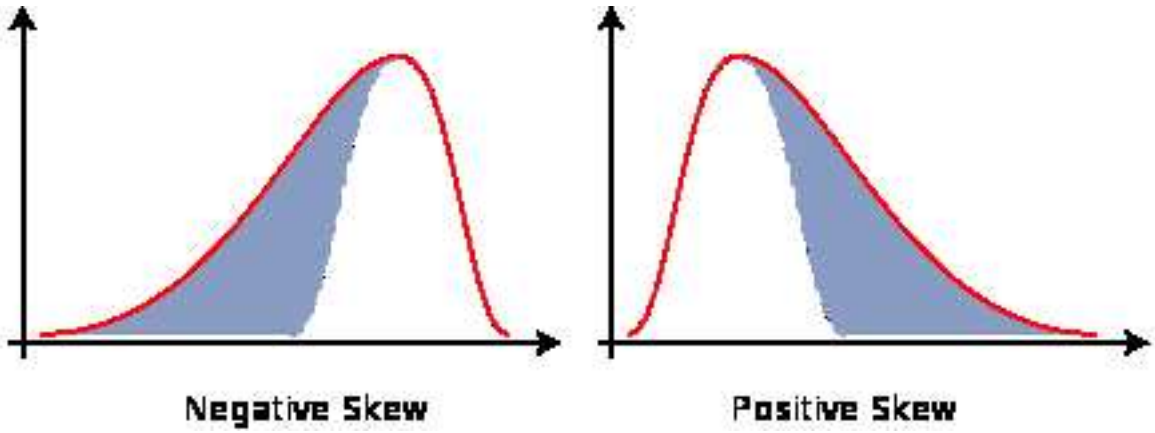

Figure 4.1: Examles of skewed distributions for negative skewness (left) and positive skewness (right) (From wikimedia commons)

is a measure of whether the data are peaked or flat relative to a normal distribution. That is, data sets with high kurtosis tend to have a distinct peak near the mean, decline rather rapidly, and have heavy tails. Data sets with low kurtosis tend to have a flat top near the mean rather than a sharp peak. The Gaussian distribution has $\gamma_2 = 3$. A distribution with higher kurtosis than this is called *leptokurtic* and a distribution with lower kurtosis is called *platykurtic*. A uniform distribution would be the extreme case with a kurtosis of one.

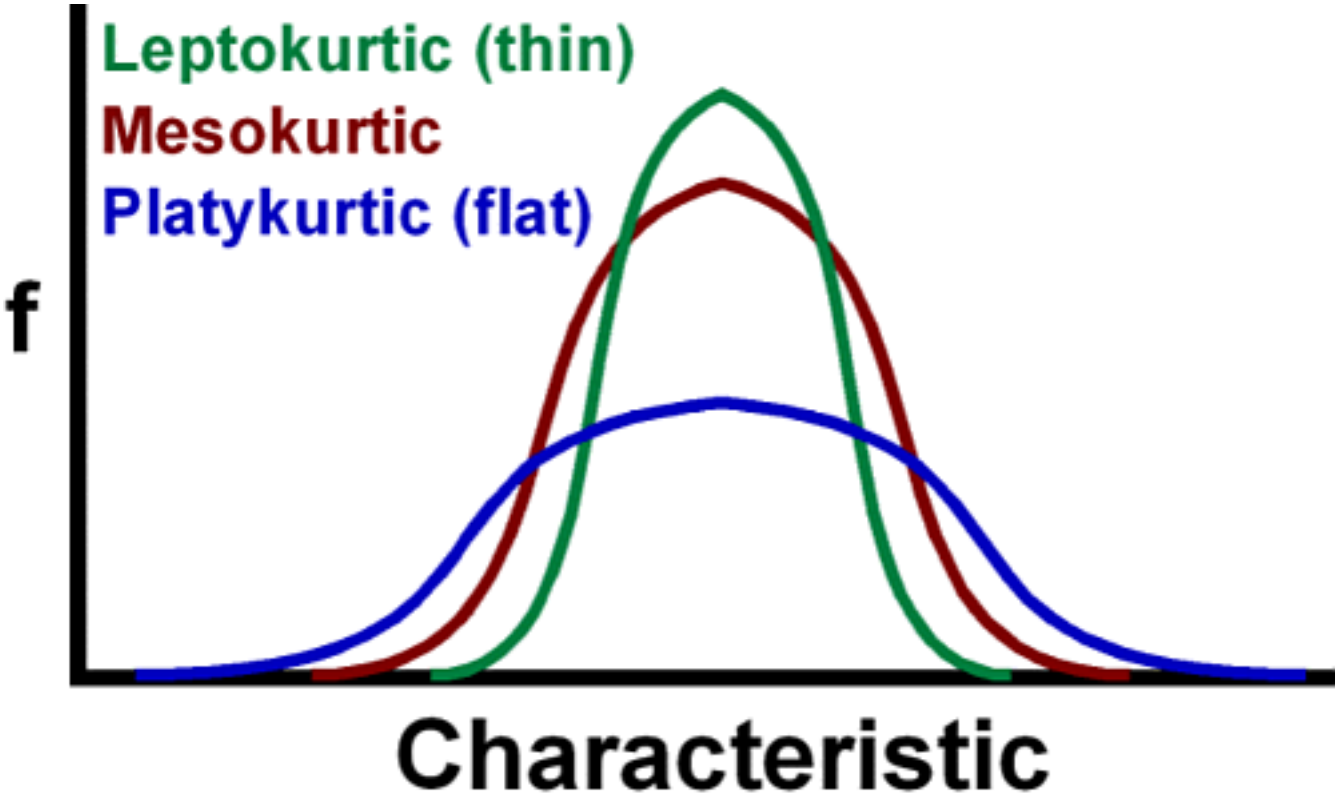

Figure 4.2: Example of two distributions comparing kurtosis to the Gaussian. (from UWSP)

Chapter 5

Results and Lessons Learned

Using the programs described in chapter 4 it was possible to compute the ellipticity and obliquity for CMB maps in the Q, V and W filters as well as for the combined VW map. The analysis was performed for the thresholds ranging from -500 for negatively defined spots (maps where the only "white" pixels are those with value less than -500μK) to -60 (still for negative spots) and then from positive 60μK (spots where the only "white" pixels are above 60μK) to 500μK at every 20th μK. The ellipticity and obliquity was calculated for

1. All spots (including the ones with only two pixels).
2. All spots containing more than two pixels.
3. Spots with > 3 pixels.
4. Spots with > 8 pixels.
5. Spots with > 20 pixels.
6. Spots with > 50 pixels.
7. Spots with > 100 pixels.
8. Spots with > 300 pixels.

The results are gathered for the VW map (see figure 3.6(f)) on a positive cut of 100μK is shown in table 5.1. The obliquity shown is measured against the "natural" equator, i.e. the $\vec{z} = (0, 0, 1)$ vector. Excess ellipticity is only evident for spots smaller than 20 pixels, and clearly for spots smaller than 8 pixels. This is due to a higher probability for smaller spots of consisting only of pixels placed vertically, horizontally or diagonally on a row, resulting in such spots having ellipticity in excess of 10, and hence skewing the results towards a higher mean ellipticity. This is clearly evident by the higher positive skewness shown. The kurtosis is also higher, because fatter tails on the

distribution of spot ellipticity will push the $(y_i - \overline{y})^4$ part of equation (4.18) higher. Figure 5.1 shows the "black and white" map of the spots found in the same case as for table 5.1 except that the spots have been color coded to highlight their ellipticity in the range from 1 to 4 with zero (dark blue) representing non–relevant pixels.

Table 5.1 highlights the difference between the cosine formula and the haversine formula. While there is no significant difference between the ellipticity results obtained either way, the difference in obliquity is substantial. All maps tested performed the same way. Also 1000 simulated maps were tested. Their results can be found in table 5.2. The results obtained are with mask, noise and a 7" beam and they agree show that the results from the real tests agree with a Gaussian standard model.

In addition to the primary ellipticity results the obliquity of all spots was tested against the equator rings orthogonal to vectors pointing at all pixels on a $N_{side} = 32$ map. This analysis seem to show a very significant detection, but this is masked by the fact that the statistical confidence intervals in the obliquity testing is bad: spots close to the (newly defined) poles will contribute to the number n in equation (4.14) but will always have obliquities close to $\pi/2$. The analysis was performed by taking all spots into account and time constraints prevented any further analysis. Figures 5.2 and 5.3 can be compared to 5.4 and 5.5 to see that even if the detection looks significant, it is equally strong in a simulated map.

5.1 Testing the Results

The results obtained for ellipticity and to some extent for obliquity were both inconsistent with those obtained by V.G. Gurzadyan et al [2, 3]. The inconsistency in the ellipticity measures may be because of the slight differences in defining semi-major axis, but the differences in ellipticity by scale found by Gurzadyan (showing a significantly higher ellipticity if all spots of > 20 pixels are considered compared to if only spots > 50 or > 100 are considered)[3] was not reproduced. Investigating possible sources of errors then becomes even more important. In order to do so, several strategies were:

1. Testing the ellipticity with both the described formulae (cosine and haversine).
2. Investigate the possibility that spots are defined and/or found erroneously.
    - Testing by brute force through the brute force method described in section 4.1.1.
    - Check on the obvious cases where there are either no spots at all, or the entire map is one big spot.

		Cosine formula					
		Ellipticity			Obliquity		
Spot size	N_{spots}	Ellipticity	Skewness	Kurtosis	Obliquity	Skewness	Kurtosis
> 2	11468	1.9844 ± 0.0160	2.451	13.42	62.054 ± 0.411	-0.7192	2.282
> 3	8607	1.8512 ± 0.0157	2.569	15.82	61.867 ± 0.467	-0.7268	2.306
> 8	4615	1.6396 ± 0.0139	1.988	10.52	61.190 ± 0.628	-0.6568	2.251
> 20	2737	1.5905 ± 0.0151	1.279	5.430	61.081 ± 0.802	-0.6013	2.213
> 50	1385	1.6143 ± 0.0213	1.159	4.829	60.823 ± 1.126	-0.5612	2.202
> 100	679	1.6226 ± 0.0310	1.170	4.737	60.045 ± 1.631	-0.5353	2.203
> 300	180	1.6053 ± 0.0597	0.8521	2.869	59.673 ± 3.306	-0.5098	2.051
		Haversine formula					
		Ellipticity			Obliquity		
Spot size	N_{spots}	Ellipticity	Skewness	Kurtosis	Obliquity	Skewness	Kurtosis
> 2	11468	1.9840 ± 0.0160	2.448	13.40	62.054 ± 0.411	-0.7192	2.282
> 3	8607	1.8508 ± 0.0157	2.565	15.79	61.868 ± 0.467	-0.7268	2.306
> 8	4615	1.6395 ± 0.0139	1.984	10.51	61.190 ± 0.628	-0.6568	2.251
> 20	2737	1.5906 ± 0.0151	1.280	5.431	61.081 ± 0.802	-0.6013	2.213
> 50	1385	1.6143 ± 0.0212	1.159	4.829	60.823 ± 1.126	-0.5612	2.201
> 100	679	1.6227 ± 0.0310	1.1701	4.737	60.045 ± 1.631	-0.5353	2.203
> 300	180	1.6053 ± 0.0591	0.8521	2.868	59.673 ± 3.306	-0.5098	2.051

Table 5.1: Data for the VW map with a positive 100μK cut. The values for Ellipticity and Obliquity is given to 95% confidence. The program found 386473 relevant pixels 18487 spots (including spots of just 2 pixels). Notice how the statistics for ellipticity and obliquity are almost identical for the two formulae and do not differ at all until the fifth significant digit (included here to highlight the difference). N_{spots} is the number of spots found in the given category.

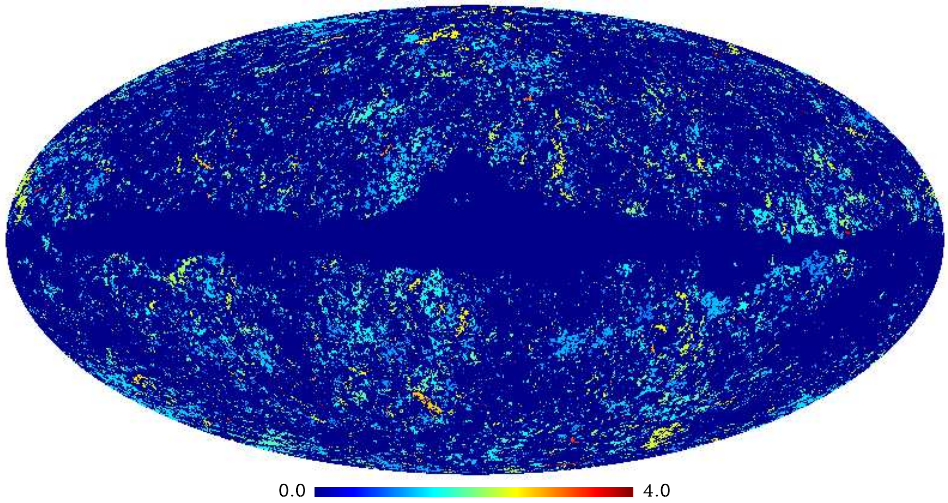

(a) Full sky color coded spot map

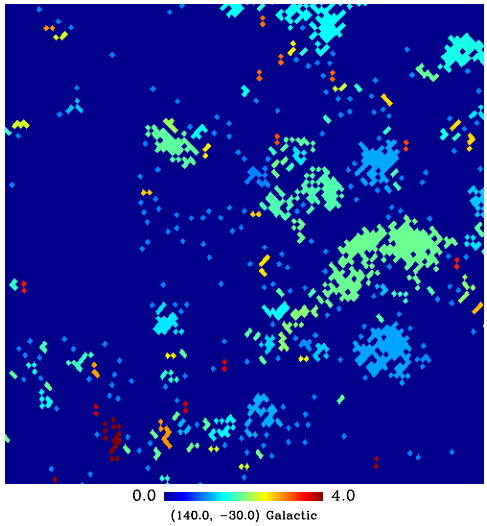

(b) Full sky color coded spot map

Figure 5.1: Color coded spot map for the VW map with positive cut of 100μK. The gnomview map shows an area centered on 2 and shows clearly some of the smaller spots that contribute

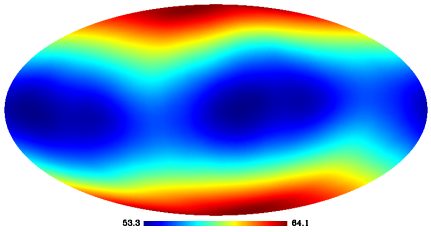

(a) > 3 pixel map

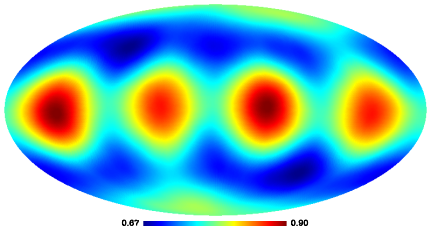

(b) > 3 pixel map 95% confidence intervals

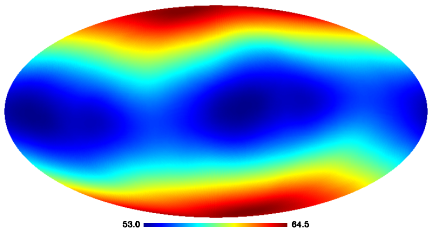

(c) > 8 pixel map

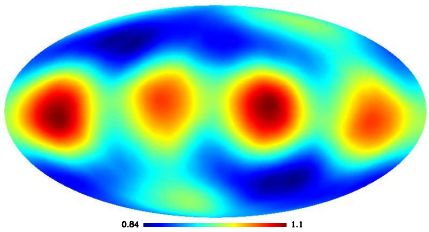

(d) > 8 pixel map 95% confidence intervals

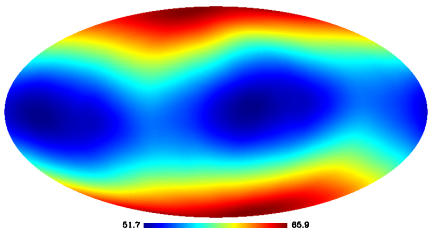

(e) > 20 pixel map

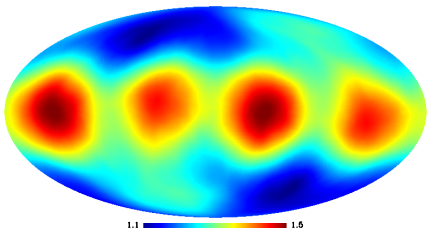

(f) > 20 pixel map 95% confidence intervals

Figure 5.2: Obliquity maps for a positive 100 μK cut on the VW map. The statistical confidence is shown in the neighbouring maps. Showing maps > 3 to > 20.

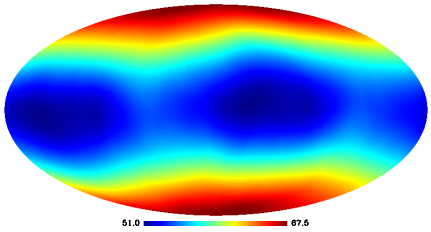

(a) > 50 pixel map

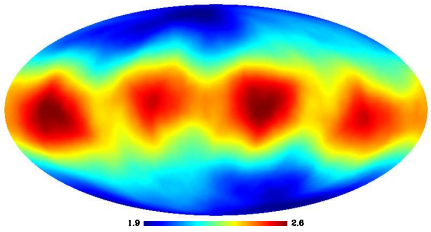

(b) > 50 pixel map 95% confidence intervals

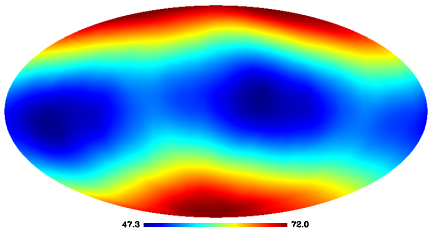

(c) > 100 pixel map

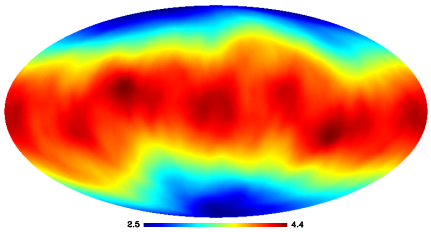

(d) > 100 pixel map 95% confidence intervals

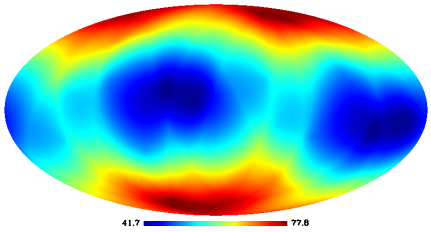

(e) > 300 pixel map

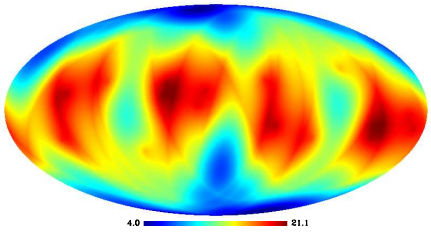

(f) > 300 pixel map 95% confidence intervals

Figure 5.3: Obliquity maps for a positive 100 μK cut on the VW map. The statistical confidence is shown in the neighbouring maps. Showing maps > 50 to > 300.

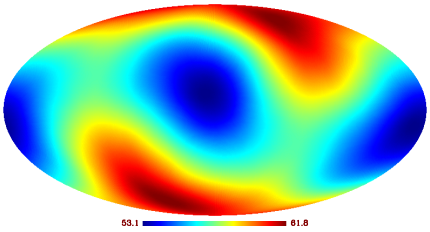

(a) > 3 pixel map

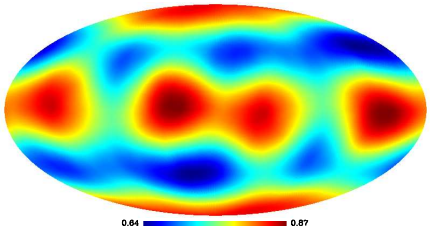

(b) > 3 pixel map 95% confidence intervals

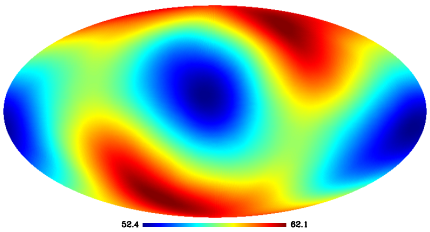

(c) > 8 pixel map

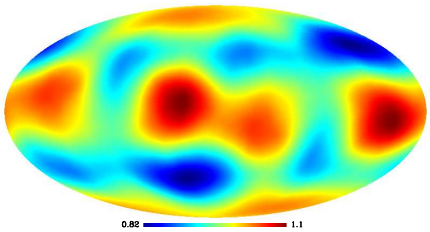

(d) > 8 pixel map 95% confidence intervals

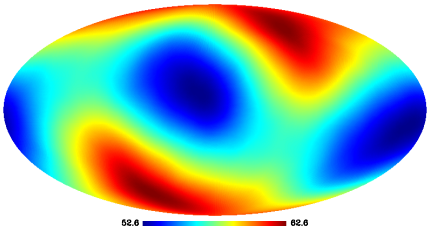

(e) > 20 pixel map

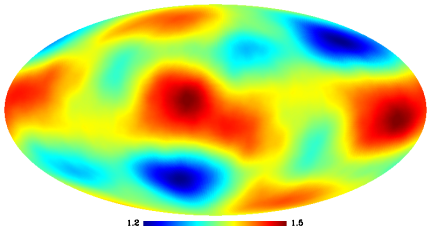

(f) > 20 pixel map 95% confidence intervals

Figure 5.4: Obliquity maps for a positive 100 μK cut on a simulated map. The statistical confidence is shown in the neighbouring maps. Showing maps > 3 to > 20.

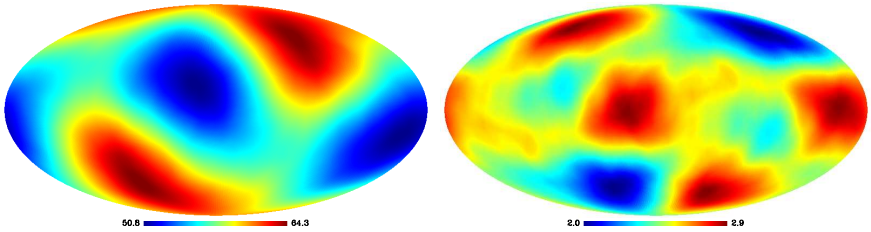

(a) > 50 pixel map

(b) > 50 pixel map 95% confidence intervals

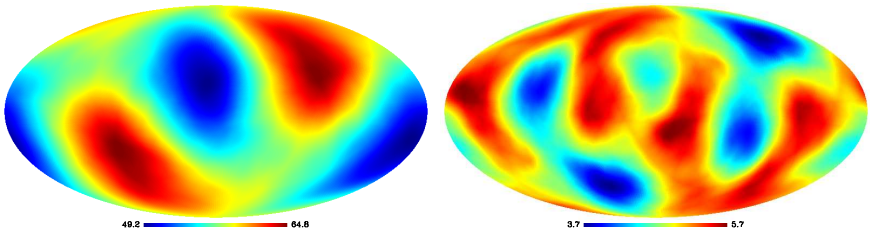

(c) > 100 pixel map

(d) > 100 pixel map 95% confidence intervals

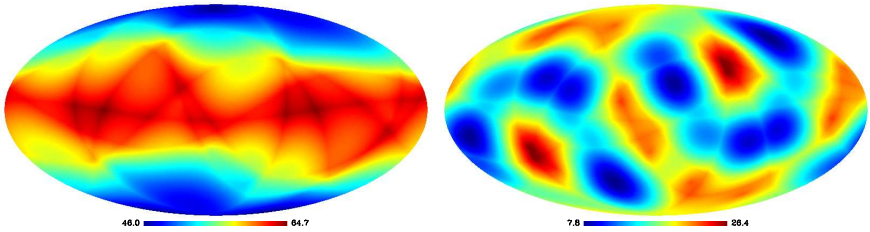

(e) > 300 pixel map

(f) > 300 pixel map 95% confidence intervals

Figure 5.5: Obliquity maps for a positive 100 μK cut on a simulated map. The statistical confidence is shown in the neighbouring maps. Showing maps > 50 to > 300.

Spot size	N_{spots}	Ellipticity	Obliquity
> 2	6675	1.92	58.20
> 3	5346	1.78	59.17
> 8	2654	1.618	58.15
> 20	1205	1.611	59.34
> 50	600	1.600	58.98
> 100	298	1.604	58.83
> 300	45	1.621	59.04

Table 5.2: Mean result for 1000 simulated maps. The values place all real maps well within the confidence intervals. The threshold used was $+100\mu$K.

- Check for cases where the map is user defined.
- Check the generated lists if any of the relevant neighbours are given a different key (see section 4.1) or not found.

3. Check the consistency between maps and expectations.
   - Testing the ellipticity against different maps: simulated CMB maps as well as mock CMB maps containing known geometrical figures. Both maps should be tested with and without noise and mask.
   - Testing against all WMAP maps to check for consistency.
   - Calculate for the same map at different cuts to check for consistency.
   - Testing the same map at different angles as rotated by the HEALPix "rotate_alm*" routine to check for consistency.
   - Testing for different N_{side} on the same maps.
4. Testing the program without the sorting described in step 2, section 4.2.
5. Testing for different size of spot.
6. Testing for beam effects
7. Testing for systematic effects from noise
8. Testing for effects of including/excluding galaxy mask.

5.1.1 Cosine Versus Haversine

While this is explained in section 4.2, it should again be noted that this is not a true independent test. As explained, they have several elements in common throughout the routine so they do not really test anything besides

		Ellipticity			Obliquity		
Spot size	N_{spots}	Ellipticity	Skewness	Kurtosis	Obliquity	Skewness	Kurtosis
> 2	7735	1.993 ± 0.020	2.650	16.30	61.65 ± 0.50	-0.6668	2.213
> 3	5730	1.868 ± 0.020	2.941	21.84	61.29 ± 0.57	-0.6591	2.205
> 8	2862	1.636 ± 0.018	2.179	13.35	60.94 ± 0.78	-0.6075	2.180
> 20	1458	1.579 ± 0.021	1.225	4.696	60.9 ± 1.1	-0.5976	2.2184
> 50	590	1.622 ± 0.033	1.164	4.762	60.4 ± 1.7	-0.5660	2.210
> 100	230	1.636 ± 0.057	1.349	5.411	58.8 ± 2.7	-0.4778	2.062
> 300	39	1.67 ± 0.15	1.345	5.977	56.3 ± 7.6	-0.3670	1.759

Table 5.3: VW map results for haversine calculated spots with a cut of -150μK.

the evaluation of the expressions themselves. They do, however, agree almost perfectly, confirming the lack of round-off errors and strongly indicating the expressions are correctly entered. Round off errors are typically only visible in the third or fourth significant digit for the smallest spots ($\lesssim 8$ pixels) and much less significant for larger spots.

The obliquity results do not necessarily match each other for the two methods on individual spots. For spots whose major axis is nearly equal to the distance between different pixels, the obliquity results may come out very different as round off error differences causes the two methods to choose different major axis. This effect dissapears when the full map is considered, and the difference between the two ($\lesssim 10^{-2}\ ^o$) is much less than the statistical uncertainties ($\sim 1.2\ ^o$ to 95% confidence).

5.1.2 Testing Spotfinder

Although testing Spotfinder was almost a repeat of the tests that were run for the whole program , and indeed used almost all of the steps tried above, it is included here because any error finding and classyfying spots will hurt all the final results. The obvious tests of the map would include testing for different N_{side} , different orientations as generated by the "rotate_alm*" HEALPix routine, different temperature cuts and testing home made maps with known figures (blanks, fulls, spesific figures etc.). In addition to this there were two important test performed; using two different methods (the brute force method described in subsection 4.1.1 and the linked list method described in subsection 4.1.2) and the testing of the list by checking for any lost or misplaced relevant pixels in the final list of spots.

The test against errors in the spot finding process contains the following elements: Run through the array over relevant pixels and check each neighbour for each pixel to see if it has the same key. This is in reality the same as the final step of the brute force method, and so should not be considered truly independent, but it does verify the results found by the brute force method and rule out any computational mistakes. No inconsistent results were found by any of these methods. In addition, the routine performed as expected on the special manually verified maps. Also on rotating the maps, the count of spots was the same except for the special cases where different pixelisation split or merged spots. The tests involving the same map with different N_{side} turned out to give expected results; increasing the N_{side} by a simple split of pixels resulted in the same number of spots being found, reducing the N_{side} by merging pixels did decrease the number of spots[1].

[1] Obviously assuming the map was in its "original" state

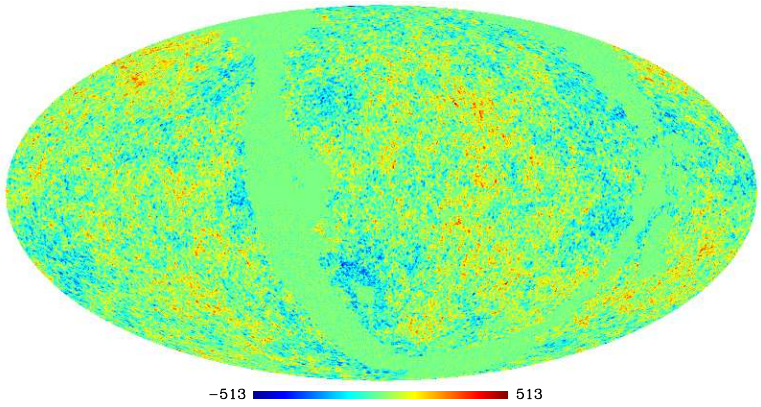

Figure 5.6: Rotated map. Notice the mask.

5.1.3 Consistency Between Maps

This test was performed by generating several maps with known properties: the mock maps containing only a few spots with hand picked properties, maps with known exaggerated sky skewness, maps with known obliquities and maps with increasing smoothing of the above mentioned spots. In all cases, the program performed as expected. The sky galaxy cut does, as expected, widen the margins of error estimated on simulated maps (by decreasing the statistcal data), noise seems to increase the ellipticity for small spots in different maps while doing little for the larger spots, as expected. Also, there is as expected no effect by increasing or decreasing the temperature cut as long as the spots found cover the same pixels.

Another consistency test that was performed was to test the program on input that should give similar but not identical results. It is known that the different WMAP bands essentially give the same results where foregrounds are negligible [46]. The results between the WMAP V, W, Q and VW maps are equal to within a very small margin of error compared to the statistical errors. This holds true for all N_{side} tested (4 - 1024) and for all thresholds tested and is equally true for both ellipticity and obliquity measurements.

Still another consitency test is to test the same map for several different temperature thresholds and N_{side} . This gave expected results, increasing N_{side} will somewhat decrease the ellipticity as long as the map itself is the same (that is, all pixels are divided in four parts of identical value). This is because the position of a pixel is considered to be its centre and the calculation is now performed in what used to be one corner of that same pixel, increasing the distances measured somewhat. Adding this way is a linear operation (adding a small number δ to both semi-major and semi-

minor axis), and gives more significance to the smallest number (the semi-minor axis) because

$$\frac{a}{b} > \frac{a+\delta}{b+\delta} \tag{5.1}$$

when a > b and $\delta > 0$. This was also correct for all maps tested. The effect is not as profound for obliquity because the pixels now considered to have the greatest distance may shift the spot obliquity either way. Conversly, decreasing the N_{side} will increase ellipticity, because of the inverse effect, but here it may also give the effect of merging spots so that ellipticity tends to be a little greater, but not always. Again, the obliquity does not change in any particular way (up or down) except staying fairly close to the ones observed on the original map. This was all measured to be as expected.

The analysis should hold for maps angled differently, that is as rotated by running it through the "map2alm*", "rotate_alm*" and "alm2map*" HEALPix routines. Apart from the difference caused by the pixelization, the results obtained from the test are largely consistent with all differences resulting from information loss and changes due to the differences in pixelisation[2]. This result was independent of the map considered. It was not, however, independent of the N_{side} of the map considered; larger N_{side} supresses this effect. As expected, neither ellipticity nor obliquity showed any preferred change when such an operation was performed, and stayed close to the original map ($\lesssim 1\%$ change)

5.1.4 Testing the Pixel Sorting

In a flat Eucleian space it will always be true that for any square grid the distance from a point p to the centre of a square A is less than the greatest of the two distances from p to the centre of squares B and C provided B and C is on opposite sides of A (either diagonally, horizontally or vertically). Because of the curving of the pixels to keep the pixel area constant this is not necessarily true on a spherical HEALPix map. For this reason the pixel sorting algorithm described in step 2, section 4.2 will sometimes sort away one or both of the true greatest distance pixels (for either semi-major or semi-minor or both).

To test this effect the obvious choice is to test the same map both with and without sorting. The time consumed by the $O(n^2)$ pair matching algorithm for finding the pixels with the greatest between–them–distance (step 3, section 4.2) made a comprehesive test too time consuming to be performed, but tests were made on maps of $N_{side} \leq 512$ though not on the same number of maps as the some of the other tests. Because the time consumption

[2]The pixelisation of a HEALPix map is unique for a particular orientation. This means that while in theory a spacial rotation of a map through spherical harmonics preserves the map exactly, HEALPix cannot reproduce the same map exactly when pixelized.

scales as $O(n^2)$ with the number of pixels in the largest spot, maps with high N_{side} and cuts close to zero (and thus few, but large, spots) were tested only twice. Tests were more comprehensive for large spots on smaller N_{side} maps as well as high N_{side} maps with cuts far away from zero $|c| > 250\mu K$ and the difference was found to be small, but existing, on all except some of the coarsest ($N_{side} \leq 32$) maps where the effect disappeared completely. The effect did not show any bias to make spots appear more or less elliptic or oblique. Although greater than any of the other sources of error examined this effect is is still less than 5% of the calculated statistical errors.

A much easier and less time consuming test is to check for individual spots. The effect is quite common, and although more profound on the intermediate size spots (10–30 pixels) than on the smaller ones (where all pixels are likely to be considered anyway) or larger ones (where the difference, if any, is small), the difference was small enough to be ignored for the ellipticity. For this reason it was decided that no further tests of high N_{side} maps with cuts close to zero was necessary. The obliquity, however, may change quite much, especially for very circular spots. This is a problem, and does not go away except for the smallest spots (for the same reason as above). It was decided to accept this uncertainty as the effect on statistics is not profound, even if a few spots dramatically change their obliquity.

5.1.5 Size of Spots

Testing the program for individual spots turned out to be far more useful than expected. The program is able to find all spots no matter how large, but when calculating the ellipticity and obliquity, it is only able to give a meaningful answer for spots smaller than π in length and whose semi-minor axis have no components further from the main axis than $\pi/2$. This is because the program only calculates the direct great circle distance between two points on the sphere using formulas (4.3) and (4.9) and does not care if that circle follows the spot in any way. Likewise, the calculation for the distance from a pixel down on the major axis will find the shortest path, even if this path placed along a great circle intersecting the major axis twice. This may result in a spot having a larger ellipticity than it would have had pixels along the minor axis be removed. This may be seen more as a problem with the definition of the spots themselves, however, and because there may be at most one such spot in a CMB map its contribution to the statistics for obliquity and ellipticity is negligible.

Another problem with very large spots, even if they are smaller than π in length is that like the cosine formula (4.3) has problems when angles are small, the havesine formula (4.9) will be subject to round off errors whenever the points considered are close to antipodal[45]. In practice, the use of double precision suppresses this error in much the same manner as double presicion floats suppress the round off errors equation (4.3) might experience for small

spots. Again, as this is only the case for very large spots, their numbers will be too small to influence the final statistics.

5.1.6 Beam, Noise and Mask

Maps (both real and simulated) were tested both with and without mask. The results obtained in both cases hardly differed at all (only to the sixth significant digit. Simulated maps were created with all combinations of beam, noise and mask, and the mask seemed again to be of little consequence either way. The noise pushed the ellipticity up a little, the beam smeared out and removed the smaller spots, so that the lower bound ellipticities would be the same as the larger. A few maps were also simulated with $\sqrt{5}$ more noise, to emulate what might have been the case for the first year data, and this produced a more profound effect on the map > 8 pixel map, but not on the > 20 pixel map.

5.2 Discussion

The spots defined in this thesis were the same as was chosen by Gurzadyan et al [1], as was the formula for calculating ellipticity

$$\epsilon = \frac{a}{b} \tag{5.2}$$

for a and b as major and minor axis respectively. The definition of semi–major axis differed to the one presented in [1], where the semi–major axis is found by defining a center and letting the semi–major axis be the line to the center of the spot from the pixel furthest away from that center. It could be that the difference in results obtained stem from this, although what mathematical mechanism could be causing this is not known.

Foregrounds were not considered, and confidence was placed on the mask. The mask used (KQ85) is fairly liberal (i.e. removing less than a more conservative mask), and may create problems especially in the Q band; if so, the effect is small enough not to be detectable.

Besides being unknown what problems the random number generator used might present (see section 3.6.1) only one mask (KQ85) was used and only one weight function to simulate maps. This could potentially limit the value of the analysis conducted for this thesis, and introduces several uncontrolled sources of error. Also, the "nasty dogs" (section 3.4.3) were not taken into account. The effect of such systematic effects are unknown, but assumed to be small.

The analysis for [4] was performed on the first year data which, in worst case, should be considered to have a signal–to–noise fraction $\sqrt{5}$ times less than the five year data. They performed their analysis on maps A and B

created as

$$A = \frac{W_1 + W_2}{2} \tag{5.3}$$

and

$$B = \frac{W_3 + W_4}{2} \tag{5.4}$$

where W_1 is the first W band assembly, W_2 is the second and so on. They use the A+B map (assumed to mean $(A+B)/2$) for analysis, and A-B map to investigate noise. As long as the noise is Gaussian all maps W_i

$$W_i = W + n_i \tag{5.5}$$

where W is the true value for the W band and n_i is the Gaussian and zero–centered noise, taking

$$\frac{A-B}{2} = \frac{1}{2}\left(\frac{W + n_1 + n_2}{2} - \frac{W + n_3 + n_4}{2}\right) = \frac{n_1 + n_2 - n_3 - n_4}{4} \tag{5.6}$$

is equivalent to taking

$$\frac{n_1 + n_2 + n_3 + n_4}{4}. \tag{5.7}$$

If there is substantial non–white noise, however, it will not be an equivalent operation. This could then lead to errors in estimating noise for the data.

The obliquity reported in [1, 2, 3, 4] range from 0 to 180°. They do not properly explain what definition they use for obliquity, but the most common definition (and the one assumed for this thesis) is only defined for angles $[0, \pi/2]$. This is because there is no meaning in defining "up" or "down" on a spot, and hence the great circle traced by the major axis can never be more than perpendicular to the chosen equator. Likely, this error is a mistake from defining the semi–major axis as a given orientation compared to the defined center[3]. If one assume that they with "obliquity" refer to what is the standard definition from celestial mechanics, there is almost agreement between the non–detection of a preferred direction and the work performed for this thesis.

5.3 Conclusion

Gurzadyan et al has, in several papers, claimed that there is strong evidence for an abnormally high ellipticity in the CMB as measured both by BOOMERanG and WMAP and to a certain extent also COBE [1, 2, 3, 4].

[3]Why not up to 360° then?

The WMAP five year data was examined in the Q, V, W and combined VW band maps to look for such an effect. No extraordinary ellipticity was found, and the results obtained for this thesis also disagrees with the reported substantial difference in ellipticity for spots greater than 50 pixels compared to when spots of 20 to 50 pixels also are included. Only for the smallest spots are any such difference found. In the case of this thesis; this is probably due to noise; and agrees well with measures on simulated noise–only maps, but findings does not support the notion that a similar effect can explain the differences in ellipticity for the > 20 pixel group compared to the > 50 pixel group.

[1, 2, 3, 4] also reports that no preferred direction can be found to any statistical significance on the CMB spots. Work preformed for this thesis also conclude that no such direction can be found to within a satisfactory statistical confidence. There is, however, a difference in average obliquity when comparing to different equator rings on the sphere. This difference seem to suggest slightly that there is a preferred direction on the spots and that they align perpendicular to an axis close to one found by [47] for anisotropies in the CMB. They also, however, align close to the noise axis. The lack of conclusive detection and proper posterior estimation means no detection claim can be made at this time.

Gurzadyan et al interpret the claimed ellipticity as evidence for geodesics mixing in a hyperbolic universe [3]. This is contrary to reports suggesting that the universe is flat; first from BOOMERanG [48], then from WMAP data [49, 50] (with the latter reporting $-0.0179 < \Omega_k < 0.0089$ to 95% confidence). Not detecting any abnormal ellipticity is consistent with the reported flatness of the universe and fits neatly within the cosmological standard model. This holds true for all frequency maps considered.

5.4 Future Work

In general, more is almost always better. The analysis should be performed with more varied masks. It should also be possible to show to a given confidence the likelihood that spots are indeed as elliptic as they are now—given the fact that simulated values were within confidence intervals, this step was omitted.

The analysis performed for this thesis was, even though similar, not exactly the same as the one described in [1]. The possibility that all differences stem from the difference in defining semi–major axis should be investigated.

The ellipticity measures were not very encouraging. The negative find should still be confirmed by comparing different areas against each other, such as hemispheres, bands of different orientation, width and latitude and smaller patches on different places in the sky. By using for instance the $N_{side} = 1$ pixels as patches, it is possible to measure correlation in the

ellipticity between different patches in the sky.

Also, it is possible to consider a "higher order ellipticity"; i.e. calculating the spot total distortion (that is, deviation from a circle). This may, for instance, be done by least–distance–mapping [51], made easier by considering the space Euclidean [52]. Another estimate of the higher–order ellongation is the Kolmogorov complexity and such estimates have already been made by Gurzadyan & Kocharyan [53]. Further, it should be possible to take into account the steepness of peaks rather than just the linear cut on one arbitrarily chosen temperature, including the second and third spacial derivative [54]. A simpler approach would be to consider the spot as a 2D distribution by taking its values into account, and use the 2D skewness as a measure of ellipticity. Also, wavelet localization of spots, abandoned for this thesis, could nevertheless show if some patches of sky have more elliptic anisotropies than others and if the more/less elliptic spots would tend to cluster — the analysis performed here only superficially takes this into account.

The obliquity measures were slightly more encouraging. The erroneous confidence intervals should be compensated for by adding weights to spots as e.g. $1 - sin(\theta)$ where θ is defined as the center of the spot, or by using only spots close to the considered equator. Another option will be to attempt a rescale of spot obliquity, mapping the possible intervals at a given θ to the uniform (in the Gaussian no–effect case) distribution one has on the equator; perhaps in combination with weighting. It should be estimated with a proper prior and null hypothesis, likelihoods for such an axis should be computed and the confidence intervals should be treated properly.

Finally, as Planck will be releasing its data, redoing the analysis on the higher resolution maps will determine the extent of pixel effects and noise in the heightened ellipticity for the smallest spots. Probing smaller scales will not only increase the statistics overall, but make it possible to compare ellipticity of large spots to small ones given the increased sensitivity. Ellipticity measure as performed for this thesis is computationally inexpensive compared to most other forms of CMB analysis and may provide data on geodesic mixing and curvature as well as might prove a valuable tool in determining the topology of the universe[4]. In addition, it might be, with more finely tuned statistics, possible to determine if the obliquity measured indeed shows a preferred direction.

[4]Even with a ΛCDM universe model the number of topologies fitting a given ellipticity measure is infinite [4].

Appendix A

Cosmological Parameters

Parameter	Common symbol
Baryon density, $\Omega_b h^2$	ω_b
Cold dark matter density, $\Omega_{CDM} h^2$	ω_{CDM}
Dark energy density, with $w = -1$ unless stated	Ω_Λ
Amplitude of curvature perturbations at $k_0 = 0.002$/Mpc	Δ_R^2
Scalar spectral index at $k_0 = 0.002$/Mpc	n_{sp}
Reionization optical depth	τ
SZ marginalization factor	A_{SZ}
Running in scalar spectral index	$dn_{sp}/d\ln k$
Ratio of the amplitude of tensor fluctuations to scalar fluctuations	r
Fraction of anti-correlated CDM isocurvature	α_{-1}
Fraction of uncorrelated CDM isocurvature	α_0
Effective number of relativistic species (assumed neutrinos)	N_{eff}
Massive neutrino density, $\Omega_\nu h^2$	ω_ν
Spatial curvature, $1 - \Omega_{tot}$	Ω_k
Dark energy equation of state, $w = p_{DE}/\rho_{DE}$	w
Primordial Helium fraction	Y_P
Ionization fraction of first step in two-step reionization	x_e
Reionization redshift of first step in two-step reionization	z_r
Linear theory amplitude of matter fluctuations on $8h^{-1}$ Mpc scales	σ_8
Hubble expansion factor ($100h$Mpc^{-1}km s^{-1})	H_0
Total neutrino mass (eV) $\sum m_\nu = 94\Omega_\nu h^2$	$\sum m_\nu$
Matter energy density ($\Omega_b + \omega_{CDM} + \Omega_\nu$)	Ω_m
Matter energy density	$\Omega_b h^2$
Age of the universe (billions of years)	t_0
Redshift of instantaneous reionization	z_{reion}
Ratio of baryon to photon number densities, $10^{10}(n_b/n_\gamma) = 273.9\Omega_b h^2$	η_{10}

Table A.1: Some cosmological parameters with common symbols.

WMAP Cosmological Parameters Model: lcdm+sz+lens Data: wmap5			
$10^2\Omega_b h^2$	2.273 ± 0.062	$1 - n_s$	$0.037^{+0.015}_{-0.014}$
$1 - n_s$	$0.0081 < 1 - n_s < 0.0647$ (95% CL)	$A_{\rm BAO}(z = 0.35)$	0.457 ± 0.022
C_{220}	5756 ± 42	$d_A(z_{\rm eq})$	14279^{+186}_{-189} Mpc
$d_A(z_*)$	14115^{+188}_{-191} Mpc	$\Delta^2_{\mathcal{R}}$	$(2.41 \pm 0.11) \times 10^{-9}$
h	$0.719^{+0.026}_{-0.027}$	H_0	$71.9^{+2.6}_{-2.7}$ km/s/Mpc
$k_{\rm eq}$	0.00968 ± 0.00046	$\ell_{\rm eq}$	136.6 ± 4.8
ℓ_*	$302.08^{+0.83}_{-0.84}$	n_s	$0.963^{+0.014}_{-0.015}$
Ω_b	0.0441 ± 0.0030	$\Omega_b h^2$	0.02273 ± 0.00062
Ω_c	0.214 ± 0.027	$\Omega_c h^2$	0.1099 ± 0.0062
Ω_Λ	0.742 ± 0.030	Ω_m	0.258 ± 0.030
$\Omega_m h^2$	0.1326 ± 0.0063	$r_{\rm hor}(z_{\rm dec})$	286.0 ± 3.4 Mpc
$r_s(z_d)$	153.3 ± 2.0 Mpc	$r_s(z_d)/D_v(z = 0.2)$	0.1946 ± 0.0079
$r_s(z_d)/D_v(z = 0.35)$	0.1165 ± 0.0042	$r_s(z_*)$	146.8 ± 1.8 Mpc
R	1.713 ± 0.020	σ_8	0.796 ± 0.036
$A_{\rm SZ}$	$1.04^{+0.96}_{-0.69}$	t_0	13.69 ± 0.13 Gyr
τ	0.087 ± 0.017	θ_*	0.010400 ± 0.000029
θ_*	0.5959 ± 0.0017 °	t_*	380081^{+5843}_{-5841} yr
$z_{\rm dec}$	1087.9 ± 1.2	z_d	1020.5 ± 1.6
$z_{\rm eq}$	3176^{+151}_{-150}	$z_{\rm reion}$	11.0 ± 1.4
z_*	1090.51 ± 0.95		

Figure A.1: Best fit values from the WMAP 5 year data and assume the ΛCDM model including Sunyaev-Zel'dovich effect and gravitational lensing. Values courtesy of the WMAP team.

Appendix B

Mathematical Preliminaries

B.1 Einstein Notation

In the parts concerning general relativity, Einsteins summation conveintion will be used. The idea is that the components of vectors are represented by a subscript or a superscript such that

$$x_i = \begin{pmatrix} x_1 & x_2 & x_3 \end{pmatrix}. \tag{B.1}$$

is a covariant vector and

$$x^i = \begin{pmatrix} x^1 \\ x^2 \\ x^3 \end{pmatrix} \tag{B.2}$$

is a contravariant vector. Also, the convension will be adopted that latin indexes represent the three values of 3-space and Greek indexes represent the four values of 4-space with time being the additional (zeroth) component such that

$$x_\mu = \begin{pmatrix} x_0 & x_1 & x_2 & x_3 \end{pmatrix} \tag{B.3}$$

Likewise a tensor of higher rank, such as a matrix is represented by additional indexes such that

$$A_{\mu\nu} = \begin{pmatrix} a_{00} & a_{01} & a_{02} & a_{03} \\ a_{10} & a_{11} & a_{12} & a_{13} \\ a_{20} & a_{21} & a_{22} & a_{23} \\ a_{30} & a_{31} & a_{32} & a_{33} \end{pmatrix} \tag{B.4}$$

is a covariant matrix and $A^{\mu\nu}$ is a contravariant matrix:

$$A^{\mu\nu} = \begin{pmatrix} a_{00}^{-1} & a_{10}^{-1} & a_{02} & a_{03} \\ a_{01}^{-1} & a_{11} & a_{12} & a_{13} \\ a_{20} & a_{21} & a_{22} & a_{23} \\ a_{30} & a_{31} & a_{32} & a_{33} \end{pmatrix} \tag{B.5}$$

where the components a_{ij} are the same in equations (B.4) and (B.5). Matrices $A_\mu{}^\nu$ and $A^\nu{}_\mu$ each have a covariant and a contravariant index. Higher rank tensors are possible by adding additional indexes.

B.1.1 Summation

Whenever the same index is repeated both as a superscript and subscript in a multiplicative expression the convention will be adopted that such repeated indexes are summed over. For instance

$$x^i y_i = \sum_{i=1}^{3} x^i y_i = x^1 y_1 + x^2 y_2 + x^3 y_3 \tag{B.6}$$

and

$$x^\mu y_\mu = \sum_{\mu=0}^{3} x^\mu y_\mu \tag{B.7}$$

and

$$A^\mu{}_\nu x^\nu = y^\mu, \tag{B.8}$$

but

$$x^i y^i \neq \sum_{i=1}^{3} x^i y^i. \tag{B.9}$$

The length of a 4-vector y, placed in the point y in space-time is

$$y^2 = g_{\mu\nu}(x) y^\mu y^\nu = y_\nu y^\nu \tag{B.10}$$

where $g_{\mu\nu}$ is used to lower an index as described bellow (section B.1.2). Likewise; the scalar product between two 4-vectors y and z at point x in space-time is

$$yz = g_{\mu\nu}(x) y^\mu z^\nu = y_\nu z^\nu. \tag{B.11}$$

B.1.2 Raising and Lowering Indexes

To evaluate a mixed tensor, compute a covariant tensor from a contravariant and vice-versa or evaluate a self summing tensor, the product of , the following identity is important.

$$g_{\mu\nu} x^\mu = x_\nu. \tag{B.12}$$

This can be generalized:

$$g_{\mu\nu} T^{\alpha\nu} = T^\alpha{}_\mu \tag{B.13}$$

and

$$g^{\mu\nu}T^{\alpha\nu} = T_{\alpha}{}^{\mu}. \tag{B.14}$$

Note that

$$g_{\mu\nu}g^{\nu\alpha} = \delta^{\alpha}{}_{\mu} \tag{B.15}$$

where $\delta^{\alpha}{}_{\mu}$ is the mixed-tensor variant of the *Kronecker delta*, defined as

$$\delta^{\alpha}{}_{\mu} = \delta_{\alpha}{}^{\mu} = \delta^{\alpha\mu} = \delta_{\alpha\mu} \equiv \begin{cases} 1, & \text{if } \alpha = \mu \\ 0, & \text{if } \alpha \neq \mu \end{cases} \tag{B.16}$$

B.1.3 Derivatives

The Einstein notation convention will be adopted that a comma refers to a derivative of an x with subscript or superscript what comes after the comma. For example

$$\Gamma^{\alpha}{}_{\mu\nu,\alpha} \equiv \frac{\partial \Gamma^{\alpha}{}_{\mu\nu}}{\partial x^{\alpha}}. \tag{B.17}$$

In equation (B.17) the α is a repeated index and thus is also summed over as described in subsection B.1.1.

B.2 Spherical Trigonometry: Law of Haversines

The *versine* for an angle θ is defined as

$$\mathrm{vers}(\theta) \equiv 1 - \cos(\theta) = 2\sin^2\left(\frac{\theta}{2}\right). \tag{B.18}$$

The *haversine* is half the versine;

$$\mathrm{hav}(\theta) \equiv \frac{\mathrm{vers}(\theta)}{2} = \frac{1-\cos(\theta)}{2} = \sin^2\left(\frac{\theta}{2}\right). \tag{B.19}$$

The latter identity is why the haversine is attractive in the first place; for small angles the sine becomes small, and all significant digits are kept. Contrast this against the cosine which, being very close to one for small angles, loose many significant digits as leading nines after zero.

To derive the haversine formula for the angle Λ between two points A and B on a sphere with $A = (\theta_A, \phi_A)$ and $B = (\theta_B, \phi_B)$, consider two more points, C and D with $C = (\theta_B, \phi_A)$ and $D = (\theta_A, \phi_B)$. In general, the chord between two points P_1 and P_2 on a sphere separated by an angle ψ is

$$P_1P_2 = 2\sin\left(\frac{\psi}{2}\right) \tag{B.20}$$

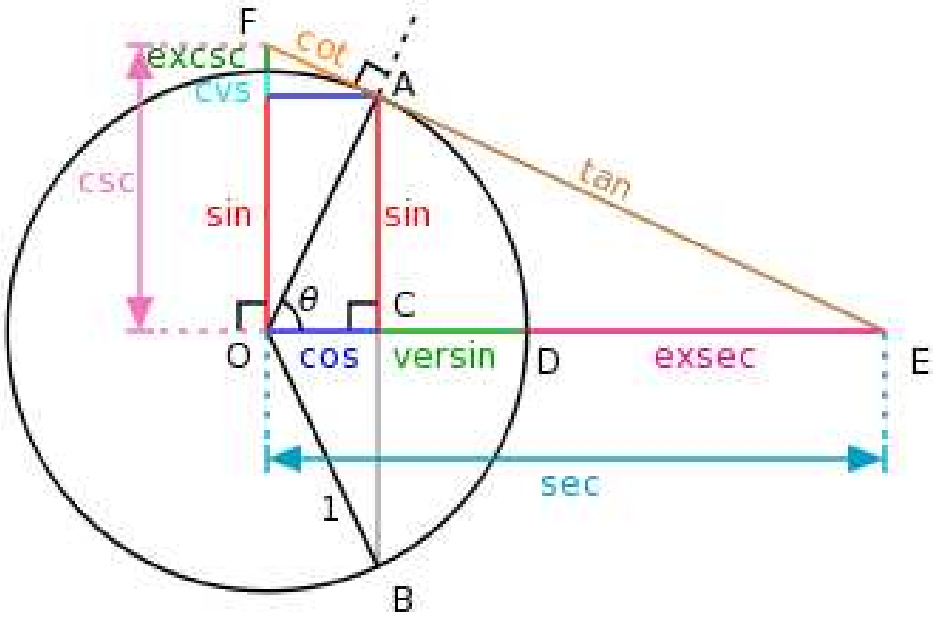

Figure B.1: Unit circle showing all trigonometric functios. The versine lies on the x axis, and measures the distance $1-\cos(\theta)$(From Wikimedia Commons)

so the chord

$$AC = 2\sin\left(\frac{\theta_A - \theta_B}{2}\right) \tag{B.21}$$

and the chord $BD = AC$. Points A and D are circle constant on a circle with radius $cos(\theta_A)$; similarly points B and C are circle constant on a circle with radius $cos(\theta_B)$. In a similar fashion to equation (B.21)

$$AD = 2\sin\left(\frac{\phi_A - \phi_B}{2}\right)\sin(\theta_A) \tag{B.22}$$

and

$$BC = 2\sin\left(\frac{\phi_A - \phi_B}{2}\right)\sin(\theta_B) \tag{B.23}$$

If all four chords are drawn, the resulting figure is an isosceles trapezoid, which, in particular, has the property of being symmetric about the middle θ angle.

If a chord between A and B could be found, equation (B.20) would give the angle between them. To find such a chord, assume first that BC is longer than AD. In that case, define a point E on the line BC, so that the line AE

is perpendicular to the line BC. Because of symmetry, the distance

$$AE = \frac{(BC - AD)}{2}. \tag{B.24}$$

Using Pythagoras theorem

$$(AE)^2 = (AC)^2 - (CH)^2 = (AC)^2 - \frac{(CB - AD)^2}{4}. \tag{B.25}$$

The length of BE is

$$BE = \frac{CB + AD}{2} \tag{B.26}$$

which, if Pythagoras' is used again, results in

$$\begin{aligned} (AB)^2 &= (AE)^2 + (EB)^2 \\ &= (AC)^2 - \frac{(CB - AD)^2}{4} + \frac{(CB + AD)^2}{4} \\ &= (AC)^2 + CB \cdot AD. \end{aligned} \tag{B.27}$$

Putting in the length of the chords

$$(AB)^2 = 4\left(\sin^2\left(\frac{\theta_A - \theta_B}{2}\right) + \sin(\theta_A)\sin(\theta_B)\sin^2\left(\frac{\phi_A - \phi_B}{2}\right)\right). \tag{B.28}$$

If a half the length AB, then

$$\begin{aligned} a^2 &= \left(\frac{AB}{2}\right)^2 \\ &= \left(\sin^2\left(\frac{\theta_A - \theta_B}{2}\right) + \sin(\theta_A)\sin(\theta_B)\sin^2\left(\frac{\phi_A - \phi_B}{2}\right)\right), \end{aligned} \tag{B.29}$$

and form (B.20)

$$\sin\left(\frac{\Lambda}{2}\right) = a \tag{B.30}$$

or

$$\sin^2\left(\frac{\Lambda}{2}\right) = \mathrm{hav}(\Lambda) = a^2. \tag{B.31}$$

Rewriting a in terms of haversines, leaves us with

$$\mathrm{hav}(\Lambda) = \mathrm{hav}(\theta_A - \theta_B) + \sin(\theta_A)\sin(\theta_B)\mathrm{hav}(\phi_A - \phi_B) \tag{B.32}$$

which is the law of haversines.

This derivation assumed that BC is longer than AD. Fortunately, nothing binds the labels on the points, so that if the opposite was true, simply switch the labels A with B and C with D, the derivation still holds.

B.3 Some Topology

B.3.1 Simple Connectedness

Let X be a space and let $f\,[0,1] \to X$ where $f(0) = x$ and $f(1) = y$ for points $x, y \in X$ be a continuous function. The space X is path connected if such a function exists for all points x and y in X. This means that a continuous path may be drawn between every two points in the space X.

The space X is simply connected iff it is path connected and every path between two points in X may be continuously transformed into every other path between those two points.

Equivalently, it holds true when those two points are merged, so that the space X is simply connected iff it is path connected and every path starting and ending in a point A may be continuously transformed into every other path starting and ending in A [55]. This implies that no "holes" exist for which it is impossible to wine a path around in a physical 3–space.

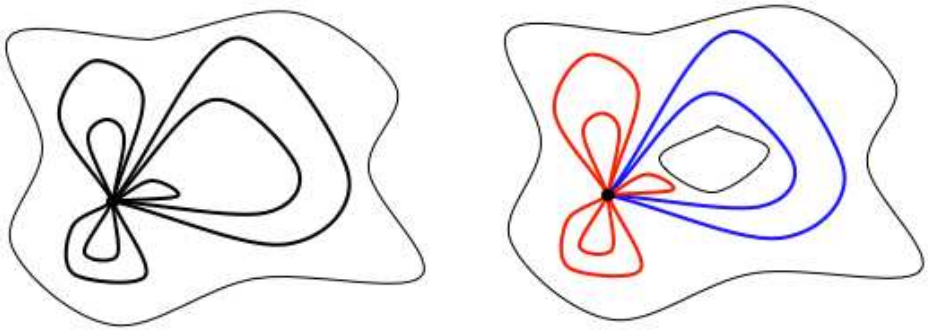

Figure B.2: Two topological spaces. The left is simply connected; the path from the point may be continuously transformed into every other. The one on the right is not; not all paths are path-homotopic; ie. not all can be continuously transformed into the other.

Bibliography

[1] V. G. Gurzadyan, P. A. R. Ade, P. de Bernardis, C. L. Bianco, J. J. Bock, A. Boscaleri, B. P. Crill, G. de Troia, K. Ganga, M. Giacometti, E. Hivon, V. V. Hristov, A. L. Kashin, A. E. Lange, S. Masi, P. D. Mauskopf, T. Montroy, P. Natoli, C. B. Netterfield, E. Pascale, F. Piacentini, G. Polenta, and J. Ruhl. Ellipticity Analysis of the BOOMERanG CMB Maps. *International Journal of Modern Physics D*, 12:1859–1873, 2003.

[2] V. G. Gurzadyan, P. A. R. Ade, P. de Bernardis, C. L. Bianco, J. J. Bock, A. Boscaleri, B. P. Crill, G. de Troia, E. Hivon, V. V. Hristov, A. L. Kashin, H. Kuloghlian, A. E. Lange, S. Masi, P. D. Mauskopf, T. Montroy, P. Natoli, C. B. Netterfield, E. Pascale, F. Piacentini, G. Polenta, J. Ruhl, and G. Yegorian. WMAP confirming the ellipticity in BOOMERanG and COBE CMB maps. *Nuovo Cimento B Serie*, 118:1101–+, October 2003.

[3] V. G. Gurzadyan, P. de Bernardis, G. De Troia, C. L. Bianco, A. L. Kashin, H. Kuloghlian, S. Masi, F. Piacentini, G. Polenta, and G. Yegorian. Elliptic cmb sky. *MOD.PHYS.LETT.A*, 20:813, 2005.

[4] V. G. Gurzadyan, P. A. R. Ade, P. de Bernardis, C. L. Bianco, J. J. Bock, A. Boscaleri, B. P. Crill, G. de Troia, E. Hivon, V. V. Hristov, A. L. Kashin, H. Kuloghlian, S. Masi, P. D. Mauskopf, T. Montroy, P. Natoli, E. Pascale, F. Piacentini, G. Polenta, and G. Yegorian. Ellipticity of Large Spots in CMB Anisotropy Maps. *Modern Physics Letters A*, 20:491–498, 2005.

[5] G. F. Smoot, C. L. Bennett, A. Kogut, E. L. Wright, J. Aymon, N. W. Boggess, E. S. Cheng, G. de Amici, S. Gulkis, M. G. Hauser, G. Hinshaw, P. D. Jackson, M. Janssen, E. Kaita, T. Kelsall, P. Keegstra, C. Lineweaver, K. Loewenstein, P. Lubin, J. Mather, S. S. Meyer, S. H. Moseley, T. Murdock, L. Rokke, R. F. Silverberg, L. Tenorio, R. Weiss, and D. T. Wilkinson. Structure in the COBE differential microwave radiometer first-year maps. *Astrophysical Journal Letters*, 396:L1–L5, September 1992.

[6] P. de Bernardis, P. A. R. Ade, J. J. Bock, J. R. Bond, J. Borrill, A. Boscaleri, K. Coble, C. R. Contaldi, B. P. Crill, G. De Troia, P. Farese, K. Ganga, M. Giacometti, E. Hivon, V. V. Hristov, A. Iacoangeli, A. H. Jaffe, W. C. Jones, A. E. Lange, L. Martinis, S. Masi, P. Mason, P. D. Mauskopf, A. Melchiorri, T. Montroy, C. B. Netterfield, E. Pascale, F. Piacentini, D. Pogosyan, G. Polenta, F. Pongetti, S. Prunet, G. Romeo, J. E. Ruhl, and F. Scaramuzzi. Multiple Peaks in the Angular Power Spectrum of the Cosmic Microwave Background: Significance and Consequences for Cosmology. *Astrophysical Journal*, 564:559–566, January 2002.

[7] N. W. Halverson, E. M. Leitch, C. Pryke, J. Kovac, J. E. Carlstrom, W. L. Holzapfel, M. Dragovan, J. K. Cartwright, B. S. Mason, S. Padin, T. J. Pearson, A. C. S. Readhead, and M. C. Shepherd. Degree Angular Scale Interferometer First Results: A Measurement of the Cosmic Microwave Background Angular Power Spectrum. *Astrophysical Journal*, 568:38–45, March 2002.

[8] A. T. Lee, P. Ade, A. Balbi, J. Bock, J. Borrill, A. Boscaleri, P. de Bernardis, P. G. Ferreira, S. Hanany, V. V. Hristov, A. H. Jaffe, P. D. Mauskopf, C. B. Netterfield, E. Pascale, B. Rabii, P. L. Richards, G. F. Smoot, R. Stompor, C. D. Winant, and J. H. P. Wu. A High Spatial Resolution Analysis of the MAXIMA-1 Cosmic Microwave Background Anisotropy Data. *Astrophysical Journal Letters*, 561:L1–L5, November 2001.

[9] C. L. Bennett, M. Halpern, G. Hinshaw, N. Jarosik, A. Kogut, M. Limon, S. S. Meyer, L. Page, D. N. Spergel, G. S. Tucker, E. Wollack, E. L. Wright, C. Barnes, M. R. Greason, R. S. Hill, E. Komatsu, M. R. Nolta, N. Odegard, H. V. Peirs, L. Verde, and J. L. Weiland. First year wilkinson microwave anisotropy probe (wmap) observations: Preliminary maps and basic results. *The Astrophysical Journal*, 148:1, 2003.

[10] Scott Dodelson. *Modern Cosmology*. Academic Press, Elsevier, 2003.

[11] Barbara Ryden. *Introduction to Cosmology*. Benjamin Cummings, October 2002.

[12] Øyvind Grøn and Sigbjørn Hervik. *Einstein's General Theory of Relativity With Modern Applications in Cosmology*. Springer Science+Business Media, LLC, 2007.

[13] A. Friedmann. Über die möglichkeit einer welt mit konstanter negativer krümmung des raumes. *Zeitschrift für Physik A Hadrons and Nuclei*, 21(1):326–332, December 1924. Publisher: Springer Berlin / Heidelberg.

[14] G. Lemaître. Expansion of the universe, A homogeneous universe of constant mass and increasing radius accounting for the radial velocity of extra-galactic nebulae. *Monthly Notices of the Royal Astronomical Scociety*, 91:483–490, March 1931.

[15] H. P. Robertson. Kinematics and World-Structure. *Astrophysical Journal*, 82:284–+, November 1935.

[16] A. G. Walker. On Milne's Theory of World-Structure. *Proc. London Math. Soc.*, s2-42:90–127, 1937.

[17] Daniel Schroeder. An introduction to thermal physics, August 2005.

[18] N. Banerjee and S. Sen. Einstein pseudotensor and total energy of the universe. *Pramana*, 49:609–615, December 1997.

[19] Yun Wang and Pia Mukherjee. Observational constraints on dark energy and cosmic curvature. *Physical Review D*, 76:103533, 2007.

[20] Howard Baer and Xerxes Tata. Dark matter and the lhc, 2008.

[21] P. M. Garnavich, R. P. Kirshner, P. Challis, J. Tonry, R. L. Gilliland, R. C. Smith, A. Clocchiatti, A. Diercks, A. V. Filippenko, M. Hamuy, C. J. Hogan, B. Leibundgut, M. M. Phillips, D. Reiss, A. G. Riess, B. P. Schmidt, J. Spyromilio, C. Stubbs, N. B. Suntzeff, and L. Wells. Constraints on cosmological models from hubble space telescope observations of high-z supernovae. *The Astrophysical Journal*, 493:L53, 1998.

[22] S. Perlmutter, G. Aldering, G. Goldhaber, R. A. Knop, P. Nugent, P. G. Castro, S. Deustua, S. Fabbro, A. Goobar, D. E. Groom, I. M. Hook, A. G. Kim, M. Y. Kim, J. C. Lee, N. J. Nunes, R. Pain, C. R. Pennypacker, R. Quimby, C. Lidman, R. S. Ellis, M. Irwin, R. G. McMahon, P. Ruiz-Lapuente, N. Walton, B. Schaefer, B. J. Boyle, A. V. Filippenko, T. Matheson, A. S. Fruchter, N. Panagia, H. J. M. Newberg, and W. J. Couch. Measurements of omega and lambda from 42 high-redshift supernovae, 1999.

[23] Alessandra Silvestri and Mark Trodden. Approaches to understanding cosmic acceleration, 2009.

[24] E. Hubble. A Relation between Distance and Radial Velocity among Extra-Galactic Nebulae. *Proceedings of the National Academy of Science*, 15:168–173, March 1929.

[25] Lyman Page. The map satellite mission to map the cmb anisotropy, 2000.

[26] G. Hinshaw, M. R. Nolta, C. L. Bennett, R. Bean, O. Dore, M. R. Greason, M. Halpern, R. S. Hill, N. Jarosik, A. Kogut, E. Komatsu, M. Limon, N. Odegard, S. S. Meyer, L. Page, H. V. Peiris, D. N. Spergel, G. S. Tucker, L. Verde, J. L. Weiland, E. Wollack, and E. L. Wright. Three-year wilkinson microwave anisotropy probe (wmap) observations: Temperature analysis. *The Astrophysical Journal*, 170:288, 2007.

[27] G. Hinshaw, J. L. Weiland, R. S. Hill, N. Odegard, D. Larson, C. L. Bennett, J. Dunkley, B. Gold, M. R. Greason, N. Jarosik, E. Komatsu, M. R. Nolta, L. Page, D. N. Spergel, E. Wollack, M. Halpern, A. Kogut, M. Limon, S. S. Meyer, G. S. Tucker, and E. L. Wright. Five-year wilkinson microwave anisotropy probe (wmap) observations: Data processing, sky maps, and basic results. *The Astrophysical Journal*, 180:225, 2009.

[28] Max Tegmark, Daniel J. Eisenstein, Wayne Hu, , and Angelica de Oliveira-Costa. Foregrounds and forecasts for the cosmic microwave background. *The Astrophysical Journal*, 530(1):133–165, 2000.

[29] A. de Oliveira-Costa and M. Tegmark. CMB multipole measurements in the presence of foregrounds. *Physical Review D*, 74(2):023005–+, July 2006.

[30] N. Jarosik et al. Design, Implementation and Testing of the MAP Radiometers. *The Astrophysical Journal Supplement Series*, 2003.

[31] M. Limon, E. Wollack, M. R. Greason, C. L. Bennett, M. Halpern, G. Hinshaw, N. Jarosik, A. Kogut, S. S. Meyer, L. Page, D. N. Spergel, G. S. Tucker, E. L. Wright, R. S. Hill, E. Komatsu, M. Nolta, N. Odegard, and J. L. Weiland. Wilkinson microwave anisotropy probe (*wmap*): Five year explanatory supplement. `http://lambda.gsfc.nasa.gov/data/map/doc/MAP_supplement.pdf`, 2008.

[32] L. Page, C. Barnes, G. Hinshaw, D. N. Spergel, J. L. Weiland, E. Wollack, C. L. Bennett, M. Halpern, N. Jarosik, A. Kogut, M. Limon, S. S. Meyer, G. S. Tucker, and E. L. Wright. First Year Wilkinson Microwave Anisotropy Probe (WMAP) Observations: Beam Profiles and Window Functions. *Astrophys. J. Suppl.*, 148:39, 2003.

[33] R. S. Hill et al. Five-Year Wilkinson Microwave Anisotropy Probe (WMAP) Observations: Beam Maps and Window Functions. *Astrophys. J. Suppl.*, 180:246–264, 2009.

[34] Ingunn Kathrine Wehus, Lotty Ackerman, H. K. Eriksen, and Nicolaas E. Groeneboom. The effect of asymmetric beams in the Wilkinson Microwave Anisotropy Probe experiment, 2009.

[35] N. E. Groeneboom, H. K. Eriksen, K. Gorski, G. Huey, J. Jewell, and B. Wandelt. Bayesian analysis of white noise levels in the 5-year WMAP data. *ArXiv e-prints*, April 2009.

[36] M. A. J. Ashdown, C. Baccigalupi, J. G. Bartlett, J. Borrill, C. Cantalupo, G. De Gasperis, G. De Troia, K. M. Gorski, E. Hivon, K. Huffenberger, E. Keihanen, R. Keskitalo, T. Kisner, H. Kurki-Suonio, C. R. Lawrence, P. Natoli, T. Poutanen, G. Prezeau, M. Reinecke, G. Rocha, M. Sandri, R. Stompor, F. Villa, and B. Wandelt. Making maps from planck lfi 30ghz data with asymmetric beams and cooler noise. *ASTRON.ASTROPHYS.*, 493:753, 2009.

[37] Krzysztof M. Gorski, Benjamin D. Wandelt, Frode K. Hansen, Eric Hivon, and Anthony J. Banday. The healpix primer, 1999.

[38] Benjamin D. Wandelt, Eric Hivon, and Kris M. Gorski. Topological analysis of high-resolution cmb maps, 1998.

[39] Max Tegmark, Angélica de Oliveira-Costa, and Andrew J. S. Hamilton. High resolution foreground cleaned cmb map from wmap. *Phys. Rev. D*, 68(12):123523, Dec 2003.

[40] George Marsaglia. Xorshift rngs. *Journal of Statistical Software*, 8(14):1–6, 7 2003.

[41] François Panneton and Pierre L'ecuyer. On the xorshift random number generators. *ACM Trans. Model. Comput. Simul.*, 15(4):346–361, 2005.

[42] T. Risbo. Fourier transform summation of legendre series and d-functions. *Journal of Geodesy*, Volume 70:383 – 396, April 1996.

[43] Shan-Tao Lai, P. Palting, and Ying-Nan Chiu. On the closed form of wigner rotation matrix elements. *Journal of Mathematical Chemistry*, Volume 19:131–145, June 1996.

[44] Donald E. Knuth. *The art of computer programming, volume 3: (2nd ed.) sorting and searching*. Addison Wesley Longman Publishing Co., Inc., Redwood City, CA, USA, 1998.

[45] R. W. Sinnott. "virtues of the haversine". *Sky and Telescope*, 68:158–+, December 1984.

[46] Antony Lewis. Cosmological parameters from WMAP 5-year temperature maps. *Physical Review D*, 78:023002, 2008.

[47] N. E. Groeneboom and H. K. Eriksen. Bayesian Analysis of Sparse Anisotropic Universe Models and Application to the Five-Year WMAP Data. *Astrophysical Journal*, 690:1807–1819, January 2009.

[48] P. De Bernardis, P. A. R. Ade, J. J. Bock, J. R. Bond, J. Borrill, A. Boscaleri, K. Coble, B.P. Crill, G. De Gasperis, P.C. Farese, P.G. Ferreira, K. Ganga, M. Giacometti, and E. Hivon. A Flat Universe from High-Resolution Maps of the Cosmic Microwave Background Radiation. *Nature*, 404:69–81, 2000.

[49] D. N. Spergel, R. Bean, O. Doré, M. R. Nolta, C. L. Bennett, J. Dunkley, G. Hinshaw, N. Jarosik, E. Komatsu, L. Page, H. V. Peiris, L. Verde, M. Halpern, R. S. Hill, A. Kogut, M. Limon, S. S. Meyer, N. Odegard, G. S. Tucker, J. L. Weiland, E. Wollack, and E. L. Wright. Three-Year Wilkinson Microwave Anisotropy Probe (WMAP) Observations: Implications for Cosmology. *The Astrophysical Journal Supplement Series*, 170:377–408, June 2007.

[50] E. Komatsu, J. Dunkley, M. R. Nolta, C. L. Bennett, B. Gold, G. Hinshaw, N. Jarosik, D. Larson, M. Limon, L. Page, D. N. Spergel, M. Halpern, R. S. Hill, A. Kogut, S. S. Meyer, G. S. Tucker, J. L. Weiland, E. Wollack, and E. L. Wright. Five-Year Wilkinson Microwave Anisotropy Probe Observations: Cosmological Interpretation. *The Astrophysical Journal Supplement Series*, 180:330–376, February 2009.

[51] Wei-Yue Ding. Locally minimizing harmonic maps from noncompact manifolds. *Manuscripta Mathematica*, 85(1):283–297, Dec 1994.

[52] Ricardo Fabbri, Luciano Da F. Costa, Julio C. Torelli, and Odemir M. Bruno. 2d euclidean distance transform algorithms: A comparative survey. *ACM Comput. Surv.*, 40(1):1–44, 2008.

[53] V. G. Gurzadyan and A. A. Kocharyan. Kolmogorov stochasticity parameter measuring the randomness in the cosmic microwave background. *Astronomy and Astrophysics*, 492:L33–L34, December 2008.

[54] Per-Erik Danielsson, Qingfen Lin, and Qin-Zhong Ye. Efficient detection of second-degree variations in 2d and 3d images. *Journal of Visual Communication and Image Representation*, 12(3):255 – 305, 2001.

[55] James R. Munkres. *Topology*. Pearson Education International, second edition, 2000.

Index